REPETITIO EST MATER STUDIORUM

Assessment of the McMaster KN Accelerator for Nuclear Resonance Absorption and Fluorescence Experiments with ^{28}Si Nucleus Induced by $^{27}Al(p,\gamma)^{28}Si$ Capture Reaction

By

Jovica Atanackovic, BSc. & MSc.

A Thesis

Submitted to the School of Graduate Studies

in Partial Fulfilment of the Requirements

for the Degree

Doctor of Philosophy in Science

McMaster University

DOCTOR OF PHILOSOPHY IN SCIENCE (2010) McMaster University

(Medical Physics and Applied Radiation Sciences Department) Hamilton, Ontario

TITLE: Assessment of the McMaster KN Accelerator for Nuclear Resonance Absorption and Fluorescence Experiments with ^{28}Si Nucleus Induced by $^{27}Al(p,\gamma)^{28}Si$ Capture Reaction

AUTHOR: Jovica Atanackovic, BSc. & MSc.

SUPERVISOR: David R. Chettle

NUMBER OF PAGES: xvii, 172

Abstract

This thesis represents a detailed assessment of the McMaster KN Accelerator site for the performance of a nuclear resonance absorption and floures-cence phenomenon in the ^{28}Si nucleus. The main focus of this work is the $^{27}Al(p,\gamma)^{28}Si$ reaction, although other nuclear reactions are explored, such as: $^{27}Al(p,p'\gamma)^{27}Al$ and $^{27}Al(p,\alpha\gamma)^{24}Mg$. The gamma yield experiments from all these reactions suggest a repeatable and steady results, as well as very good agreement with the present literature. This is seen in chapter 2. Chapter 3 represents concrete nuclear resonance experiments with a direct ground state transition of the $12.33MeV$ gamma energy from the $^{27}Al(p,\gamma)^{28}Si$ reaction. These experiments are reproducible and repeatable with either HPGe or NaI(Tl) (NaI elsewhere in text) detectors. Also, they are in close agreement with the literature.

However, the main part of this work is described in chapter 4, where the first excited level of Si at $1.78MeV$ is studied thoroughly. This is a pilot work that has never been attempted before. A thorough empirical approach is undertaken and described in section 4.1. This approach describes rationale for attempting nuclear resonance experiments with the first excited state of Si. The calculations suggest very close agreement between $12.33MeV$ and $1.78MeV$ experiments. Based on that, 7 different experimental sets, with several subsets (within some of the sets) are performed. Very interesting results are obtained. However, so far, it cannot be concluded whether NRA/NRF experiments can be performed using the first excited state of Si. Most likely, hight current proton accelerators should be used and the experiments with

$1.78MeV$ lines should be repeated. These accelerators are described in chapter 5 and have the proton current output close to 1000 times higher than the McMaster KN accelerator. At the end, the dosimetry measurements suggest a negligible radiation dose from KN accelerator, as well as from these powerful accelerators.

Acknowledgements

I would like to thank my daughters Ana and Isidora and my wife Jelena for giving me strength, energy and constant encouragement to finalize this work. Huge thanks to my parents Svetlana and Zoran, brother Vladan and sister Vasilisa for giving me tremendous support in the last five years.

I would like to thank MAL staff. In particular, Jason Falladown for running KN accelerator and constantly burning *Al* targets for me during the course of more than 3 years. A huge thanks to Dr. Fiona McNeill, a member of my supervisory committee for giving me an opportunity (long ago) to be the part of Medical Physics family at McMaster University. Furthermore, I would like to thank other members of my supervisory committee: Dr. Bill Prestwich, Dr. Balraj Singh and Dr. Soo-Hyun Byun. Bill, for teaching me the first principles and fundamentals of radiation physics as well as for advising me during the course of this work, Balraj for helping me with nuclear physics and Byun for enormous help in experimental part of this work.

I have saved my greatest appreciation, for the end, because it is very hard to be as short as possible and to summarize more than seven incredible years of one's life. The person who gave me not only scientific, but life tools as well, is my supervisor Dr. David Chettle. With all his incredible patience, David allowed me to discover myself through constant falls and rises, numerous mistakes and all the bitterness that this project carried for over 5 years. He was there for me from the beginning of this journey to the very end; from $3T3$ to the end of this thesis. He did not teach me physics, he taught me how to learn constantly, explore and love physics. David, thank you for everything!

To my grandmother Milena and grandfather Stojan who are in Heavens

Table of Contents

List of Figures

List of Tables

Chapter 1

Introduction and Theory

1.1 Opening Remarks

In the Medical Physics and Applied Radiation Sciences Department, at McMaster University, the detection of trace elements (both toxic and non-toxic), using nuclear and atomic techniques is one of the most important and strongest research fields. The experiments are performed both *in vitro* and *in vivo*, depending on how well a particular experimental technique is established in terms of minimum detection limits (MDL), and overall performance. Also *in vivo* practice depends mostly on the radiation dose received by the patient. The received gamma and/or neutron radiation doses must be below reasonable limits in order for an *in vivo* measurement to be considered. These measurements take place simultaneously at several experimental sites: KN accelerator, Tandem accelerator, McMaster Nuclear Reactor (MNR), $^{238}Pu/Be$ portable neutron source. Also, numerous operator independent low energy $\gamma - Ray$ and $X - Ray$ sources are available for XRF (X-Ray Fluorescence) measurements and experiments. There are established XRF techniques for measuring lead

[16] strontium [17], cadmium [18], and arsenic [19]. Most of them are taking place *in vitro* and some of them *in vivo*, since the radiation doses are significantly low. Also, numerous elements are measured using nuclear techniques such as prompt gamma and delayed gamma neutron activation analysis (PGNAA and DGNAA, respectively) [20]. Those are cadmium [21], mercury [18], aluminum [22] [23] [24], manganese [25] [26] [27], magnesium [28]. The low neutron and gamma doses for these experimental sites are well characterized by several studies [29] [30] [25] [18]. Furthermore, in 1999 there was a joint study with an Israeli group focused on measurement of whole body nitrogen *in vitro* (pilot study) using nuclear resonance gamma ray absorption (NRA) [31]. The technique was based on proton bombardment of thin ^{13}C target and creation of specific nuclear gamma rays ($9.17MeV$ resonance) that were further used for NRA. The experiments took place at the McMaster KN accelerator. The reaction used in the process was: $^{13}C(p,\gamma)^{14}N$. Given that this technique represents the primary focus of this research, thorough explanations and theoretical approaches will be outlined later in the chapter. In any case, that was the first attempt to use NRA technique for *in vitro* measurements at McMaster University.

The purpose of this work is to establish an appropriate experimental model based on the NRA technique in order to standardize it for concentration measurements of silicon metal *in vitro* and possibly *in vivo*. This novel and extremely difficult nuclear measurement technique is based on the $^{27}Al(p,\gamma)^{28}Si$ reaction. Following possible positive results from the study, the ultimate goal would be to use this technique in order to detect different concentrations of trace amounts of Si metal in different samples. More specifically, the objec-

tive was to establish the standards of minimum detection limits (MDL) for silicon, using this technique and present equipment (KN accelerator). However, we will see that this particular study is concerned only with developing the measurement technique at the KN accelerator site. Chapter 1 will deal with all theoretical and practical concerns regarding NRA. Furthermore, it will explore all relevant literature and approaches that are significant for better understanding the process of this interesting event. Before we delve into the theory, in the following section we will briefly discuss the importance of Si metal in human body. Also we will touch upon its basic nuclear and atomic properties and, subsequently the reasons why are we trying to develop and use the technique of NRA for Si measurements.

1.2 Natural Silicon; Si

1.2.1 Significance and Organic Importance

Natural Si consists of three stable isotopes: ^{28}Si (abundance 92.23%), ^{29}Si (4.67%) and ^{30}Si (3.10%) [32]. After oxygen, silicon is the most abundant element in the crust of the Earth [33][34]. It is very rarely found in its elemental form. Since it has a great affinity towards oxygen, it is found in the solid form of silica and silicates [1]. The most common examples of silicates are: quartz (SiO_2) and aluminosilicates (in the form of Al_2SiO_5) [1]. The dissolved silicates in water form soluble silica (low silicon concentration) species, among which the most common is monosilicic acid, also known as orthosilicic acid, or $Si(OH)_4$ [1]. This is the only form of silicon that can be absorbed by humans

and other living organisms. However, monosilicic acid is stable in very low concentrations, below $2mM$. Otherwise, it will take the form of a polymeric molecule, which significantly reduces its solubility and hence availability for living organisms [1]. Partly, the silicon is taken through drinking water ($20-30\%$) [35]. On average there is approximately $6.2mg/L$ of Si in drinking water [1]. This number may vary significantly, depending on many factors, such as: water type, geographical location, water source, weathering. For example, in Britain, depending of softness of the water, the silicon concentration may vary from $0.2-2.5mg/L$ for soft water and $2.8-14mg/L$ for harder water [36][37][38]. Hence, in general, higher concentrations of dissolved silicon are found in the lowlands of England, compared to Scotland's highlands. The main reason for this is the fact that younger rocks in lowlands of England are easier to weather and therefore the water is harder.

The other major source of Si intake is solid food. India and China have the highest intake of Si through this pathway; $143-204mg/day$ and $139mg/day$, respectively [39][40][41]. Contrarily, Si intake in Western world is significantly lower; $13-62mg/d$ [1]. In general, plant-based food is the major contributor to the Si intake. In particular, grains and cereals with $(49\pm34)\%$ and fruits and vegetables with $(21\pm29)\%$ [1]. Interestingly, studies by Jugdaohsingh et al. [39] and Pennington [41] argued that major source of silicon in adult males is **beer**. Depending on consumption, it can go up to 44%, while for children, this is cereal with 68% of total Si intake. Moreover, they suggested that concentration of Si in beer is $(19.2\pm6.6)mg/L$, while in cereals this can vary; $(7.79\pm6.31)mg/100g$.

Lastly, Si can be taken artificially through dietary supplements, pharmaceuticals and cosmetics [1]. The following three tables summarize the above. Table 1.1 is taken from Jugdaohsingh et al. [1]. The other two tables; 1.2 and 1.3 are also taken from the same article, however, they represent some important findings of a study done in United Kingdom in 2005 by Powell et al. [2].

Human exposure to silicon

Sources	Exposure Levels	Comments
Soil	28% of the Earth's crust	Locked up in minerals (e.g., quartz, aluminosilicates). Inert, insoluble and very little is bioavailable (even to plants). Only released with weathering.
Dust	No data avilable.	Wide variety and forms (crystalline and amorphous). Inhaled; not readily solubilised; retained in the lungs and does not participate in the general metabolism of Si in the body.
Water	0.8-35 (median: 6.2) mg/L (freshwater), 0.001-0.3 mg/L (marine) 0.2-14 mg/L (tap), 4-40 mg/L (mineral/spring)	Most readily bio-available source (50-80%), as Si present as soluble OSA. Intake can make up 20-30% of daily Si intake, may be higher from mineral waters.
Diet	13-62 mg/d (Western countries) 143-204 mg/d (India), 139 mg/d (China)	Major contribution from plant-based foods (cereals, grains and some fruits & vegetables) and little from dairy and meat. Mean bioavailability is ~41%. Cereals, grains & products: 49±34%; Fruits & vegetables: 21±29% (bananas: 2.1%)
Dietary additives	≤ 2% food weight (UK)	Silicates (Mg, Ca & Al). Extracted from natural minerals or synthetics. Supposed to be inert and not absorbed from GI tract
Dietary supplements	Variable: 0.02 to 60 mg/g. Horsetail 9-17 mg/g	Colloidal. gels, plant-based, etc. Bioavailability is low, << 20% for most; BioSil (stabilised-OSA; BioMinerals NV, Belgium), ~30%; Monomethyltrisilano (LLR-G5, Ireland) is similar to OAS, at least 50% bioavailable.
Pharmaceuticals	Main components of antacids ($Mg_2Si_3O_3$; 250 mg/g), anti-diarrhoeal (Al & Mg silicates; 80% wt), and as excipients in proprietary analgesics	Can greatly increase exposure (>1g/d) but are supposed to to be inert & not absorbed. 5-10% at most is absorbed. Long term use can lead to silica stones and kidney damage
Cosmetics/ Toiletries	No data available. Excipients and viscosity agents.	Toothpaste, creams (silicones), lipstick, coloured/powdered cosmetics & talcum powder (Mg hydrogen silicate). Dermal absorption suggested to be low as silicates are not lipid soluble, but silicones in hand and nail creams are. Dermal absorption of aluminosilicates is linked to podoconiosis an inflammatory disease.
Other sources (e.g. detergents, tissue implants, etc.)	No data available	Exposure is low/minor for most individuals.

OSA= orthosilicic acid; GI= gastrointestinal

Figure 1.1: Human Exposure to Silicon [1]

Food sources of silicon

Food Groups	Si (mg/100g)	Range	Comments
Cereals Grains & Products			
Breakfast Cereal (n=16)	7.79 ± 6.31	1.34–23.36	11 of the 18 foods with high Si content (> 5mg/100g) are from this group. Silicon is almost solely present in the outer skin (husks/hull) of the grain. Oat bran has the highest Si content as it consists of the husk/hull
Bread/Flour (n=15)	2.87 ± 1.60	0.34–6.17	
Biscuit (n=5)	1.56 ± 0.56	1.05–2.44	
Rice (n=8)	1.54 ± 1.00	0.88–3.76	
Pasta (n=7)	1.11 ± 0.47	0.62–1.84	
Fruits			
Raw& canned (n=33)	1.34 ± 1.30	0.1–4.77	Bananas, pineapples and mangoes are high.
Dried (n=3)	10.54 ± 5.44	6.09–16.61	
Vegetables (n=49)	1.79 ± 2.42	0.1–8.73	High in Kenyan beans, green beans, runner beans, spinach and coriander.
Legumes (lentils, pulses, etc.; n=11)	1.46 ± 1.23	0.38–4.42	Lentils and Soya/tofu are high.
Nuts & Seeds (n=4)	0.78 ± 0.82	0.28–1.99	
Snack Foods (crisps, candy, etc; n=3)	1.97 ± 2.15	0.47–1.01	
Milk & Milk Products (TDS & n=3)	0.31 ± 0.21	0.07–0.47	Low Si content
Meat & Meat Products (TDS)		0.1–1.89	Low Si content

Table adapted from Powell et al. (44); TDS= Sample four the Food Standard Agency total diet study

Figure 1.2: Silicon in Food [1] [2]

Silicon in beverages

Food Groups	Si (mg/100g)	Range	Comments
Beverages (non-alcoholic)			
Tap water (n=11)	0.37 ± 0.13	0.095–0.61	Mineral waters > tap water
Mineral & Spring waters (n=14)	0.55 ± 0.33	0.24–1.46	Tap waters > carbonated drinks
Tea & Coffee (n=6)	0.51 ± 0.28	0.24–0.86	
Fruit juices (n=11)	0.38 ± 0.53	0.05–1.5	
Fizzy/Carbonated (n=6)	0.15 ± 0.04	0.11–0.19	
Milk based (n=6)	1.30 ± 1.40	0.2–3.96	
Beverages (alcoholic)			
Beers (n=76)	1.92 ± 0.66	0.9–3.94	No correlation with alcohol content, type of beer, type of storage/packaging or geographic origin
Wines (n=3)	1.35 ± 0.85	0.68–2.31	
Port/Sherries (n=2)	1.24-1.26		
Liquor/Spirits (n=11)	0.13 ± 0.04	0.06–0.20	

Figure 1.3: Silicon in Beverages [1] [2]

Considering what was said above and observing the summary tables, the main route of silicon absorption is through the GI tract. It was also found by Jugdaohsingh [39] that urinary excretion of Si is in direct correlation with the dietary intake. Dobbie et al. [42] found that silicon concentrations in the blood are similar to the concentrations of zinc, copper and iron. Moreover, the silicon and calcium excretion rates are very similar. The silicon is present in all tissues. However, the concentration may vary. Exley [33] did a study on rats and suggested that silicon concentration is highest in bone and connective tissues (tendons) hair, skin and nails. This study also found that a very high concentration of Si is in inner lining of aorta, called tunica intima. Furthermore, it is expected that a similar tissue distribution is present in humans, but there are no studies so far to confirm this. There are some studies done on infant chicks and rats [43] [44] suggesting the importance of silicon in normal bone and connective tissue growth and development. There are a number of studies done on human and animal cultured bone tissues suggesting a very important role of Si in the development and growth of normal bone and bone mineral density (BMD). For example, it was shown by Jugdaohsingh et al. [45] and MacDonald et al. [46] that BMD of the hip and spine is in correlation with dietary intake of silicon. The hip case was seen in men and pre-menopausal women. Also, the spine case was seen in pre-menopausal women and post-menopausal women under hormone replacement therapy.

The very first silicon deprivation studies on animals were were done in the seventies. These include studies with rats [43] and chicks [44]. It the case of chicks, it was found that beaks and bones were more fragile, paler and thinner, while in the case of rats, visible skull and teeth defects were observed.

Moreover, similar Si deprivation studies in rats were performed in the nineties and at the beginning of this century by Seaborn and Nielsen [47] [48] [49] [50]. These studies further showed lower BMD, decrease of bone mineral content of femur, tibia and vertebrae [49][50], decrease in body weight [47], decrease in collagen synthesis and increase in collagen breakdown [48]. Opposite studies, where Si supplementation was introduced were conducted by Elsinger and Clairet [51] in 1993. The silicon was introduced in the form of monomethyl trisilanol. The introduction of Si showed increase in femoral and lumbar spine BMD in osteoporotic patients. The drug was introduced orally in the amounts of $100mg/week$ for 4 months. A study done in 2005 by Spector et al. [52] used choline-stabilized orthosilicic acid (ch-OSA) as a Si supplement. The subjects were females with low BMD. The amount of Si supplement ranged from 0 to $12mg/day$. The study showed increased BMD with daily dose of $6mg$. All these facts clearly suggest an important biological role of Si.

So far we have seen beneficial sides of Si. However, over exposures to Si can be toxic as well [1]. Inhalation of different forms of Si is the most common mechanism of silicon long term chronic poisoning. Asbestos is a well known material that contains Si and is very toxic if inhaled chronically. It can cause lung cancer, tuberculosis and heart problems [1]. This is correlated more to the fibre structure of asbestos, then Si itself, however, the amount of asbestos in the lungs is linearly proportional to the amount of Si. Moreover, over exposure to different forms of Si can cause kidney problems, such as kidney inflammation (interstitial nephritis). This is chronic damage of renal kidney tubules. There are data that showed increased rates of interstitial nephritis in peoples of the Balkans (former Yugoslavia, Romania and Bulgaria) [1]. This

was due to the increased concentration of silicate minerals in drinking water in some confined parts of these countries. No studies so far were conducted that showed normal exposures to Si in correlation with silicon health related problems.

1.2.2 Nuclear and Atomic Properties; The Reasons for NRA Technique

In the previous section we have seen organic importance of Si metal in living organisms. Clearly it is an essential trace element. Contrarily, we have seen that it can be even toxic if high concentrations are found in the living organisms. Because of that the idea was to try to quantify the amount of Si *in vivo*. In particular, quantification would involve measurement of Si, using noninvasive nuclear and/or atomic techniques. Unfortunately, some of the existent and previously discussed experimental techniques are not appropriate because of the physical properties of Si. Since, Si is light element, the case of XRF is restricted due to very low energies of K_α and K_β X-rays; $1.74keV$ and $1.83keV$, respectively [53]. For comparison, the most prominent K_α and K_β X-rays of lead are $75keV$ and $85keV$, respectively [53]. As indicated above, Pb is the trace element where XRF technique was proven to work *in vivo* [16]. However, from the numbers quoted, we see that Pb X-Rays are more than 40 times higher in energy compared to Si X-Rays. At these very low energies X-Rays, such as in Si case, there are numerous difficulties for XRF experimental technique to take place. The largest obstacle is huge attenuation coefficients. Also there are difficulties associated with successful detection and

spectroscopy of very low energy electromagnetic radiation. The final problem would be finding an appropriate source to induce the XRF phenomenon in Si. When considering nuclear techniques, such as thermal neutron activation, (prompt gamma or delayed gamma), the main obstacle is very low cross section for thermal neutrons of only $177mb$ [54]. Furthermore, there would be a huge competition for thermal neutrons with other abundant, as well as trace elements in living tissues. In general those elements are: C, N, K, Cl, H, O, Al. When compared to Si, most of these elements have much larger cross sections and they are much more abundant in the living tissues. Taking all of the above into consideration, it is evident that these techniques are not the best choices for quantifications of Si *in vivo*. However, Ettinger et al. [55] did experiments where they used neutron inelastic scattering to measure high concentrations of Si in anthropomorphic chest phantoms. For these experiments, the $^{28}Si(n, n'\gamma)^{29}Si$ nuclear reaction was used and neutron energies ranging from $5MeV$ to $8MeV$. After extensive experimenting with Van de Graaff accelerator, different targets and projectiles, Ettinger et al. managed to optimize experimental settings. The final experiment comprised of deuterium target, bombarded with $4MeV$ deuterons. The reaction produced was: $D(d, n)^3He$. The nominal neutron energy was $7MeV$. With this neutron source, they managed to establish MDL of $0.6g$ of Si in lung phantoms. At the same time, the equivalent dose was $10mSv$. Considering all this, our primary goal was to use some similar, radiation based, non-invasive technique in order to measure Si. The choice was nuclear resonance absorption of gamma rays (NRA). However, it will become clear later in the thesis that even establishment of the technique itself would be a very difficult task. The following discussion will introduce

briefly a logic of the NRA. After that, in the section to come, we will delve deeper into the theory of NRF/NRA, referring to the appropriate literature. As mentioned before, a pure thick or thin Al target was bombarded with a beam of protons. The proton currents and energies varied depending on the nature of an experiment. The prompt process of releasing nuclear gamma rays is pictured in the nuclear reaction below:

$$^{27}Al + p \rightarrow ^{28} Si + \gamma \tag{1.1}$$

The reaction is highly exothermic with a Q value of $11.584MeV$ [56]. Therefore, by capturing an incoming proton the ^{28}Si nucleus would be excited up to a high energy resonance level, usually above $12MeV$, since [56]:

$$E_{level} = E_{cm} + Q \tag{1.2}$$

Where E_{cm} is the center of mass energy of incoming proton. These resonance levels (states) would de-excite to the Si ground state by releasing excess energy in the form of gamma rays, either directly or in cascade. There are more than 85 known resonance states [57]. The strongest resonance, or the resonance with the highest gamma ray yield is populated by $992keV$ protons [58]. This resonance sits $12.54MeV$ above the ground state of Si and it decays to the first excited state of Si $(1.78MeV)$ with absolute branching ratio of 75% [57]. The rest of 25% of decays de-excite to the ground state through different cascades. For illustrative purposes, the decay scheme of $992keV$ resonance is given in figure 1.4 [58].

At the same time, the strongest resonance that decays to the ground state directly with the greatest absolute branching ratio (75%) is populated by

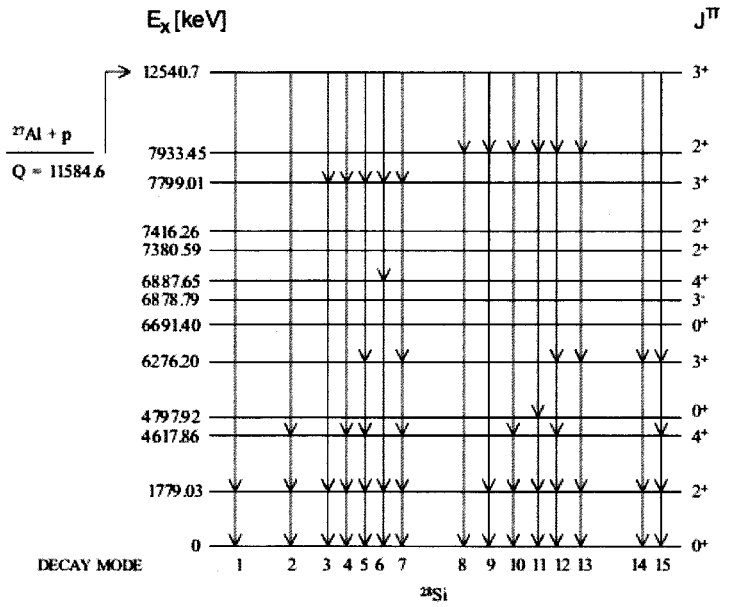

Figure 1.4: Decay scheme of $12.54MeV$ resonance, populated by $992keV$ protons

$771keV$ protons. This excited state of silicon is $12.33MeV$ above the ground state [10]. The mean life-time of this resonant state is about $45as$ [10]. The natural width of the resonant state, or any other excited bound state is described by the uncertainty principle:

$$\Gamma = \frac{\hbar}{\tau} \tag{1.3}$$

However, we will see later in the chapter, that in practice, the value of the width of the resonance state is much larger than proposed natural width, due to the thermal motion of nuclei. The thermal motion is described by a Maxwellian distribution function and the corresponding width is called the Doppler broadened width. All the relevant in-depth theory is described in the following section.

1.3 Nuclear Resonance Gamma Ray Absorption and Fluorescence (Emission)

As the title suggests the processes of nuclear resonance gamma ray fluorescence (NRF) and nuclear resonance gamma ray absorption (NRA) are inverse. In particular, these processes are subsequent; i.e. they follow each other sequentially. A nucleus can absorb a particular gamma ray and jump to its excited state above the ground state, but promptly after, the excited nucleus will return back to its ground state, by emitting the same gamma ray, as the excess of nuclear energy. The gamma ray can be directly emitted to the ground state or it can be emitted in cascade through several other excited energy states, shown in figure 1.4. Evidently the processes of nuclear resonance absorption and emission of gamma rays happen sequentially, one after the other. This is somewhat similar to the atomic x-ray absorption and fluorescence (XRF), except that in nuclear case much higher gamma ray energies are involved; i.e. 1 to 2 orders of magnitude, compared to atomic x-ray transitions. For illustrative purposes, the XRF features are observed below $100keV$, while NRF and NRA features are observed above $1MeV$ and very often above $10MeV$. Considering this, obviously, NRA and NRF are processes where the energy of the recoiling nucleus, or nuclear recoil, cannot be ignored. This fact will become more evident later in the chapter, since the proof will come directly from the calculations that follow. Particularly, this is the main problem and concern when NRA and subsequently NRF are used in experiments. Hence, it is the greatest obstacle of this project. There are several experimental approaches used in order to overcome the problem of the recoiling nucleus. All of them will be discussed later in this section. However, in order to start from the

beginning, we are going to take a look at the classical treatment of an excited nucleus of mass M, with initial energy E_i that decays to the ground state with final energy E_f, releasing a gamma ray of energy $E\gamma$ [3]:

$$E_i \rightarrow E_f \tag{1.4}$$

Furthermore, E_i can be written as:

$$E_i = E_f + E_\gamma + T_r \tag{1.5}$$

Where, T_r is the kinetic energy of recoiled nucleus. Before gamma decay, the particular nucleus was assumed to be motionless and total linear momentum of the system was zero. Furthermore, according to the conservation of linear momentum; after the decay the sum of the linear momenta of recoil nucleus (P_r) and gamma ray (P_γ) must be zero as well:

$$0 = P_r + P_\gamma \tag{1.6}$$

Writing the kinetic energy of a recoiled nucleus:

$$T_r = \frac{P_r^2}{2M} \tag{1.7}$$

and rearranging equation 1.5, we have:

$$\Delta E = E_i - E_f = E_\gamma + \frac{P_r^2}{2M} \tag{1.8}$$

Where, ΔE is the energy difference between excited and ground state. Also, substituting equation 1.6 into equation 1.8 and using the fact that:

$$P_\gamma = \frac{E_\gamma}{c} \tag{1.9}$$

we can easily come to the quadratic equation that is solvable for E_γ:

$$\frac{1}{2Mc^2}E_\gamma^2 + E_\gamma - \Delta E = 0 \tag{1.10}$$

Now solving the above quadratic equation for E_γ, we end up with the solution in the form:

$$E_\gamma = Mc^2(-1 \pm \sqrt{1 + \frac{2\Delta E}{Mc^2}}) \tag{1.11}$$

Further expanding the square root term we finally end up with solution for gamma ray energy:

$$E_\gamma \cong \Delta E - \frac{(\Delta E)^2}{2Mc^2} \tag{1.12}$$

Moreover, $\Delta E \approx E_\gamma$, so finally we can write:

$$E_\gamma = \Delta E - \frac{E_\gamma^2}{2Mc^2} \tag{1.13}$$

The second term in the above equation represents the kinetic energy of the recoiled nucleus. Similarly, if we use the same treatment to calculate gamma ray energy needed for inverse process (NRA) to take place, we would come up with relationship for the energy of gamma ray that is required for this to take place:

$$E'_\gamma = \Delta E + \frac{E_\gamma^2}{2Mc^2} \tag{1.14}$$

Obviously, we can see from equations 1.13 and 1.14 that gamma rays required for absorption and gamma rays emitted during the fluorescence differ by 2 times the recoil energy or:

$$\frac{E_\gamma^2}{Mc^2} \tag{1.15}$$

For illustrative purposes, the resonance that is $12.33MeV$ above the silicon ground state (populated by $771keV$ protons) de-excites with branching ratio of 75% directly to the ground state [57]. According to the recoil equation:

$$E_r = \frac{E_\gamma^2}{2Mc^2} \tag{1.16}$$

The initial kinetic energy of the recoiled silicon nucleus would be:

$$E_r = \frac{(12.331MeV)^2}{2 \times 27.9769amu \times 931.502MeV/amu/c^2 \times c^2} = 2.92keV \tag{1.17}$$

Hence, resonantly released and absorbed $12.33MeV$ gamma rays differ by $2 \times 2.92keV = 5.84keV$. Similarly, we can take a look at another transition; $1.78MeV$, the first excited state of silicon. In this case we have $E_r = 60.79eV$, so that the difference between absorption and fluorescence lines is $121.58eV$. The number in either case is relatively large. Because of this huge energy difference in absorption and fluorescence lines, we will observe no overlap between them and absolutely no chance of the sequence NRF / NRA to occur. This will become more apparent later in the chapter, when we introduce the concept of resonance absorption cross section with natural and Doppler broadened width. Moreover, from the literature [10], the natural width of the $12.331MeV$ line was found to be $(9.0 \pm 0.6)eV$, while the natural width of the $1.78MeV$ state is $0.96meV$ [32]. If we are observing an isolated nuclear level, that de-excites only by one possible mode of gamma decay (for instance: directly to the ground state, with no cascade present) the cross section for subsequent NRA of the same gamma ray is given by the Breit-Weigner formula, introduced by Bethe [59]:

$$\sigma(E) = \frac{\lambda^2}{8\pi} \frac{2J_1 + 1}{2J_0 + 1} \frac{\Gamma^2}{(E - E_r)^2 + \frac{1}{4}\Gamma^2} \tag{1.18}$$

In the equation above J_1 and J_0 are the total angular momenta of the excited and ground states respectively, λ is the wavelength of gamma radiation and Γ is natural width of the line. In the following calculation, we are going to use examples of $12.33MeV$ resonance and $1.78MeV$ first excited Si state. For the first case we have:

- $J_1 = 1^+$ and $J_0 = 0^+$ [10]
- $\Gamma = (9.0 \pm 0.8)eV$ [10]
- $\lambda^2 = (\frac{hc}{E})^2$

Similarly, for the second case we have:

- $J_1 = 2^+$ and $J_0 = 0^+$ [32]
- $\Gamma = 0.96meV$ [32]

Substituting all of the above into equation 1.18, for the $12.33MeV$ case, we end up with cross section:

$$\sigma_{12.33}(E) = 12.076b \times \frac{81eV^2}{(E - 12.331MeV)^2 + 20.25eV^2} \tag{1.19}$$

Using the same approach, for the $1.78MeV$ exited state, we will observe:

$$\sigma_{1.78}(E) = 966.28b \times \frac{0.922meV^2}{(E - 1779.03keV)^2 + 0.230meV^2} \tag{1.20}$$

In general, we will observe fluorescence and absorption lines separated by two times recoil energy. Hence, in case of $12.33MeV$ resonance, the energy

required by the absorber will be shifted up by the recoil value ($2.94keV$) and cross section will read:

$$\sigma(E) = 12.076b \times \frac{81eV^2}{(E - 12333.92keV)^2 + 20.25eV^2} \tag{1.21}$$

Similarly, the energy emitted by the source will be shifted down for the recoil value and cross section will read:

$$\sigma(E) = 12.076b \times \frac{81eV^2}{(E - 12328.08keV)^2 + 20.25eV^2} \tag{1.22}$$

For illustrative purposes gamma ray of $12.33MeV$ case is pictured in figure 1.5.

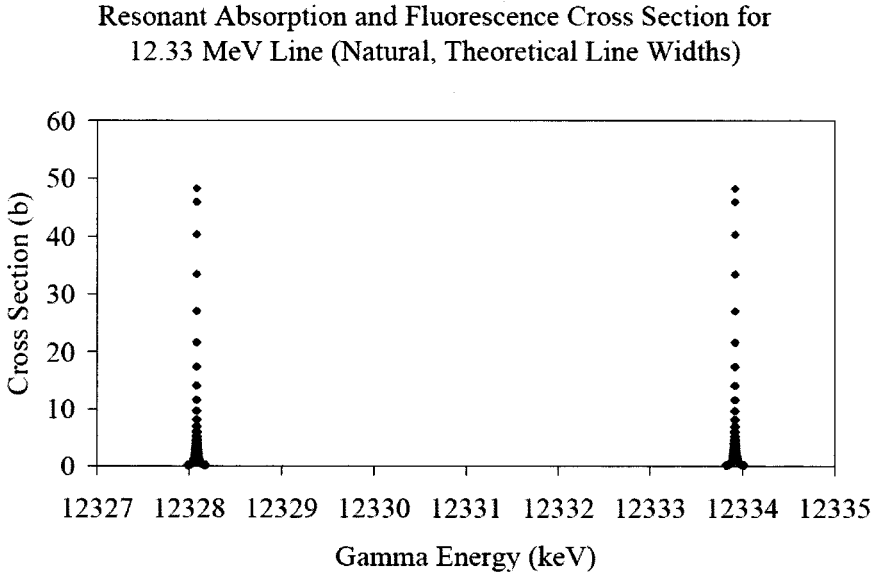

Figure 1.5: Resonance fluorescence and absorption lines for $12.33MeV$ gamma ray

From figure 1.5, it is evident that the theoretical width of $12.331MeV$ gamma ray is negligible compared to the recoil energy and hence there is practically no probability for the NRA / NRF sequence to occur, since there is absolutely no overlap between two resonance lines. However, these theoretical widths are broadened, by nuclear motion due to thermal energy. The

following section will treat a realistic model of the NRA / NRF sequence and all conditions and approximations associated with that. Furthermore, this will emphasize the difficulty in obtaining realistic absorption cross sections for NRA. The nuclear velocities within the absorber are distributed according to the Maxwellian distribution function [60]:

$$w(v)dv = \sqrt{\frac{M}{2\pi k T_{eff}}} e^{-\frac{Mv^2}{2kT_{eff}}} dv \tag{1.23}$$

Note that T_{eff} is effective temperature of the absorber, which is not the actual room temperature. It is rather calculated from a specific Debye temperature, θ_D, for particular crystal [60]. The Debye temperature is given by the relationship [61]:

$$\theta_D = \frac{h}{k}(\frac{3N}{4\pi V})^{1/3} v_s \tag{1.24}$$

Also, the effective temperature is given by the following relationship [62]:

$$\frac{T_{eff}}{T} = 3(\frac{T}{\theta_D})^3 \int_0^{\theta_D/T} t^3(\frac{1}{e^t - 1} + \frac{1}{2})dt \tag{1.25}$$

Finally, let's assume $f(t)$ to be integrand function from the above equation:

$$f(t) = t^3(\frac{1}{e^t - 1} + \frac{1}{2}) \tag{1.26}$$

In above equations, N/V and v_s represent number density and speed of sound in crystal, respectively, while h and k are Planck's and Boltzmann's constants, respectively. In our experiments to follow, we are going to use ordinary glass (soda lime glass) for windows, as Si absorber. According to Seward [63], soda lime glass is composed of: SiO_2 (73%), Na_20 (14%), CaO (9%) and MgO (4%). The speed of sound in this material was calculated to be $5408.2 m/s$ with density of $2.53 g/cm^3$ [63], both at room temperature

($T = 20°C = 293.15K$). Using the proportion of the mixture, outlined above, and its density, it was calculated that number density (N/V) for soda lime glass is $7.382 \times 10^{22} atoms/cm^3$. Therefore, the Debye temperature, θ_D was found to be $676.6K$. Moreover, using the simple trapezoid rule for performing numerical integration of equation 1.26 from 0 to θ_D/T, T_{eff} was finally found to be $367.8K$. For the nucleus moving towards the radiation source, the emitting gamma ray energy has shifted frequency, and hence the energy, due to Doppler effect. The shifted energy E' can be written as:

$$E' = \frac{E(1+\frac{v}{c})}{\sqrt{1-(\frac{v}{c})^2}} \approx E(1+\frac{v}{c}) \tag{1.27}$$

Where v is the velocity of moving nucleus. It is important to keep in mind here that movement of a nucleus is only due to the thermal energy and in accordance to the Maxwellian distribution function, defined by the equation 1.23. Using this equation and equation 1.27, we can easily rewrite $w(v)$ in terms of E':

$$w(E')dE' = \frac{1}{\Delta\sqrt{\pi}} e^{-(\frac{E'-E}{\Delta})^2} dE' \tag{1.28}$$

In this equation, Δ represents Doppler width due to nuclear motion and it is given by [64]:

$$\Delta = E\sqrt{\frac{2kT_{eff}}{Mc^2}} \tag{1.29}$$

Averaging the NRA cross section over all possible energies, we end up with expression [60]:

$$\sigma(E,t) = \int \sigma(E')w(E')dE' = \sigma^0_{max}\psi(x,t) \tag{1.30}$$

Where:

$$x = \frac{2(E-E_r)}{\Gamma} \tag{1.31}$$

And:

$$t = (\frac{\Delta}{\Gamma})^2 \tag{1.32}$$

In equation 1.30, σ^0_{max} represents maximum cross section, when $E = E_r$. See equation 1.18. Hence, the maximum cross section will read:

$$\sigma^0_{max} = 4\frac{\lambda^2}{8\pi}\frac{2J_1+1}{2J_0+1} \tag{1.33}$$

Finally, we have:

$$\psi(x,t) = \frac{1}{2\sqrt{\pi t}}\int_{-\infty}^{\infty}\frac{1}{1+y^2}e^{-(\frac{(x-y)^2}{4t})}dy \tag{1.34}$$

Where:

$$y = \frac{2(E'-E_r)}{\Gamma} \tag{1.35}$$

The integral in the equation 1.34 is very hard to solve analytically. The most cited source for tabulated function $\psi(x,t)$ is WAPD by Rose et al. [65]. Unfortunately, it was not possible to get hold of this material. Rose calculated $\psi(x,t)$ for the x values up to 300 and t values up to 2500. Furthermore, Beynon in his article [66] was able to solve the integral analytically, using the Tchebysheff polynomial expansion. Only a small fraction of his calculations can be found in the article and it is also available in the Duderstadt textbook [67]. Also, Melkonian [68] and Dardel [69] used these integrals in their articles as the means for neutron resonance calculations. Metzger [60] used the fact that for large values of x and t (larger than those tabulated by Rose in his article [65]), $\psi(x,t)$ can be approximated by following expression:

$$\psi(x,t) = \frac{1}{2}\sqrt{\frac{\pi}{t}}e^{-x^2/4t} \tag{1.36}$$

Finally, for $\Delta \gg \Gamma$, effective cross section becomes:

$$\sigma_D = \sigma^0_{max}\frac{\Gamma\sqrt{\pi}}{2\Delta}e^{-(\frac{E-E_r}{\Delta})^2} \tag{1.37}$$

Table 1.1: Nuclear Properties of $12.33MeV$ and $1.78MeV$ Gamma Transitions

Nuclear Properties	$E_\gamma = 12.33MeV$	$E_\gamma = 1.78MeV$
Transition half-life ($t_{1/2}$)	$(0.045 \pm 0.004)fs$ [10]	$475fs$ [32]
Transition mean life-time (τ)	$0.0649fs$	$685fs$
Resonance Natural Width (Γ)	$(9.0 \pm 0.8)eV$ [10]	$0.96meV$
Doppler Broadened Width (Δ)	$19.23eV$	$2.7746eV$
t value ($t = (\frac{\Delta}{\Gamma})^2$)	4.57	4.02×10^6
Max Cross Section $E = E_r$ (σ^0_{max})	$48.27b$	$3865.13b$

Table 1.1 summarizes important nuclear properties of the two transitions of interest. Evidently, the effective cross section for $1.78MeV$ transition can be approximated using the equation 1.37, since t value in this case was calculated to be very high (4.02×10^6). However, in the case of the $12.33MeV$ transition, the effective cross section must be calculated either from the Tchebysheff polynomial expansion, or using the integral table given by Rose et al. [65]. In this thesis we will not go into the details of obtaining the effective cross section for the $12.33MeV$ transition, since Doppler angle correction for nuclear resonance absorption was proven to work in this case [10]. However, in the case of $1.78MeV$ transitions, we will demonstrate that Doppler broadening due to the nuclear thermal motion (or effective cross section) does not help in resolving the nuclear resonance fluorescence and subsequent absorption issues. Therefore, substituting all relevant factors into equation 1.37, we can easily obtain the effective cross section for the $1.78MeV$ transition. Hence it is given by a Gaussian relationship:

$$\sigma_D = 1.185e^{-(\frac{E-1779030eV}{2.7746eV})^2} \tag{1.38}$$

The obtained cross section is given in the units of barns, while independent energy variable must be in the units of eV. Furthermore, using the fact that

nuclear recoil in the case of $1.78MeV$ gamma ray was calculated to be $60.79eV$, we can distinguish between the fluorescence and absorption cases. This is similar to the $12.33MeV$ gamma ray discussed before in the chapter and depicted in figure 1.5. Finally, the effective cross section shifted up for the energy recoil value would simply read:

$$\sigma_D = 1.185e^{-(\frac{E-1778969.21eV}{2.7746eV})^2} \tag{1.39}$$

At the same time the effective cross section shifted down for the energy recoil value would read:

$$\sigma_D = 1.185e^{-(\frac{E-1779090.79eV}{2.7746eV})^2} \tag{1.40}$$

We can also plot these two cases in order to see the effectiveness of Doppler broadening due to the thermal motion of nuclei. The plot is given below in figure 1.6. From this figure, since there is absolutely no overlap between two Gaussian lines, it is evident that Doppler broadening due to thermal motion of nuclei at room temperature is still not enough to compensate for the huge energy difference between absorption and fluorescence lines, caused by nuclear recoil. The same effect was observed in the case of $12.33MeV$ line.

In general, there are several experiments that can be performed in order to overcome these difficulties and to make the NRF/NRA sequence work. Firstly, we will discuss briefly two of them, when relatively low resonance gamma energies are involved (usually under $500keV$), paired with relatively heavy nuclides (usually $A > 150$) [60]. Furthermore, we will discuss the third experiment involving resonance gamma rays with higher energies and lighter nuclides. Lastly, we will talk about the fourth experiment, based on the nuclear reactions (proton capture, in particular). In fact this experiment is the integral

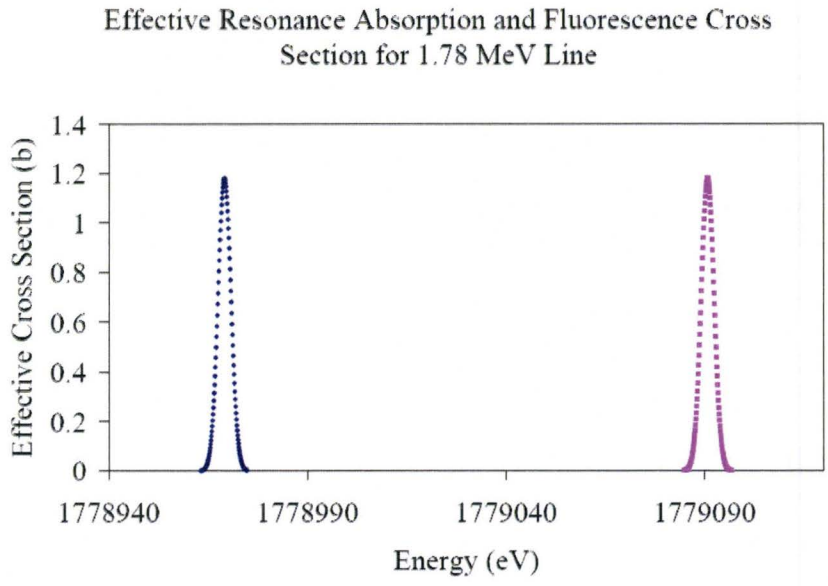

Figure 1.6: Effective resonance absorption and fluorescence cross section for $1.78MeV$ line

part of the thesis and it will be discussed thoroughly in chapters to follow, as well. In order to overcome nuclear recoil, one can either further broaden the effective width of the resonance lines (further Doppler broadening, or simply **Doppler broadening**), or shift mechanically one (or both) of the resonance lines for the value of the recoil (**Doppler shift**). It is important not to confuse further Doppler broadening with Doppler broadening due to thermal motion of the nuclei, already discussed before. This is the reason why we designate this as a further Doppler broadening. However, in the text to follow, for simplicity, this will be referred to as Doppler broadening. In order to perform the Doppler broadening technique, thermal methods are usually applied. This means heating up the source and/or absorber or scatterer. In this case, the broadened width would overcome the huge difference in nuclear recoil, depicted in figure 1.6. In other words the FWHM of fluorescence and absorption lines

would greatly increase and eventually these two lines would overlap to some degree. Later, we will see that in practice, only fluorescence FWHM increases and overlaps with the absorption width. This is because, in practice, the source is heated only, while absorber and/or scatterer is kept at room temperature. However, for Doppler shift, three methods will be discussed. Those are: the centrifuge method, the preceding radioactive decay method (radioactive source method) and the nuclear reaction (proton capture reaction) method. Metzger [60] summarized all these, nicely in his report in "Progress in Nuclear Physics".

On the other hand, we can classify these methods differently, by the resonance energy and nuclides involved. As mentioned, the Doppler broadening method is in the same group as the centrifuge method, since both require resonance gamma rays of energies under $500keV$ and heavy nuclides ($A > 150$). The case of Doppler broadening (thermal method) can be explained by recalling the equations for nuclear recoil energy and Doppler width due to thermal motion; 1.16 and 1.29, respectively: $E_r = \frac{E_\gamma^2}{2Mc^2}$ and $\Delta = E\sqrt{\frac{2kT_{eff}}{Mc^2}}$. From equation 1.29, it is obvious that the value of Doppler broadening increases with a square root of the T_{eff} in K. In other words if the source temperature is increased from $25°C$ ($298.15K$) to $1000°C$ ($1273.15K$), the Doppler width is doubled. Note, that for simplicity, we will not go into Debye temperature corrections. In the case of reasonably small E_r values, doubling the FWHM of one of the lines is sufficient to compensate for this difference. Equation 1.16 directly dictates the value of nuclear recoil. Simply, relatively small resonance energies, paired with relatively heavy nuclides produce desirably small nuclear recoil values. Also, note that thermal agitation has its own practical limitations, because it is directly dependent on the temperature. Usually for these

types of experiments the temperature of the source can go up to $1200°C$. A good example for thermal agitation scattering experiment is the first excited state of ^{198}Hg, sitting at $411keV$ above the ground. Here, it is evident that the conditions of a heavy nuclide and low resonance energy are satisfied. For this excited state, the nuclear recoil energy is $0.46eV$, thus the difference between fluorescence and absorption lines is $0.92eV$. At the same time, the Doppler broadened FWHM due to the thermal motion is $0.36eV$ [3]. This is pictured in figure 1.7 [3].

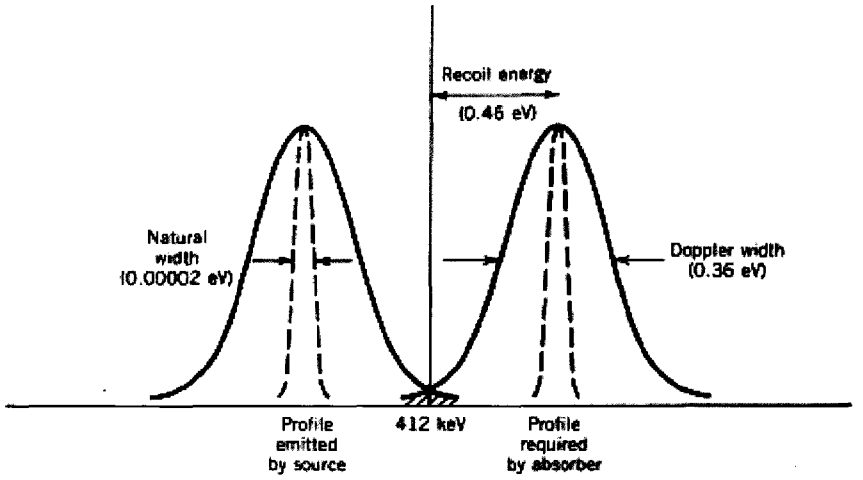

Figure 1.7: Fluorescence and Absorption Lines of $411keV$ ^{198}Hg First Excited State [3]

Metzger did nuclear resonance scattering experiments, using thermal agitation of a mercury source [70]. In fact the source was ^{198}Au that was converted to excited ^{198}Hg, via β^- decay. The source temperature was $1125°C$. This would approximately double the fluorescence FWHM. From figure 1.7, it is evident that doubling the FWHM of the fluorescence line will cause significant overlap with the absorption line. The purpose of this particular experiment was to measure angular distribution of resonance radiation. The experimental

arrangements are similar to one depicted in figure 1.10. The detector used for measuring radiation is shielded from the direct beam. One has to be careful with these types of experiments, because the cross section for elastic scattering at these low energies is a significant factor and it is in direct competition with resonance scattering cross section. This fact is handled by finding the optimal angles and comparing the results with scatterers of similar physical properties. Metzger also did resonance scattering studies in ^{72}Ge and ^{74}Ge, using ^{72}As and ^{74}As liquid sources [4]. He observed the $835keV$ excited state of ^{72}Ge and the $596keV$ excited state of ^{74}Ge. Figure 1.8 shows the $835keV$ line with Ge and corresponding Zn scatterer material. We can see the expected experimental outcome, i.e. no resonance scattering is observed with the Zn scatterer. As mentioned, for this type of experiment, it is important to choose an appropriate competitive scatterer that has very similar cross section for elastic scattering to the scatterer of interest. This is achieved by choosing an element of approximately the same atomic number as the scatterer of interest. This way one is able to distinguish elastic scattering from nuclear resonance scattering. Since this case involves lighter nuclei and higher energy gamma rays, Metzger also proved that Doppler broadening due to source thermal agitation only, was not sufficient for resonance effects to be seen. Rather this was a combination of thermal agitation and preceding radioactive decay method (Doppler shift method). Hence, in this case we are dealing with thermal Doppler broadening combined with Doppler shift.

The next important method involving light nuclei and low energy states is the centrifuge method. In this case we observe Doppler shift only, rather than Doppler broadening. The Doppler shift is due to the moving source.

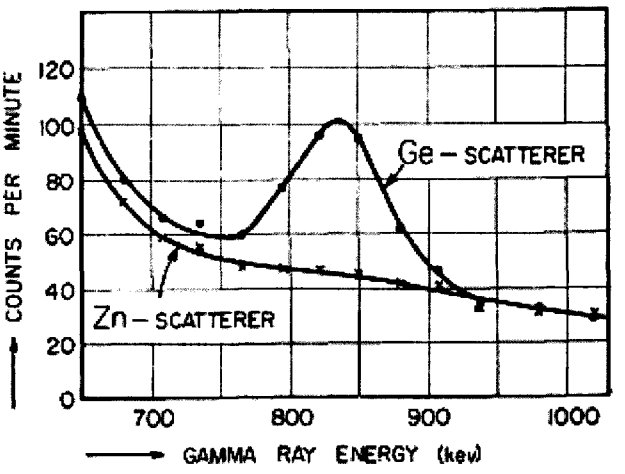

Figure 1.8: $835keV$ Gamma Line Observed with Ge and Zn Absorbers [4]

The source moves toward an absorber with high speed. The high speed of the source is achieved by fixing the source on the tip of the centrifuge rotor. Recalling equation 1.27, that represents shifted Doppler energy of the moving source and using the expression for the nuclear recoil energy, we can easily derive a simple expression for the source speed that is enough to overcome the Doppler shift of $2E_R$:

$$v = 2c\frac{E_R}{E_\gamma} \tag{1.41}$$

A typical experimental arrangement is depicted in figure 1.9. As mentioned, this method is restricted by the number of revolutions per minute of the rotor and hence optimal speed of the source. Typical source speeds are approximately $700m/s$, produced by $10^4 - 10^5 rpm$ [3]. This is sufficient for scattering experiments with ^{198}Hg. In fact, Moon and Storruste [71] did this experiment where they measured the half-life of the $411keV$ state to be $80ps$. Moon also did experiments with another heavy nuclide; ^{181}Ta and its $480keV$

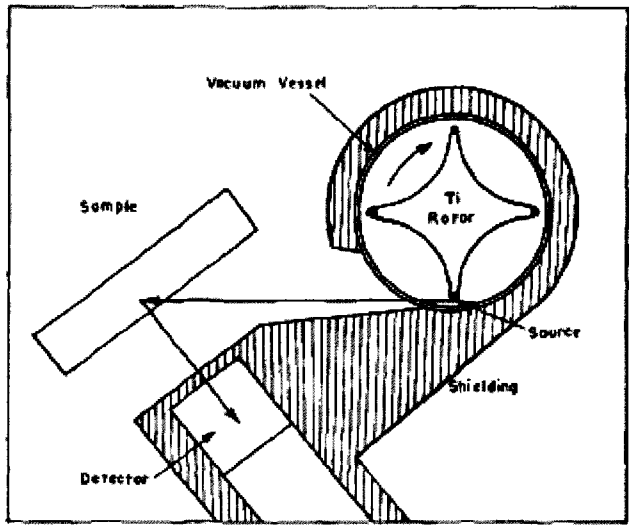

Figure 1.9: Nuclear Resonant Scattering Centrifuge Method [5]

transition [72]. Furthermore, Knapp did centrifuge scattering experiments with the second excited state of ^{199}Hg [73]. This is a $209keV$ transition with a mean-life of $(78 \pm 12)ps$.

Finally, the next two methods of interest are **preceding radioactive decay method** and **proton capture method**. They are common for light nuclei and gamma resonance energies above $500keV$ and they are both based on the Doppler shift of the fluorescence line. Before we go into a more detailed description, we have to mention that preceding radioactive decay method together with thermal agitation and centrifuge can be even further classified into two different experimental techniques. One has been already discussed and this is resonance scattering experiment. The usual experimental arrangement is given in figure 1.10. The other one is self-absorption experiment that involves scatterer and absorber as well. The typical arrangement of this experiment is given in figure 1.11. Lastly, proton capture method differs from

the above two and it is performed using resonance absorption (transmission) experiments. The experimental arrangement for this method is depicted in figure 1.12

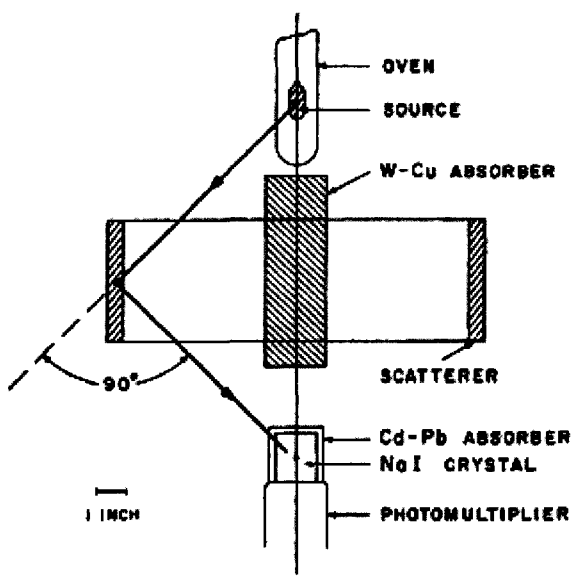

Figure 1.10: Nuclear Resonant Scattering Experiment [6]

As discussed, the last experiment, particularly $^{27}Al(p,\gamma)^{28}Si$ reaction is the integral part of the thesis and thorough elaboration will be given in the chapters to follow, as well. Self absorption and scattering experiments are indeed similar and this is evident from the experimental arrangements. The main difference is the presence of absorption material in the self-absorption experiment. The idea of both experiments is to measure (or quantify) the amount of nuclear resonance absorption (or scattering). After the event is observed and measured, the value can be related to the width of an energy level under investigation [74] [75] [76] [6]. Furthermore, an angular distribution of the scattered gamma rays can be measured [76] [6] [74]. As discussed, in

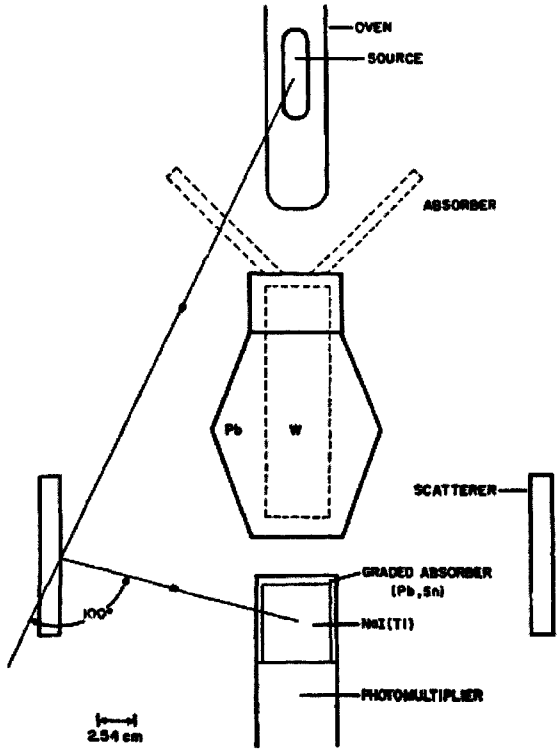

Figure 1.11: Nuclear Resonant Self-Absorption Experiment [7]

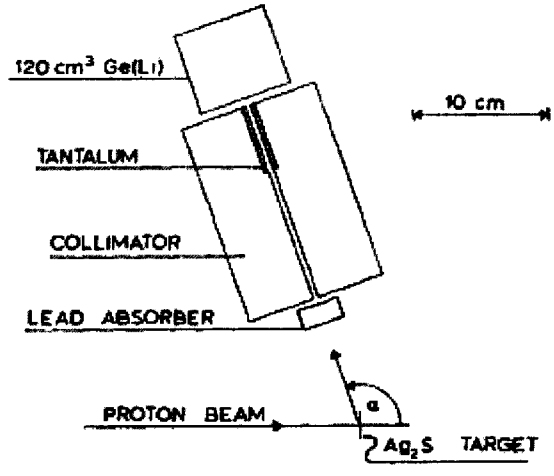

Figure 1.12: Nuclear Resonant Absorption (Transmission) Experiment [8]

the scattering case, usually two experiments are performed; one with resonant scatterer and the other without resonant scatterer. The typical outcome is described in figure 1.8. Interestingly, in self-absorption case, one more experiment is performed, on the top of these two [9]:

- resonant scatterer paired with non resonant absorber
- resonant scatterer paired with resonant absorber
- non resonant scatterer paired with non resonant absorber

The last experiment will yield no signal of interest at all, since no resonantly scattered radiation can be observed. The first experiment will yield the largest signal, since a non resonant absorber cannot contribute to further resonant scatter and thus no loss of gamma rays will be observed. Finally, the second experiment will give a smaller signal, because, a resonant absorber will cause previously scattered radiation to scatter further resonantly and thus, it would decrease a gamma fluence rate to the detector. Rust et al. [9] performed self-absorption experiments with $771keV$ level of ^{65}Cu and $439keV$ level of ^{23}Na. Some of the results from this study are given in figure 1.13. The radiation source used was a Compton scatter from a $4000Ci$ ^{60}Co source. It can be seen that in both ^{65}Cu and ^{23}Na experiments, the highest signal was present when experiment with resonant scatterer and non resonant absorber was conducted. Essentially, no gamma peak is seen in the third experiment. Moreover, Hough and Mouton [77] used a very similar idea and Bremsstrahlung radiation from a $1.4MeV$ electron accelerator source in order to induce self-absorption experiments in ^{27}Al, ^{31}P, and ^{35}Cl. They were looking for mean life-times of

the ground state transitions in these nuclides from levels: $1.01MeV$, $1.26MeV$ and $1.22MeV$, respectively. The results are very similar to the one obtained by Rust et al. and given in figure 1.13.

Another interesting method used for overcoming a differences in E_r is preceding radioactive decay method. In this case a nucleus that emits a resonance gamma ray is set in motion by preceding radioactive decay. Vartsky et al. used this process to measure body iron [78] and hepatic copper [79]. Also, Kelly and Beard [80] and Begzhanov et al. [81] used the same technique to estimate mean life time of the first excited state of iron. In the case of iron, usually a heated gaseous $^{56}MnCl_2$ source is used. The ^{56}Mn decays via β transition to the first excited state of ^{56}Fe, which is at $847keV$ above ground. This excited iron becomes the gamma source for further resonance excitation of ground state iron in the sample of interest. In the case of copper, a $^{65}ZnI_2$ gaseous compound is used. The ^{65}Zn decays via electron capture to the excited ^{65}Cu. The excited copper becomes the source. The source in iron case is set in motion by conservation of momentum resulted from previous β decay. However, in the case of copper, due to excess of negative charge, a $^{65}ZnI_2$ molecule will undergo Coulomb fragmentation and resulting ^{65}Cu source is set in motion via Coulomb repulsion. Also, in both cases, the source is heated so that emission line is further broadened.

Finally, we will discuss an experimental method used in this thesis, based on **Doppler shift** and induced by a nuclear reaction, i.e. proton capture. In order for the Doppler shift method to work, a radiation emitter (decaying nucleus) must be in motion. For this particular case, a decaying nucleus is set

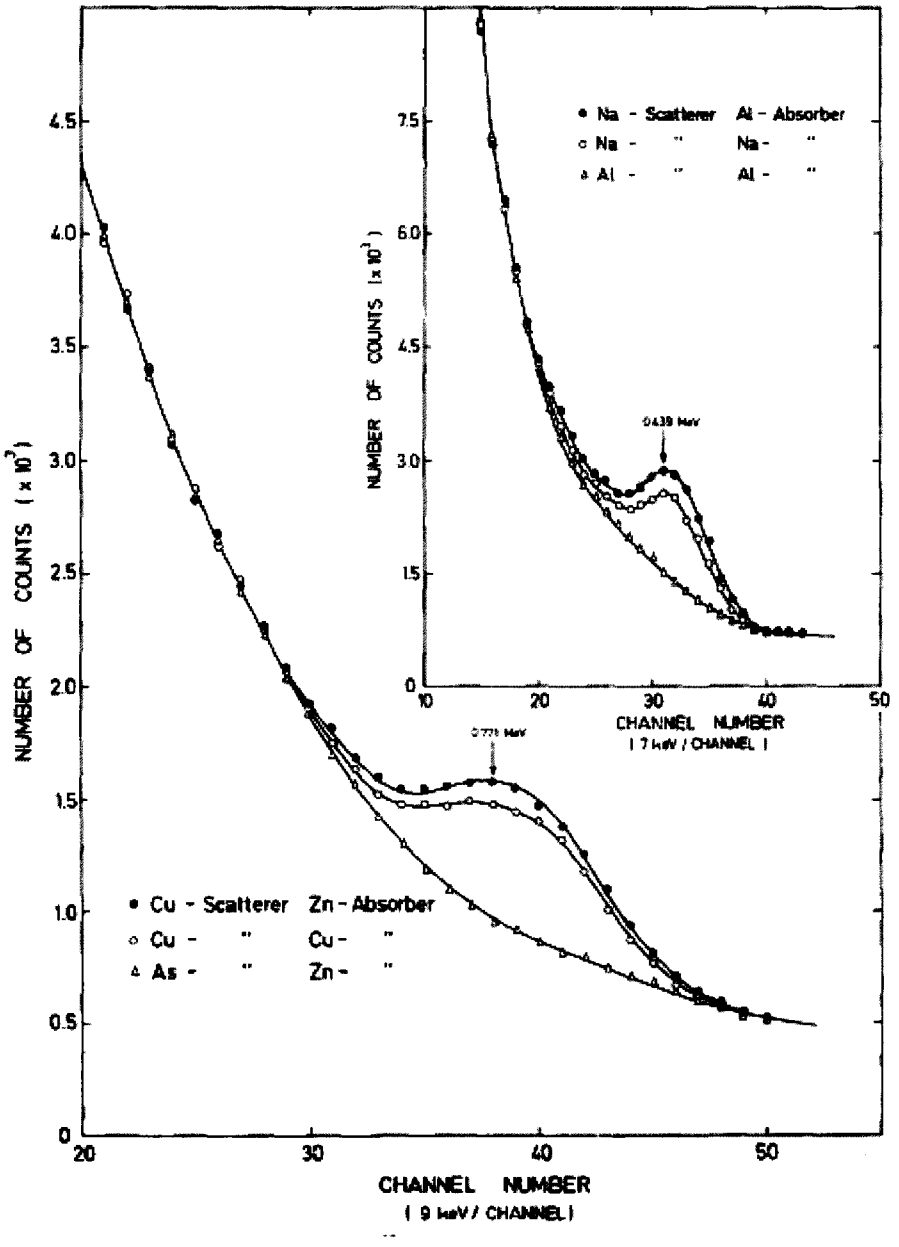

Figure 1.13: Example of Self-Absorption Experimental Results [9]

in motion by the captured proton. A proton carries its own kinetic energy and gets captured by a stationary nucleus. By, conservation of linear momentum, we can easily come to the relationship:

$$V = \frac{\sqrt{2E_p m_p}}{M} \tag{1.42}$$

Where E_p and m_p are kinetic energy and mass of incoming proton, respectively and M and V are the mass and velocity of bombarded nucleus (following proton capture). When a proton is captured and a nucleus starts to move in the direction of that proton, it will decay. The crucial part is the shortness of a mean-life of this new nucleus in motion. In our case, a nucleus of Al is stationary and nucleus of excited Si is in motion. An emitted gamma ray is "launched" from a moving source and this will create a "micro-spectrum" of gamma rays, from the perspective of a receiver (an absorber located at some particular angle with respect to the line of motion) [78]. A Doppler shifted energy (or energy increment) of the released gamma ray is dependent on angle α and given by:

$$\Delta E = \frac{V}{c} E_0 cos\alpha \tag{1.43}$$

Where E_0 is original energy of gamma ray released. Therefore, an absorber nucleus located at different angles from a line of motion perceives a different portion of this gamma "micro-spectrum", that is dependent on angle α. On the other hand, we saw in section 1.3 that in order for NRF/NRA to work, we have to overcome the energy difference of two recoils, or $\frac{E_0^2}{Mc^2}$. In other words, when this difference is equal to the energy increment caused by Doppler shift; equation 1.43, the condition is fulfilled. Thus, substituting equation 1.42 into

equation 1.43 and equating it with $\frac{E_0^2}{Mc^2}$, we end up with an expression for a Doppler angle α:

$$cos\alpha = \frac{E_0}{\sqrt{2E_p m_p c^2}} \tag{1.44}$$

A typical transmission curve centered at angle α is given in figure 1.14. This is Si $12.33MeV$ resonance populated by $771keV$ protons [10]. The reaction is: $^{27}Al(p,\gamma)^{28}Si$, as discussed.

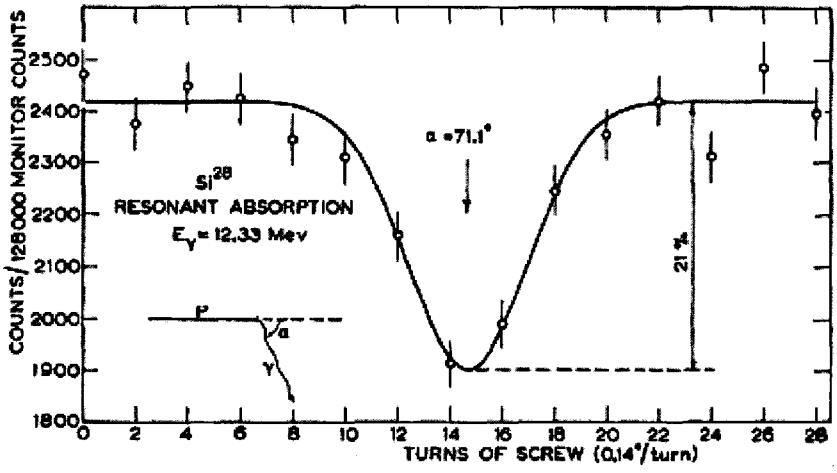

Figure 1.14: Nuclear Resonance Absorption Curve Obtained by Smith and Endt [10]

There are number of important studies that observed a Doppler shift correction using a proton capture experiment. One of the strongest (p,γ) resonances comes from the $^{13}C(p,\gamma)^{14}N$ reaction [82]. This is a $9.17MeV$ resonance, populated by $1.75MeV$ protons, with $\alpha = 80.8°$. Hanna and Schützmeister [83] measured this resonance in 1959. They obtained transmission curves for different absorber thicknesses in order to measure the strength of a resonance as a function of these thicknesses. Later, in 1981, Biesiot and Smith [82] performed similar experiment, where they found a width of the $9.17MeV$ level to

be $(135 \pm 8)eV$. Vartsky et al. in 1989 did the same experiments and obtained a slightly smaller value for the total width; $(122 \pm 8)eV$. Wielopolski et al. [84] proposed the method for human body composition studies, based on several capture reactions, for detection of nitrogen, calcium, chlorine, oxygen, carbon and phosphorus. Furthermore, at McMaster University, in 2000 Vartsky et al. [31] used the method for feasibility study for *in vivo* measurements of nitrogen. The goal was to measure nitrogen content in different phantoms. For example, they managed to measure $(3.9 \pm 0.14)\%$ of nitrogen in a meat phantom, while the true concentration was 3.46%. The radiation dose from this particular experiment was measured to be $9\mu Sv$. Finally, Vartsky et al. [85] used the method in order to detect nitrogen in a cargo, that would be an indication of possible presence of explosives. The other important nuclide used in proton capture experiments is ^{40}Ca. The reaction of interest is $^{39}K(p,\gamma)^{40}Ca$, induced by protons of $2.05MeV$, populating resonance at $10.3MeV$. Eckert and Shrader [64] found a total width of this energy level to be $(10.3 \pm 1.7)eV$. Later, Mu et al. [86] performed similar experiments and used another important line of calcium: $9.604MeV$, together with the $10.3MeV$ line. They found a great discrepancy with the previous study. Namely, they reported a width of $(91 \pm 15)eV$ for the $10.3MeV$ level and $(188 \pm 47)eV$ for the $9.604MeV$ level.

Finally, for further reference purposes, we are going to mention two other experiments performed, but we will not discuss them, since the purpose of conducting those experiments was the same. Those are: $^{26}Mg(p,\gamma)^{27}Al$ [87], $^{30}Si(p,\gamma)^{31}P$ [88] [89]. Lastly, the experiments on which this particular work is based is: $^{27}Al(p,\gamma)^{28}Si$ reaction. They were performed by Smith and Endt [10], targeting the $12.33MeV$ resonance state, which is populated by $771keV$

protons. They reported a total width of this state to be: $(9.0 \pm 0.8)eV$. The ultimate goal of this thesis is to study this particular reaction at the McMaster KN Accelerator and to evaluate the feasibility of using it in detection of *Si in vitro* and possibly *in vivo*. This is a similar approach that Vartsky [31] and Wieloposki [84] suggested for detection of nitrogen. However, since this is the first attempt to use the $^{27}Al(p,\gamma)^{28}Si$ reaction for these purposes, a detailed pure experimental exploration (from the ground level) had to be performed in order to assess it properly. Chapters 2, 3 and 4 describe all relevant experimental findings and obstacles, as well as lessons learned during the course of this work.

Chapter 2

Preliminary Experiments: Thick Target Nuclear Gamma Ray Yield from the Reaction: $^{27}Al(p,\gamma)^{28}Si$

2.1 Brief Literature Review and Experimental Methods Used

The preliminary experiments of this study were done in order to assess the McMaster KN Accelerator experimental site. In particular, total thick target gamma ray yield experiments were performed. As mentioned, the whole idea was based on the nuclear reaction: $^{27}Al(p,\gamma)^{28}Si$. The experimental setup was very simple. A pure, thick Al target (99.999% purity) was bombarded with accelerator protons. In general, for different experiments, the proton current on target was varied from approximately $5\mu A$ to a maximum of $60\mu A$. In addition, a nominal proton current of $60\mu A$ is indeed a maximum output of this particular machine. Moreover, two types of gamma detectors were used; Hyper Pure Germanium (HPGe) and sodium iodide (NaI) scintillator, depending on

experimental setup and the goal that we wanted to achieve. The first one was 30% relative efficiency, coaxial n-type detector, while the second one was large NaI 6" $\times$ 6" scintillator. In general, a gamma ray yield was obtained, simply by integrating total, or partial gamma spectra, with subtraction of appropriate background collected while the KN accelerator was down. The results were normalized to the total charge collected on the target. Correction for the dead time was applied and yield was presented in the units of $counts/\mu C$, or $(counts/600s)/\mu C$. The purpose of the thick target is to be able to collect all the resonances that are located below the incoming proton energy and to obtain a summed gamma yield from all of them. Therefore, by increasing the proton energy, gamma yield should increase steadily, since more resonances are included. The general prediction is that gamma yield should increase in step-like fashion, depending on the energy resolution and stability of the accelerator. For instance, the better the resolution of the accelerator, the more the total gamma yield curve resembles a step like increase, since in this case it is possible to have several measurements before a neighbouring resonance is reached. Those measurements will yield identical gamma spectra, until the proton energy is increased to include a higher, neighbouring resonance. Once this resonance is included (reached), the total yield will start to increase. Furthermore, the gaps between consecutive resonances play important role in determining the shape of the yield curve. Particularly, the larger the energy gap between a neighbouring resonances, the more likely that a step-like gamma yield curve will be obtained and a larger plateau in yield curve will be seen. Timmermann et al. were able to observe a thick target total gamma yield from a single $1.78MeV$ line, between $200keV$ and $360keV$ of proton incoming

energy, in the increments of $5keV$ [11]. These experiments were done in order to target resonances located at $11.782MeV$, $11.801MeV$, $11.869MeV$ and $11.901MeV$, which are populated by protons of energies: $203keV$, $223keV$, $293keV$ and $327keV$, respectively. Evidently, energy gaps between these resonances are: $20keV$, $70keV$ and $34keV$, so that the number of data points that can be taken between neighbouring resonances in this case is: 4, 24 and 6, respectively. Hence, accelerator energy resolution of $5keV$ is sufficient for this experiment. Interestingly, at these proton energies, a $^{27}Al(p,\gamma)^{28}Si$ reaction of interest is in direct competition with $^{27}Al(p,\alpha\gamma)^{24}Mg$ reaction. We will elaborate more on these competing reaction channels later in the chapter. At this stage, the important fact is the gamma yield curve obtained by Timmermann et al. [11] and given below in figure 2.1

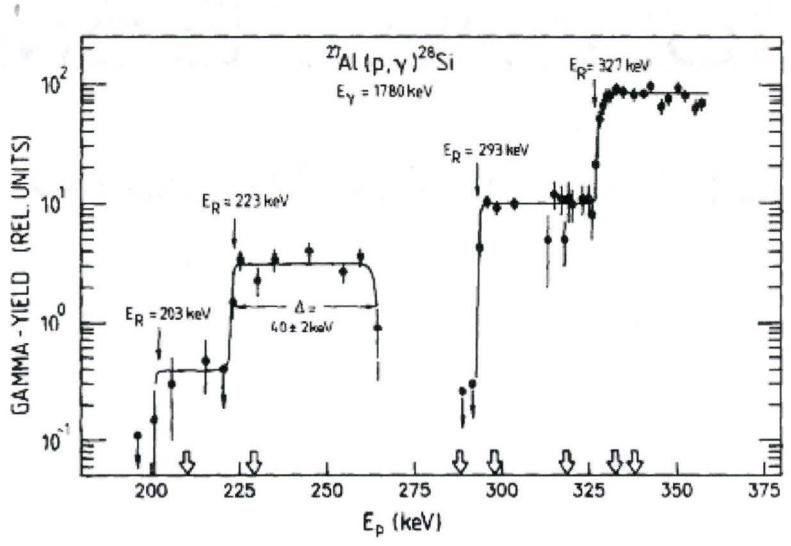

Figure 2.1: Thick Target Gamma Yield for 1.78 MeV Line [11]

As discussed a step-like yield function is obtained, because of the small proton energy incremental step compared to relatively large energy gaps between

consecutive resonances. Similar results were obtained by Demortier et al. [12], where they have targeted higher energy resonances at $12.542MeV$, $12.552MeV$ and $12.574MeV$, which are populated by protons of energies $992keV$, $1002keV$ and $1025keV$, respectively. The proton energy incremental step in these experiments was only $1keV$, hence indicating excellent resolution of the accelerator used in the experiments. The obtained gamma ray yield curve is given in figure 2.2.

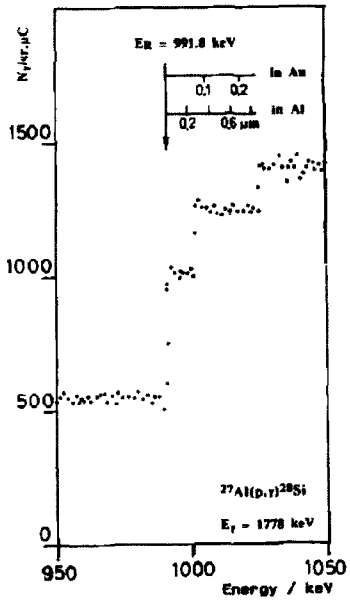

Figure 2.2: Thick Target Yield from $^{27}Al(p,\gamma)^{28}Si$ Reaction, around $1MeV$ Proton Energy [12]

Evidently, the step-like feature is even more prominent in this case, since accelerator energy resolution was indeed outstanding. By contrast, Fink et al. [13] did similar experiments with much higher proton energies from $1.75MeV$ to $4MeV$, and considerably larger increment step of $250keV$. Moreover, they calculated a total gamma yield by integrating a whole gamma spectrum, from

$5.5MeV$ and up (above $13MeV$) and also from $9.5MeV$ and up. Finally, this was done for 0° and 90° geometries. The results of these experiments are summarized below in figure 2.3.

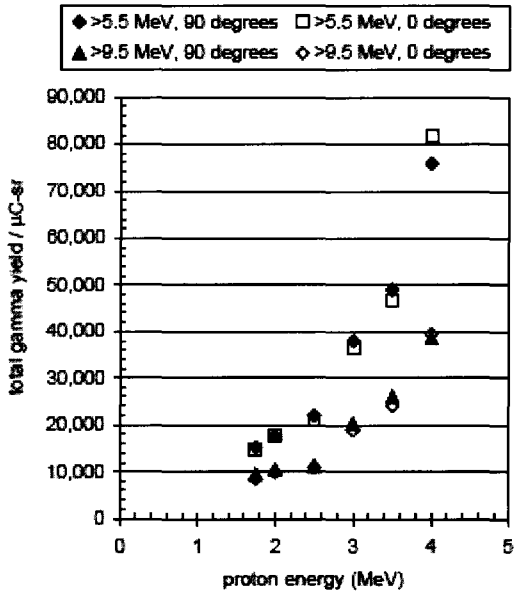

Figure 2.3: Total Integrated Gamma Yield above $5.5MeV$ and above $9.5MeV$ as a Function of Proton Energy [13]

Also, the actual total gamma spectra from this study, taken with NaI detector are given in following figure; 2.4. As predicted, total gamma yield function increases steadily, however no step-like features are observed, mostly because of high proton energy increments of $250keV$.

Lastly, in this section we are going to mention another very interesting study conducted by Savidou et al. [14]. They have used protons of energies between $1.0MeV$ and $4.1MeV$ in order to observe gamma yields in a large set of light elements: Li, B, F, Na, Mg, Al, Si and P. They were looking for different reactions, induced by proton bombardment of these elements. Those

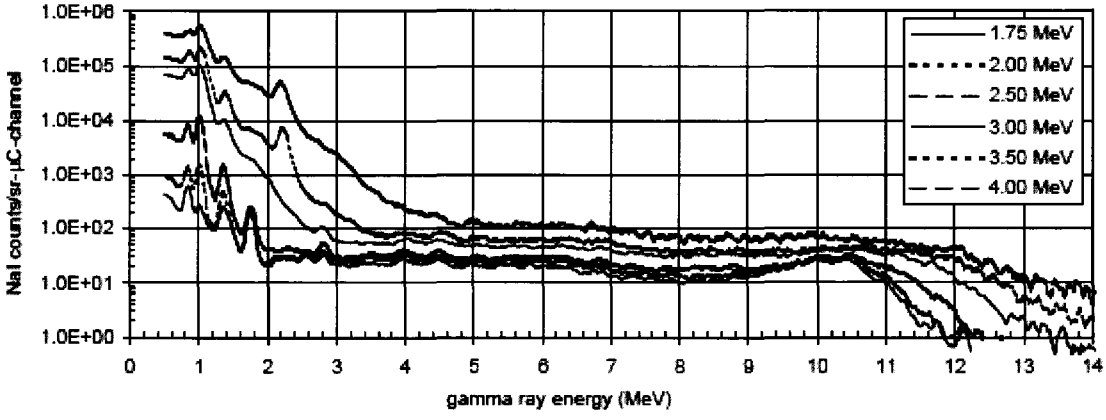

Figure 2.4: NaI Detector Gamma Spectra for Different Proton Energies [13]

are: $(p, p'\gamma)$, $(p, \alpha\gamma)$, (p, γ), $(p, n\gamma)$. The reason for this is to quantify the amount of light elements in different material using PIGE (Proton Induced Gamma-ray Emission). We have already mentioned in the first chapter, that XRF techniques are practically impossible to use for quantification of light elements due to low energy of X-rays produced, large absorption coefficients and thus very low probability of detection of these X-rays. More detailed discussion on this study (and also on similar studies) is given in the final chapter of this work. As will be seen, the PIGE technique will be proposed as one of the alternatives for detection of light elements *in vitro*. In this article, Savidou et al. [14] used a HPGe detector, so that a high detection resolution was achieved, since a large number of different high intensity gamma rays were observed. Proton energy was increased in steps of $10keV$ between $1.0MeV$ and $1.82MeV$ and in steps of $50keV$ between $2.2MeV$ and $4.1MeV$, depending on the element observed and the reaction induced. At this stage we will consider two findings of this study. Figure 2.5 represents gamma yield from a single $1.78MeV$ line from reaction $^{27}Al(p, \gamma)^{28}Si$. The proton energy

span was between $1.0MeV$ and $1.8MeV$. Similarly, figure 2.6 represents a $1.014MeV$ gamma ray yield from reaction $^{27}Al(p,p'\gamma)^{27}Al$, between proton energies of $2.0MeV$ and $4.1MeV$.

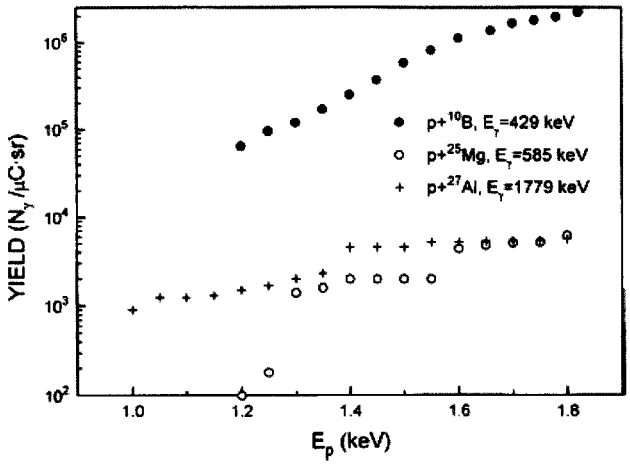

Figure 2.5: Thick Target Gamma Yield for B, Mg and Al $(1.78MeV)$ at Proton Energy Range $1.0MeV$-$1.82MeV$ [14]

From these two figures, we see that gamma ray yield of interest increased much more rapidly in the latter reaction; 500 times, compared to only 5 times in the former reaction. This is very important finding, because a very similar experiment was conducted during this research and also similar results were obtained. Indeed, this experiment is described in the last section of this chapter.

2.2 Experimental Set 1; Preliminary Runs

All the runs in this experimental set lasted for $600s$ real time. The total charge was collected during that time and final results were normalized to

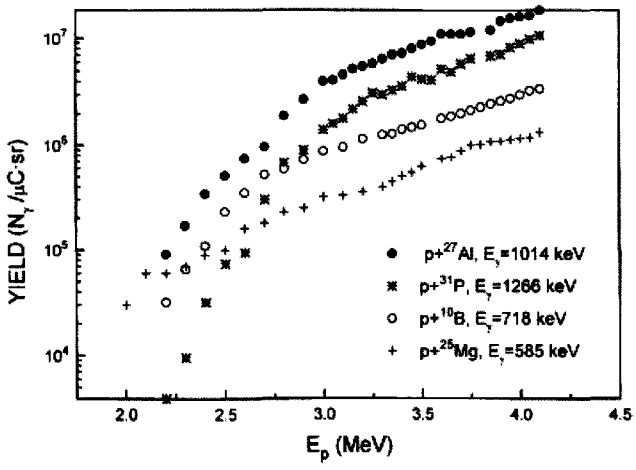

Figure 2.6: Thick Target Gamma Yield for B, Mg, P and Al ($1.014MeV$) at Proton Energy Range $2.2MeV$-$4.1MeV$ [14]

this total charge and corrected for the dead time, so that gamma ray yield was interpreted in the unit of $(counts/600s)/\mu C$. The detector used was the large NaI scintillator described earlier in the chapter. The distance between detector and target was approximately $30cm$ (0° geometry), with a total proton current on the target varying between $37\mu A$ and $48\mu A$. The very first set of runs consisted of seven experimental points taken between $600keV$ and $900keV$ of proton kinetic energy. The incremental step in this case was $50keV$. The energy uncertainty of the KN accelerator is $10keV$ and this is indicated as an x error bar. It has to be mentioned at this point that uncertainty of $10keV$ is indeed large, compared to energy resolution of $5keV$ or furthermore, the phenomenal $1keV$ achieved elsewhere and discussed in this chapter. Even from these first experiments, we can conclude that there are certain limitations to the KN machine used. Chapters 3 and 4 will deal with this issue in detail. Figure 2.7, represents a compilation of total gamma yield taken from $1500keV$-

up and $4500keV$-up. With described scintillator and present electronics, we were capable of collecting gamma spectrum up to $9MeV$, approximately. Furthermore, gamma ray yield for a single $1.78MeV$ line is included in the figure.

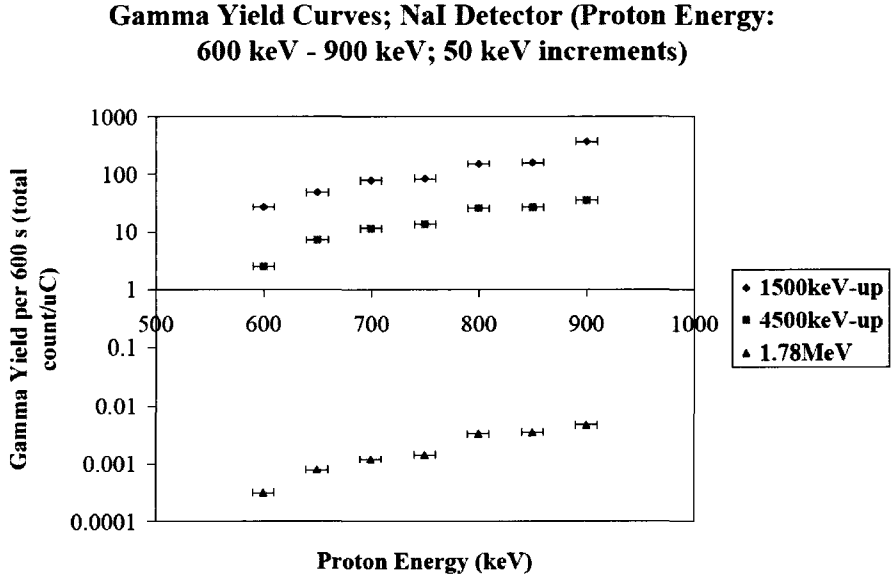

Figure 2.7: NaI Detector Total Gamma Yield Curves; Proton Energy $600keV-900keV$

All three curves possess very similar shape and constant yield increase is observed as a function of proton energy. As expected, not very prominent steps are observed, since a small proton energy range was targeted and also a relatively large energy step of $50keV$ was used. The important fact is a presence of a constant and monotonic increase, which is in agreement with similar experiments described in literature [13] [14] and given in figures 2.3 and 2.5. The next experiment contained 17 points between $1500keV$ and $2300keV$ of proton kinetic energy with usual increments of $50keV$. This way we have targeted higher energy resonances. The experimental arrangement was the same as in the previous case. The proton current varied between

$0.2\mu A$ and $4\mu A$. Evidently, this was significantly lower proton current output. However, in order to keep a proton beam stable, as a terminal voltage is increased, the current had to decrease accordingly. The result is given below in figure 2.8. Finally the last experiment in this set involved proton energy increments of $25keV$ and proton energy span between $1250keV$ and $1625keV$ or 16 experimental points in total. For this case the proton currents varied from $2\mu A$ to $24\mu A$. The results of the described experiments are given below in figures 2.8 and 2.9.

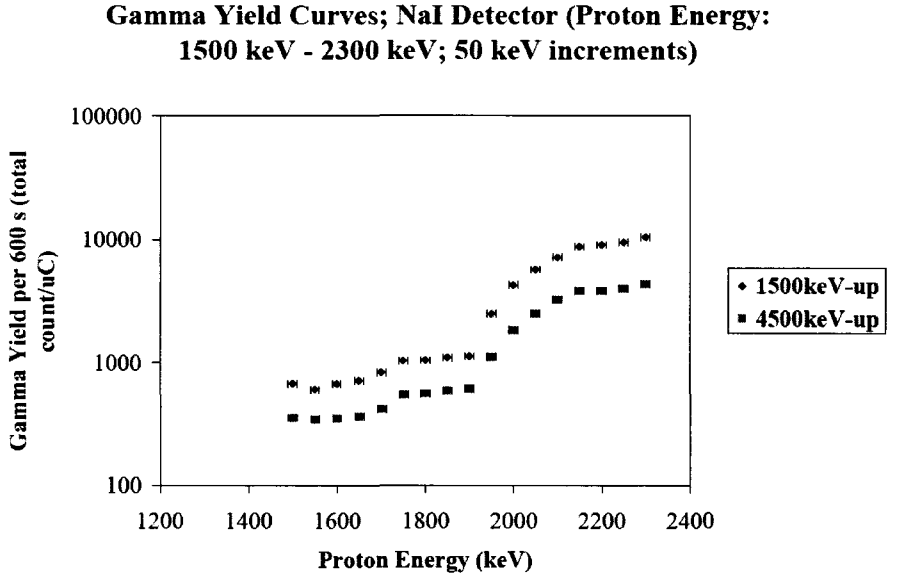

Figure 2.8: NaI Detector Total Gamma Yield Curves; Proton Energy $1500keV - 2300keV$

Both figures contain a step-like feature, as expected. A very prominent step is seen in figure 2.9. This is a logical outcome, since incremental step was much smaller in this case; only $25keV$, compared to $50keV$ in the previous experiments. Again, constant gamma yield increase is seen in both experiments,

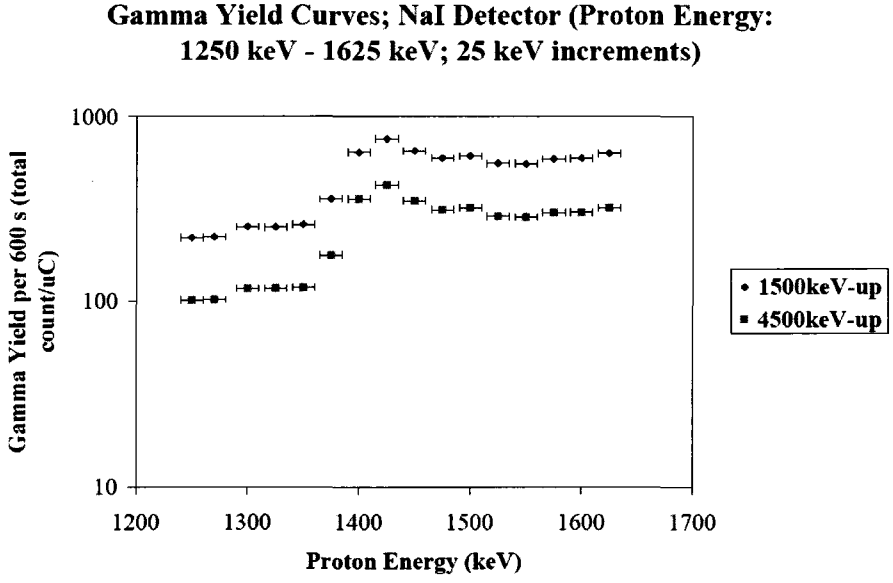

Figure 2.9: NaI Detector Total Gamma Yield Curves; Proton Energy $1250keV - 1625keV$

with a notable plateau in figure 2.9. Further yield experiments are described in the next section

2.3 Experimental Set 2

The following two experiments were actual sequels of the previous set of experiments. They involved two identical repetitive experiments. The distance between NaI detector and proton target was fixed at $45cm$. In both cases, the proton increment was $50keV$ and proton energy span was between $850keV$ and $2150keV$ in the first experiment and $800keV$ and $2250keV$ in the second experiment. In total, 26 and 30 experimental points were collected, respectively. The purpose of these runs was to include as many proton energies as possible and to observe an overall trend in a thick target gamma yield ex-

periments, over a much larger range of proton energies. This way, the stability of the accelerator was under an investigation, since a single data set has been collected during the course of one day. The results of these experiments are given below in figures 2.10 and 2.11

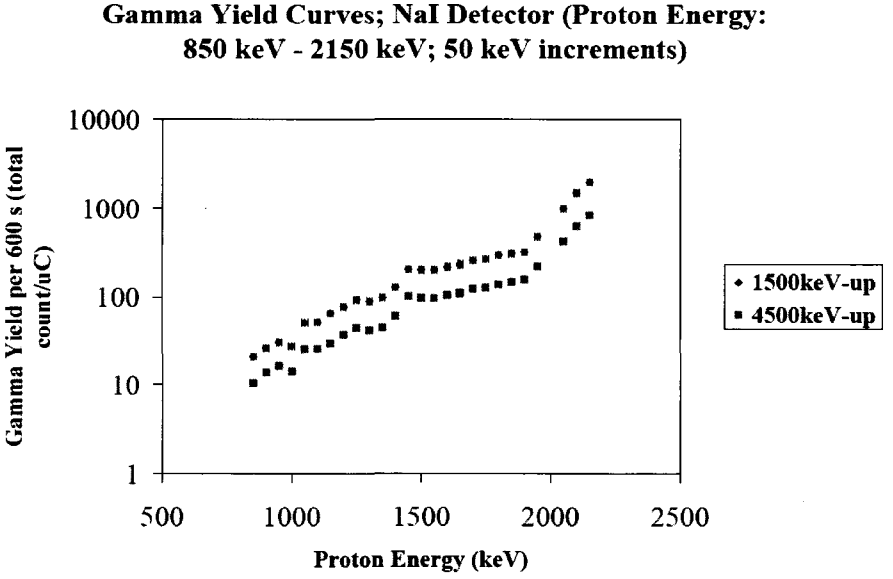

Figure 2.10: NaI Detector Total Gamma Yield Curves; Proton Energy $850keV - 2150keV$

Almost identical results were obtained in these experiments. Also, some plateau on a logarithmic scale was observed between $1550keV$ and $1950keV$ of proton energy in both cases. The important fact was that constant increment in gamma yield was observed as a function of proton energy, again. Furthermore, at this stage, a fair amount of accelerator stability was observed, because of very similar results in two independent experimental outcomes. Unfortunately, we will see later that this kind of accelerator stability and reliability was not observed all the time. This phenomenon is encountered later in the research and analyzed in chapters 3 and 4.

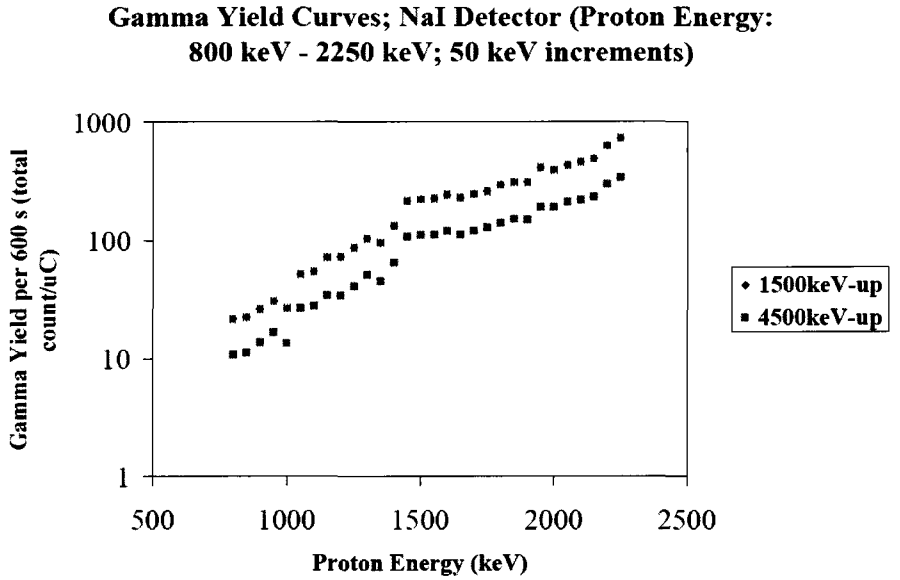

Figure 2.11: NaI Detector Total Gamma Yield Curves; Proton Energy $800keV - 2250keV$

2.4 Experimental Set 3

After extensive experimenting with the NaI detector, the HPGe detector was used in order to achieve desired energy resolution and search for a particular lines of interest. These gamma lines come from the above mentioned reactions that are in direct competition with the $^{27}Al(p,\gamma)^{28}Si$ reaction. Particularly, these are: $^{27}Al(p,p'\gamma)^{27}Al$ and $^{27}Al(p,\alpha\gamma)^{24}Mg$. Consequently, the first reaction produces gamma lines at $844keV$ and $1014keV$, while the second reaction produces a gamma line at $1369keV$. Savidou et al. [14] measured absolute yields from all these lines, using a HPGe detector that was calibrated for absolute efficiency. Also, they applied a correction for proton stopping power in different materials. In these experiments, the incoming kinetic energy of protons was $1.77keV$. From this study, relative yields can be expressed as follows: $1780keV : 1369keV : 1014keV : 844keV = 1.3 : 1.4 : 1 : 3.1$.

Recall that some of the results are summarized in figures 2.5 and 2.6. The experiments that we have performed were very similar, indeed. In our case, the distance between the accelerator target and HPGe detector was $23cm$, with a nominal proton current of approximately $6\mu A$. The proton kinetic energy was varied in increments of $50keV$ from $1600keV$ to $2300keV$. Below is figure 2.12 that represents yields from single gamma lines. Furthermore, the annihilation line is included in order to check the production of $511keV$ gamma rays as proton energy is increased.

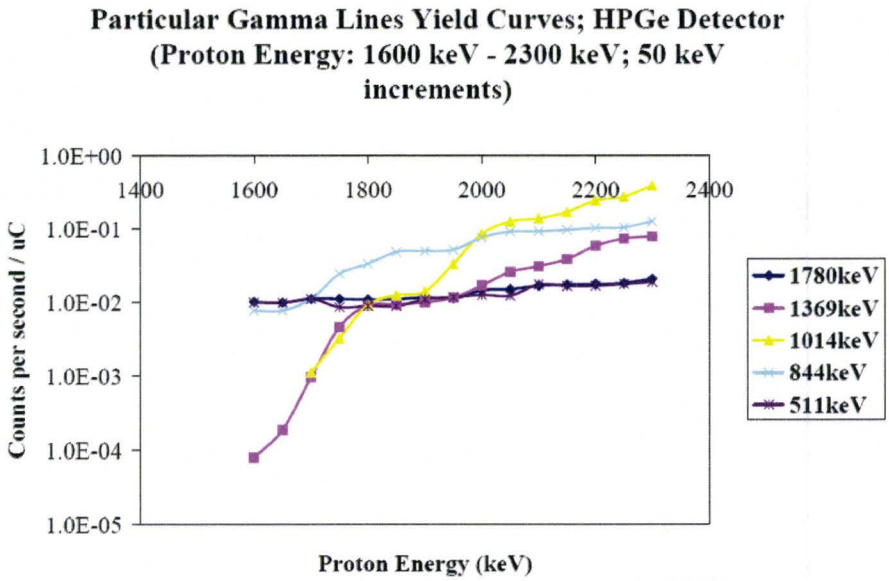

Figure 2.12: HPGe Detector Gamma Yield Curves; Proton Energy $1600keV - 2300keV$

Over the proton energy range, the $1.78MeV$ yield is fairly constant, which is in agreement with the study performed by Savidou et al. [14] and summarized in figure 2.5. Similarly, the production of annihilation radiation follows closely the trend of the production of $1.78MeV$ gamma rays, suggesting that the source of this radiation are high energy gamma rays produced in (p, γ)

reaction only. Obviously, the three other lines of interest are included in the figure. From this data set the yield ratio at $1.75MeV$ proton energy is as follows: $1780keV : 1369keV : 1014keV : 844keV = 3.4 : 1.4 : 1 : 7.4$, while at $1.80MeV$ the same ratio reads: $1.2 : 0.98 : 1 : 3.6$. The second reported ratio at $1.80MeV$ is in very close agreement with results obtained by Savidou et al. at $1.77MeV$ proton incoming energy. Even, the first ratio at $1.75MeV$ is in close agreement with literature results. This is very promising finding in terms of evaluation of the present equipment and accuracy of the experiments performed. Finally, the following figure represents a total gamma yield from these experiments. The total yield is integrated from $200keV$ to $8450keV$ and from $4500keV$ to $8450keV$.

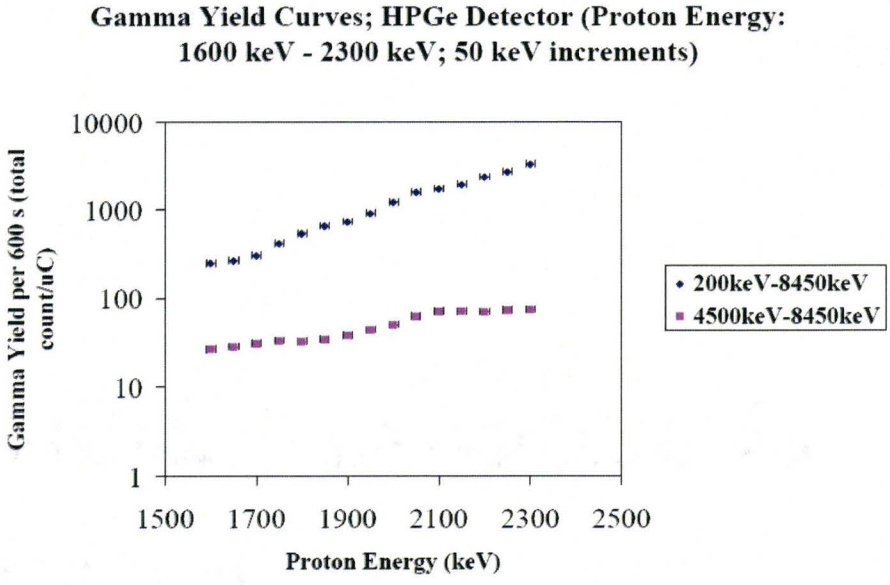

Figure 2.13: HPGe Detector Total Gamma Yield Curves; Proton Energy $1600keV - 2300keV$

The obtained results are as expected and very similar to the previous experimental sets. Moreover, yields from individual lines from various reactions

are in close agreement with the literature. These facts form a very strong basis for further exploration of $^{27}Al(p,\gamma)^{28}Si$ reaction and its usage for Si detection. The next chapter will deal with direct ground state transition of $12.33MeV$ resonance populated by $771keV$ protons.

Chapter 3

Nuclear Resonance Absorption Experiments Using $771keV$ Protons and Direct Ground State Transition of $12.33MeV$ Gamma Rays

As the title suggests, the $12.33MeV$ gamma line with 75% branching ratio to the Si ground state, populated by $771keV$ protons [10] was under investigation. Evidently, we were dealing with high energy gamma rays in this case. Since the line was yielded from a single resonance, the idea of the following set of experiments was to focus on that resonance and to avoid the other resonances. This was achieved simply by using a thin Al target. Essentially, this was a very similar experiment to the one conducted by Smith and Endt [10]. The nominal thickness of the target was $0.4\mu m$. Four targets were prepared by evaporating Al onto a copper backing. One of the very important issues in thin target yield experiments is the energy loss of the proton beam inside the target itself. One would agree that thinner the target is, better are the chances to hit a single resonance of interest and to avoid the other ones. Along

with a target thickness, the vicinity of other resonances plays an important role. In other words, if the resonance of interest is isolated enough on the energy scale, the chances are much better to avoid undesired resonances. Taking into the account the thickness of the Al target and using a total stopping power of protons in Al obtained from NIST [90], ranging from $761keV$ up to $781keV$ (increments of $1keV$), we can easily calculate loss of proton energy in the target. The stopping power function is given in figure 3.1.

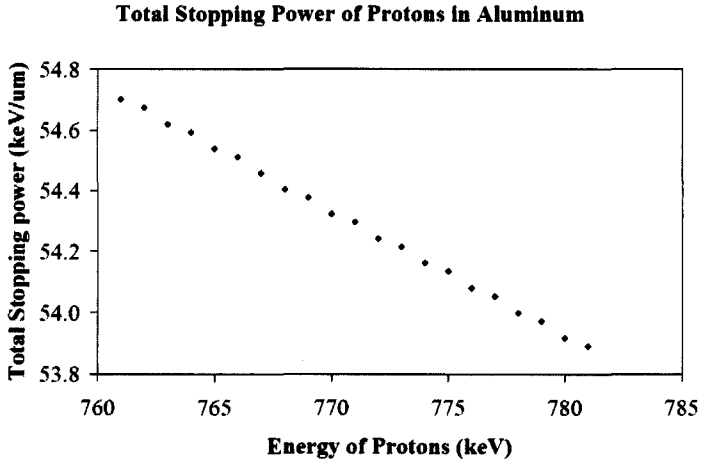

Figure 3.1: Stopping Power of Protons in Aluminum between $761keV$ and $781keV$

The stopping power is given by well known relationship:

$$S(E) = -\frac{dE}{dx} \tag{3.1}$$

Hence, the discrete case would read:

$$S(E) = -\frac{\Delta E}{\Delta x} = -\frac{E_{n+1} - E_n}{x_{n+1} - x_n} \tag{3.2}$$

Knowing the initial conditions; i.e. $E_0 = 781keV$, $x_0 = 0$ and $E_1 = 780keV$ we can easily construct discrete function $E(x)$, by iterative process. This is given in figure 3.2.

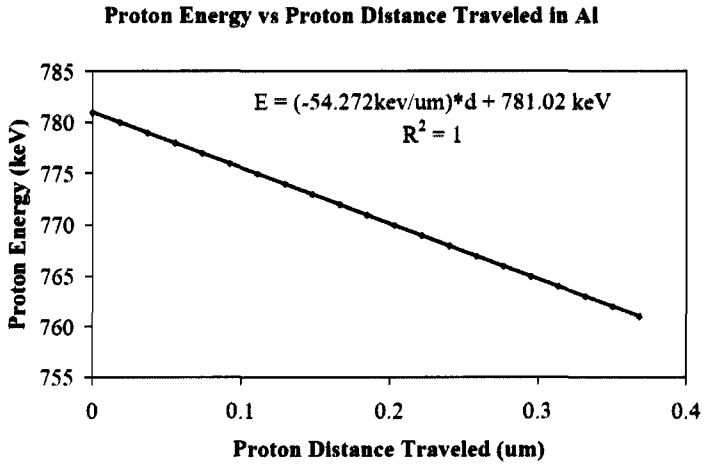

Figure 3.2: Proton Energy vs Proton Distance in Aluminum between $761keV$ and $781keV$

Clearly, we end up with a strong linear relationship. Using the fitted linear equation, we can derive relationship between energy loss and corresponding thickness of Al target. This is simply given by the equation:

$$\Delta d = \frac{\Delta E}{54.272keV/\mu m} \tag{3.3}$$

Where ΔE represent a proton energy loss and Δd is corresponding Al thickness. For example, a beam of protons in this energy range will loose $21.7keV$, after it passes through $0.4\mu m$ thick Al target. According to Meyer [57], the closest resonance above $771keV$ is located at $882keV$. Evidently, this is more than $100keV$ away from the resonance of interest and surely, there would be no interference in a $0.4\mu m$ thick Al target. As far as lower energy resonances are concerned, we will mention $764keV$ resonance ($12.325MeV$ population) and $757keV$ resonance ($12.318MeV$ population) [57]. These resonances are close enough to $771keV$, so they would undoubtedly be scanned by the proton beam. However, according to Harrisopulos et al. [56], their resonance strengths are $0.2eV$ and $0.14eV$, respectively, while the resonance strength of a $771keV$ res-

onance is $0.4eV$. Also, according to Meyer at al. [57], the branching ratios of these two resonances to the ground state are 0.06% and 1.5%, respectively. These numbers indicate clearly that there would be no $12.3MeV$ gamma rays coming from the $764keV$ and $757keV$ resonances. Hence, the $771keV$ resonance is quite well isolated. Before experiments were performed, the energy calibration of the KN machine had to be established, since we have seen that proton energy loss in the present target is $21.7keV$. Hence if a machine calibration was off by this number, or more which is only 2.8% of $771keV$, the resonance of interest could have been missed. A short experimental set is described in the following section.

3.1 Proton Energy Calibration of the KN Accelerator at $771keV$

An exact KN energy calibration had to be performed in order to tune the position of the $771keV$ resonance, accurately, i.e. to check for possible upward or downward energy shifts of the KN machine. For that purpose, a short experiment was performed. The idea was to start the accelerator at approximately $770keV$. The proton energy was then gradually increased until a gamma yield plateau was reached and finally passed. Here we were looking at $12.33MeV$ gamma yield together with its single and double escape peaks. For this particular experiment the HPGe detector was used, as close as possible to the Al proton target, with no shield present, the multichannel analyzer (MCA) was set to a maximum of $16k$ channels, since the gamma energy spectrum was spread beyond $12MeV$. The nominal proton current was at its maximum of

$55\mu A$. During the course of the experiment, 14 runs (in three days) were taken, ranging from $770keV$, up to $825keV$. The duration of each run was $45min$ real time. The HPGe compiled spectra for all runs are shown below in figure 3.3.

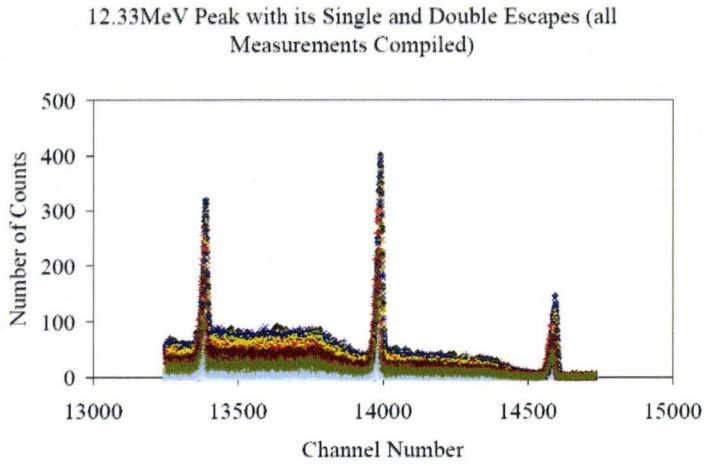

Figure 3.3: 12.33MeV Peak with its Single and Double Escapes

Amplifier gain was very stable since no gain shift was observed during the course of the measurements. This is evident from the compiled spectral data. The high energy peaks are located on very low background and therefore a simple cumulative integration was applied for better statistics. In other words, a sum of the primary peak along with its single and double escapes was applied and that was taken as representative of a total count. Again, this could be done, since we were dealing with extremely high energy, isolated gamma ray. Finally, the result of these runs as a function of proton energy is given in the figure 3.4.

The existence of a stable plateau between $795keV$ and $815keV$ is evident, thus our energy of interest, $771keV$, sits somewhere between these numbers ($805keV$, for reference). Therefore, at $805keV$ the KN machine is down-shifted

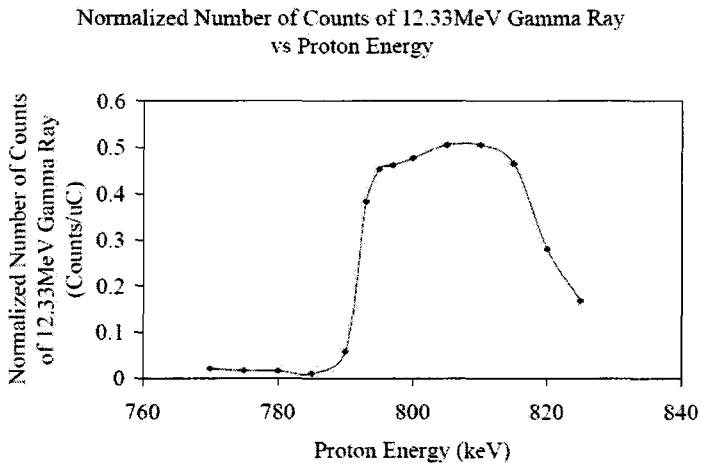

Figure 3.4: KN Accelerator Energy Calibration at $771keV$

in energy by more than $30keV$. In the experiments to follow, we will see that the energy was varied between these numbers in order to achieve the most stable and the largest proton current possible.

3.2 Nuclear Resonance Absorption Experiments Using HPGe Detector

This section describes a nuclear resonance experiments performed with the $12.33MeV$ gamma ray, using a HPGe detector for spectra collection. The glass absorber length was $14cm$ in order to match the length of the absorber in experiments described by Smith and Endt [10]. The width of an absorber was $4mm$. The distance between shielded detector and Al target was minimized to approximately $30cm$. The experimental arrangement is given in chapter 4, section 4.5, figure 4.33. Since we knew that the Doppler angle for $12.33MeV$ gamma rays occurred at 71° [10], the idea of these experiments was simply to perform measurements around this angle and to observe if it was possible

to see the dip-like nuclear resonance absorption feature centered at the angle of interest and finally to compare it with literature results. In particular, the experiments that Smith and Endt [10] performed in their study. They obtained a 21% nuclear resonance absorption (transmission) curve, centered at 71.1°. This is depicted in figure 1.14 and discussed in chapter 1. They also managed to have the full width at half maximum of approximately 0.8°. This implies standard deviation of 0.34°. As mentioned, in our experiments similar methods were applied. The glass and no glass runs were performed, with each measurement of $1h$ real time. In total, 14 data sets in 3 days were collected. The angular range covered was from 73° down to 67° in decrements of 1°. The nominal accelerator current was at maximum of approximately $55\mu A$, with the KN proton energy fixed at $800keV$, to compensate for the energy shift observed in the previous section. A normalization was done using a total proton time integrated current on the target in μC, which was very stable during the course of measurements. The results of this run are given below in figures 3.5, 3.6 and 3.7.

The first two figures 3.5 and 3.6 represent glass and no glass runs, while figure 3.7 represents a simple ratio (glass/no glass). Using the *Origin Pro* 7 fitting tool, a normalized Gaussian curve on a constant background (level value) was used for a fitting. This is given in equation 3.4.

$$Y = -\frac{AREA}{WIDTH \times \sqrt{2\pi}} \exp(-\frac{(x - POSITION)^2}{2 \times WIDTH^2}) + LEVEL \qquad (3.4)$$

Furthermore, the Gaussian amplitude is simply: $\frac{AREA}{WIDTH \times \sqrt{2\pi}}$, while maximum transmission (MAX T) is AMPLITUDE divided by LEVEL value. Note that the WIDTH value actually represents 1 standard deviation of the curve. There

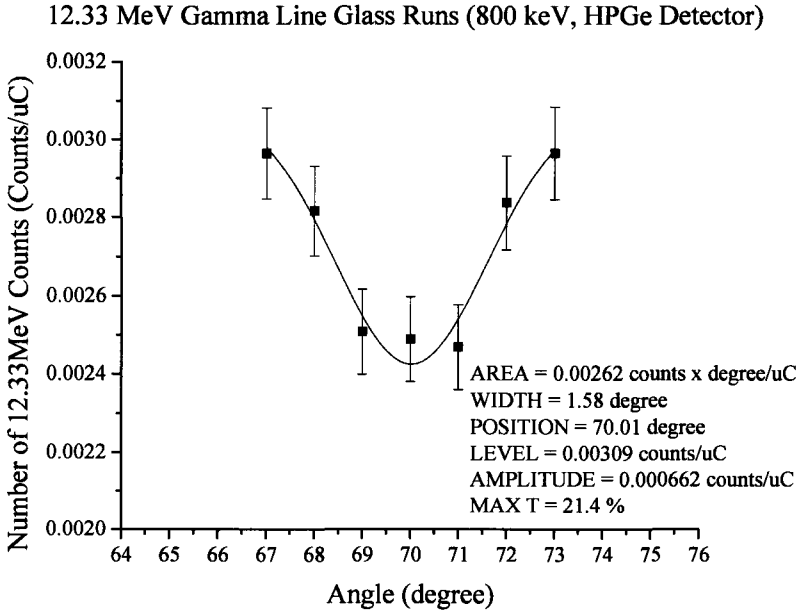

Figure 3.5: HPGe Glass Runs $12.33MeV$ Gamma Line; $800keV$ protons

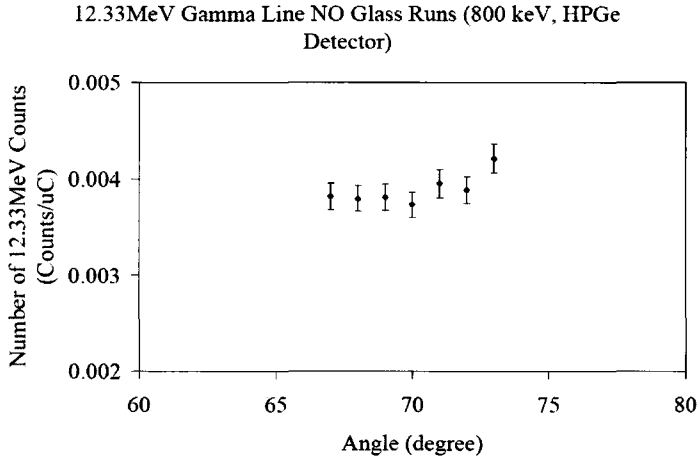

Figure 3.6: HPGe No Glass Runs $12.33MeV$ Gamma Line; $800keV$ protons

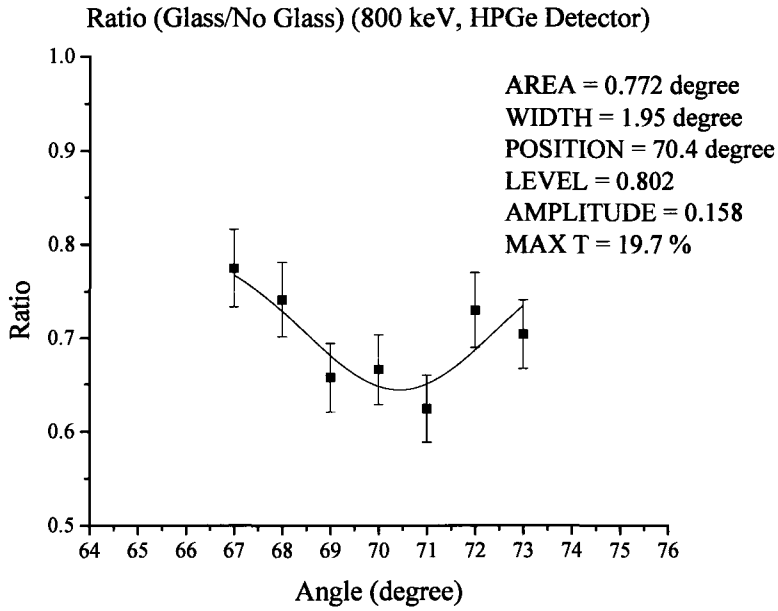

Figure 3.7: HPGe Ratio Glass / No Glass; $800keV$ protons

is an obvious dip centered at approximately 70°, with a maximum transmission value of approximately 20%, according to the fit. This is valid both for glass run and ratio run, although there is a small discrepancy in standard deviations. This is probably due to the fact that **no glass** results are not perfectly constant, which is evident from figure 3.6. Smith and Endt reported max T of 21%, which is in very close agreement with our value. Furthermore, from figure 1.14, the standard deviation for Smith and Endth curve is 0.34°. However, the standard deviation in our case is significantly larger and it is 1.58°. This is due to a slightly different geometry and collimator opening ($4mm$ in our case, compared to $1.9mm$ in Smith's case). Also, a much more sophisticated, laser based technique of angle determination was used by Smith, while in our case it was not used. Also, in our case, the dip is centered at 70°, instead of 71°. Furthermore, after this experimental set, a similar one was performed in order

to observe if we were able to reproduce the results. In this case, only glass runs were performed. The nominal proton energy was decreased to $795keV$, with maximum current output of $59\mu A$. The angular range covered was from 73° down to 67° in decrements of 1°. As usual, the real time collection was $1h$. The results are depicted below in figure 3.8.

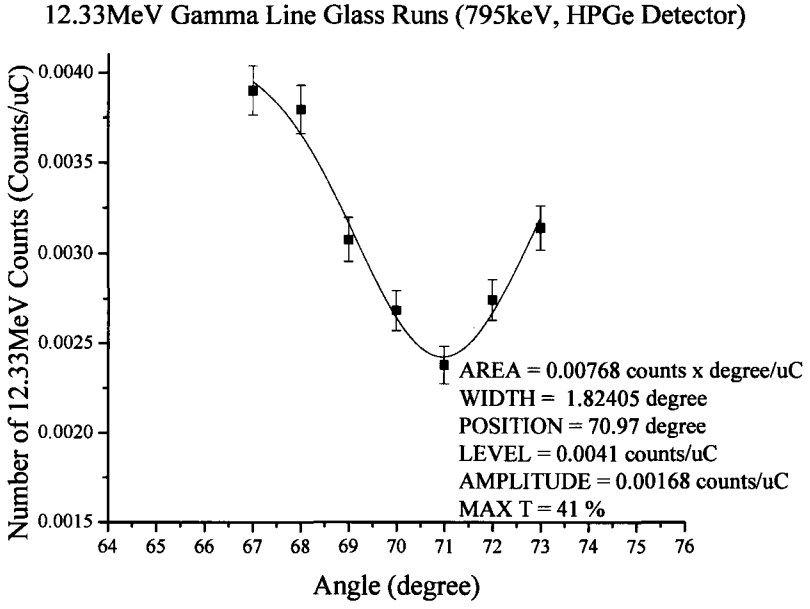

Figure 3.8: HPGe Glass Runs $12.33MeV$ Gamma Line; $795keV$ protons

The results obtained in this run are very similar to the results obtained in previous set. Again, the dip is clearly present. This time it is centered at 71°. However, the Gaussian fit yielded 41% for maximum transmission. We cannot rely on this value, since the first two point on the graph are probably outliers. Furthermore, perhaps fluctuations in proton beam energy were possible, since we were on the border of the plateau with $795keV$. Nevertheless, in total the results are very promising in terms of our experimental ability to produce and actually quantify the feature of nuclear resonance absorption, using the

$12.33MeV$ high energy gamma ray. Because of that, the experiments were repeated again. This time, instead of HPGe detector, a large NaI detector was used for collection in order to achieve better statistics. These experiments are described in the following section.

3.3 Nuclear Resonance Absorption Experiments Using Large NaI Detector

As suggested, this part describes experiments performed using large NaI detector for spectra collection. The experimental set up was the same as in previous section, except for the different detector and heavier shielding to compensate for the size of NaI scintillator. The maximum proton current was set at $59\mu A$ with proton energy slightly increased to $805keV$, in order to avoid possible uncertainties due to proton energy fluctuations. From figure 3.4, it is obvious that proton energy of $805keV$ sits in the middle of a plateau and apparently it provides slightly higher gamma yield compared to $795keV$ and $800keV$. Therefore, using this proton energy, the gamma yield was further increased. The angular range covered was from 73.5° down to 67°. In this case the angle decrement was decreased to 0.5°. In total 14 glass runs were taken. The duration of each one was $1h$ real time, as usual. Before the experiments were started, several high count rate runs were taken in order to calibrate the detector and to observe the resolution of the scintillator at $12.33MeV$. It was noted before in chapter 2 that the NaI detector could not fully resolve $12.33MeV$ peak from its single and double escapes. After energy calibration

at high count rate, we could clearly see those three features together and not fully resolved. It is depicted below in figures 3.10 and 3.9.

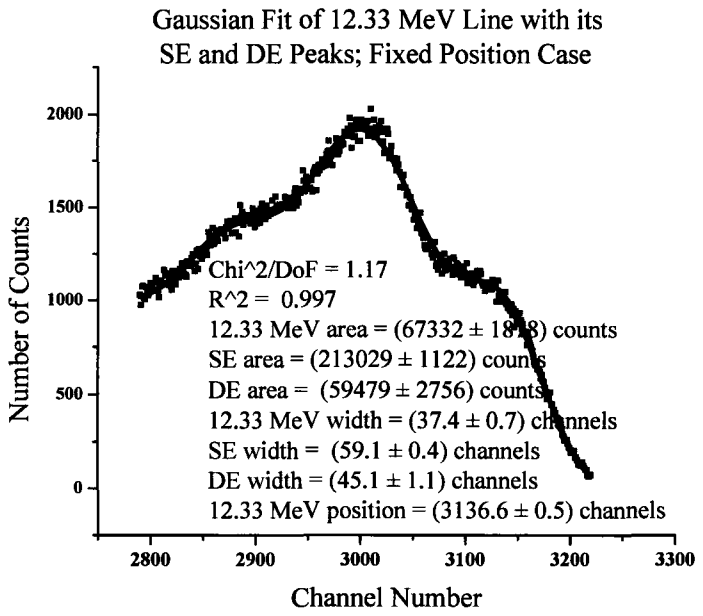

Figure 3.9: Large NaI Detector: Gaussian Fit; Fixed Position

Obviously, three positive Gaussian peaks were fitted together, with a linear function with a negative slope as a background. The single Gaussian equation is similar to the one cited before in the chapter; equation 3.4. In this case, we had three positive Gaussian peaks with different background and 9 parameters in total. In the first fit; figure 3.9, the width (resolution) of the peaks was varied with fixed $12.33MeV$ peak position, representing a reference peak position. In the second fit; figure 3.10, the positions of all peaks were varied with fixed, common resolution for all three peaks. When comparing these fits, the difference in the sum counts for all three peaks was less than 2%, i.e. the total number of counts for the fixed width case was $333.9kcounts$, while the fixed position case yielded $339.8kcounts$. The reason for doing this

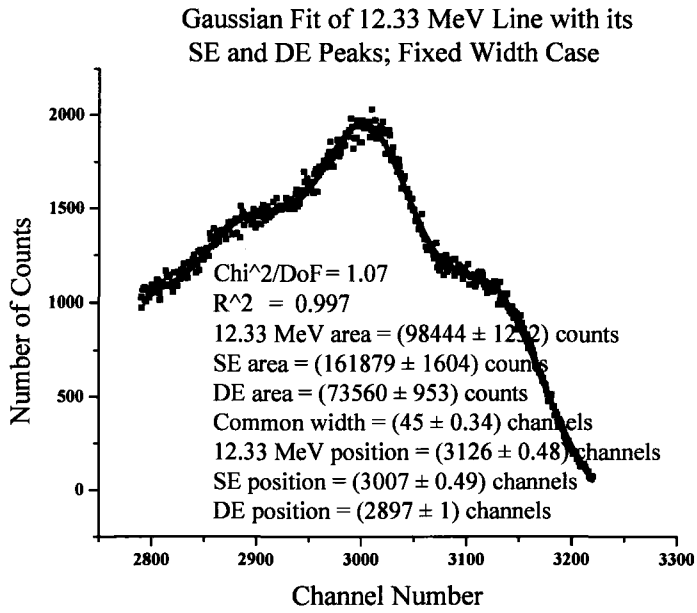

Figure 3.10: Large NaI Detector: Gaussian Fit; Fixed Width

kind of fitting for high count rate case was simply to identify the range of the total count integration for low count rate case that is observed in the actual experiments. Finally it was found that the optimal range of count integration was from channel number 2780 to channel number 3330. This fact was used in the final experimental analysis. Providing that the amplifier gain is constant for the duration of experiments, this method works well for low count rate case. Figure 3.11 represents glass results obtained by NaI detector.

The resonance dip is shifted slightly backward, on the energy scale. The maximum nuclear resonance absorption of 19% is observed at 69.7° with 1 standard deviation of 0.57°. Evidently, this data set reported the results which are in very close agreement to the results obtained by Smith and Endt, in terms of maximum transmission and even standard deviation of a Gaussian

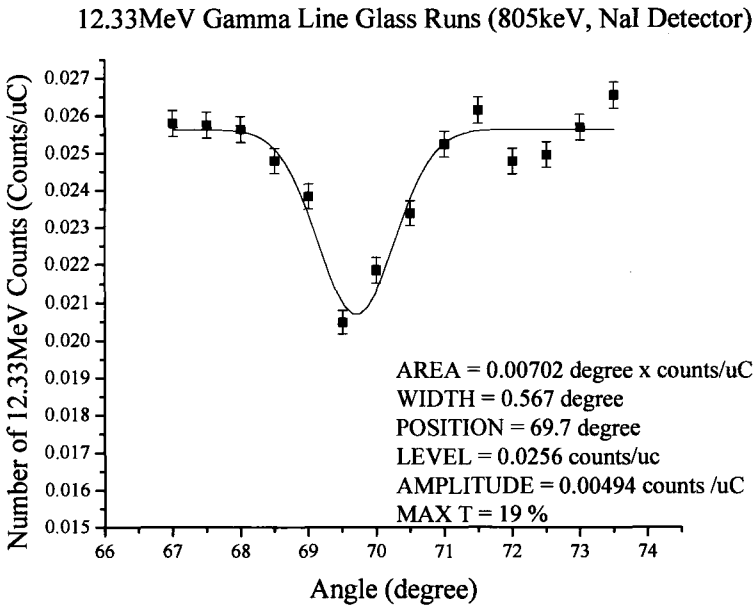

Figure 3.11: Large NaI Glass Runs 12.33MeV Gamma Line; 805keV protons

peak. Clearly, the resonance dip is present again and the third independent set of experiments confirmed this clearly. We can conclude that the present equipment is capable of obtaining the nuclear resonance absorption dip for Si metal for 12.33MeV transition, either by using HPGe detector or NaI scintillator.

Moreover, in the NaI case and observing the data from figure 3.11, at this stage we can estimate approximate conservative Si detection limit with the present system (KN Accelerator). The fitting program estimated the error of the area under Gaussian peak to be 0.00055$counts/\mu C$. From figure 3.11, the area was calculated to be: 0.00702$counts/\mu C$, or 12.8 sigma (where sigma is the Gaussian area uncertainty). Using the criterion that the signal must be at least two times its uncertainty, this implies the capability of the present

system to detect about 7 times less silicon than present in the glass filter (soda lime glass). According to discussion in section 1.3 the mass percentage of Si in soda lime glass is about 34%, so that present system is capable of detecting samples of 5% silicon by mass.

After these promising results with the KN accelerator, our next goal was to attempt similar experimental techniques, with the first excited state of ^{28}Si. This is the $1.78MeV$ transition, already discussed thoroughly throughout this work. In fact, the following chapter describes the work that represents an integral part of this thesis and consists of 7 different experimental sets. This would undoubtedly be a pilot work in nuclear resonance gamma transmission experiments.

Chapter 4

Nuclear Resonance Absorption Experiments Using the First Excited State of Si Nucleus ($1.78MeV$ Gamma Line)

4.1 Theoretical Predictions and Reasons for Using $1.78MeV$ Silicon State

As mentioned before and looking back at the literature [10] [57] the strongest Si resonance that gives direct transition to the ground state is populated by $771keV$ protons. This is $12.33MeV$ resonance. However, as seen in preliminary experiments and discussed in previous chapters, the use of this resonance and corresponding gamma line has its own limitations. The phenomenon of nuclear resonance fluorescence and absorption is seen in a medium with relatively high concentration of Si (soda lime glass). Our next goal would be to look for a resonance that would possible give promising results in medium with

lower Si concentration. Especially, this becomes important when thick glass absorbers are used together with heavily shielded detectors, which are indeed conditions required for these experiments to take place. Since the $12.33MeV$ resonance is the strongest one amongst all resonances that directly de-excite to the ground state [10] [56] [58], the logical implication is that we could not use other, weaker ground state transitions. At that point, a ground state transition was ruled out as our primary means for detecting Si. Therefore, encouraged by findings so far and theoretical predictions, we were looking for other solutions to this problem. The concept itself did not change, i.e. to base this new solution on the NRA/NRF sequence and Doppler angle corrections, with slight modifications of the experimental site. Moreover, we know that the most prominent gamma line in the spectrum is $1.78MeV$, the first excited state of silicon. In addition, according to the literature it was found that almost all resonances de-excite to this state, either by single transition, or in cascade [57]. After taking all these facts into consideration, we have decided to use $1.78MeV$ line as our primary gamma source.

Therefore, by using thick pure Al target and maximum proton energy of about $2.3MeV$, we would be able to sweep through all possible resonances (down to zero proton energy), and to obtain maximum possible yield of this gamma line. This is somewhat similar to experiments conducted in chapter 2. However, in this case, $1.78MeV$, presumably isotropic photon fluence would be corrected for Doppler angle. The problem with this approach is the fact that there are no theoretical calculations (predictions) of how to use Doppler angle correction for an intermediate excited state. Nevertheless, as far as this is concerned, we can base our predictions on already established theoretical

calculations and experimental findings together with some logical assumptions. A more detailed discussion will be given later in this section, after we introduce relevant theory needed for establishing a valid set of logical assumptions.

The idea was rather to explore (scan) experimentally a complete angular range; from 90° down to 0° and this way to determine an approximate value for Doppler angle. It is important to keep in mind the fact that we have some assumptions where the Doppler angle might be, but these will be explained later. Of course, several repetitive or similar experiments would have to be conducted in order to confirm a validity of a Doppler angle, or an angular position of maximum NRA. Evidently, this kind of approach would definitely be a pilot project, since no literature studied this feature. Once an appropriate Doppler angle for intermediate $1.78MeV$ silicon state (first excited state) is found, the quantification of silicon could take place. Just to avoid any confusion, the Doppler angle is still an angle between incoming protons and a position of a primary detector, used for detection of $1.78MeV$ gamma rays. Obviously, the Doppler angle correction works well for a short-lived resonance that de-excites completely to the silicon ground state [10] [88] [89]. This feature was discussed in the previous chapters thoroughly. As seen before, in order for Doppler angle correction to work, we need to have a short lived transition. In fact, the half life of a transition has to be much shorter compared to a time of flight of a moving nucleus (a nucleus that carries the momentum of incoming proton). Indeed, it has to be shorter or at least comparable to the time before nucleus starts to slow down significantly, since relatively constant velocity has to be preserved in order for the theory of Doppler shift to work. In our case a stationary Si nucleus receives all the momentum from a

captured proton and starts to move in the same direction. Of course, when it starts to move, it becomes an ordinary heavy charged particle moving in the Al absorber, continuously slowing down (CSDA approximation). While moving in the absorber material, a nucleus emits $1.78MeV$ gamma rays. Initially, in order to check the feasibility of future experiments based on detection of the $1.78MeV$ line and the described intermediate transitions in the Si nucleus, we will perform some simple calculations and compare our findings with the literature; and with the $12.33MeV$ resonance direct transition to the ground state, which was proven to work [10] and confirmed in this work. The half life of the $1.78MeV$ intermediate state is relatively long; $475fs$ [32], compared to half life of the $12.33MeV$ Si resonance; $0.045fs$ [10]. The $12.33MeV$ resonance is populated by $771keV$ protons, while the majority of $1.78MeV$ gamma rays come from $12.54MeV$ resonance, that is populated by $992keV$ protons [56]. Later in this chapter we will see and experimentally prove that contribution of $12.54MeV$ to the total fluence of $1.78MeV$ gamma rays is approximately 60%. In other words, when using a thick Al target and proton energy of approximately $2.3MeV$, so that all possible resonances (more than 85 of them) are included into the total gamma yield, a single $12.54MeV$ resonance contributes 60% of this total fluence. The rest of the fluence comes from the other resonances. Using the simple equation 1.42 from chapter 1, we can easily calculate that the initial kinetic energy of flying Si nuclei, populated by $771keV$ and $992keV$ protons are $27.76keV$ and $35.72keV$, respectively. Hence corresponding velocities are $0.00146c$ and $0.00166c$, respectively. Let's start as simple as possible and consider a charged particle with mass m, (in atomic mass units

m_A) and initial kinetic energy E in an absorber (in our case; Si nucleus in Al absorber). Simply, the initial velocity is given by:

$$v = \sqrt{\frac{2E}{m}} = c\sqrt{\frac{2E}{mc^2}} = (3 \times 10^8 \frac{m}{s})\sqrt{\frac{2E}{m_A(931MeV/amu)}} \tag{4.1}$$

We can assume an average velocity of a particle as it slows down to be [91]:

$$\langle v \rangle = Kv \tag{4.2}$$

Where K is proportionality constant. In a case of uniform acceleration, K would be 0.5, so that average velocity is half of a initial velocity. However, the rate of energy loss (stopping power) for charged particles is greater as they slow down, i.e. near the end of their tracks. In other words, deceleration is not constant. Therefore, K must be higher than 0.5, between 0.6 and 0.8, as a rule of thumb. Later in this section, we will calculate the K value for our particular case. Moreover, the time required for a charged particle to stop (in this case, time of flight of Si recoiled nucleus) is given by [91]:

$$T = \frac{R}{\langle v \rangle} \tag{4.3}$$

Where R represents a range of a charged particle in a given material. In our case, we deal with low energy, heavy charged particle ($30keV$ Si nucleus) in Al absorber. In general, stopping power of a charged particle is described by the Bethe equation [92]:

$$S(E) = -\frac{dE}{dx} = \frac{4\pi z^2}{m_e v^2}(\frac{e^2}{4\pi\varepsilon_0})^2 NZln(\frac{2m_e v^2}{I}) \tag{4.4}$$

Obviously, the above equation gives stopping power as a function of a velocity (v) of a charge particle in an absorber, z and Z, respectively, represent an

atomic number of a charged particle and absorber, m_e is electron mass, N represents electron density of absorber, while I is mean excitation potential. This quantity is experimentally defined and particularly, for Al, its value is $167eV$ [93]. In addition, this form of stopping power Bethe equation ignores relativistic velocities, which are indeed irrelevant for our study. From the kinetic energy and speed relationship, where M is the mass of the charged particle, we simply have:

$$v^2 = \frac{2E}{M} \tag{4.5}$$

Now, substituting equation 4.5 into equation 4.4, we end up with stopping power as a function of a kinetic energy of a charged particle:

$$S(E) = -\frac{dE}{dx} = \frac{2\pi z^2 NZ}{E}\frac{M}{m_e}(\frac{e^2}{4\pi\varepsilon_0})^2 ln(\frac{4m_e E}{MI}) \tag{4.6}$$

Substituting all relevant constants we end up with equation:

$$S(E) = -\frac{dE}{dx} = \frac{1.02 \times 10^8 keV^2/\mu m}{E} ln(4.70 \times 10^{-4} keV^{-1} E) \tag{4.7}$$

Evidently, energy of a charged particle is given in units of keV. Similarly, we can write Bethe equation for **alpha particle** in Al absorber, for comparison purposes:

$$S(E) = -\frac{dE}{dx} = \frac{2.98 \times 10^5 keV^2/\mu m}{E} ln(3.28 \times 10^{-3} keV^{-1} E) \tag{4.8}$$

From equations above, we can see that Bethe approach cannot be taken as valid model for stopping power for low energy particles. This is obvious from logarithmic part of the equations. For relatively low energies, logarithmic part would give negative result for stopping power. Physically, this is not a valid result. In our case, we are dealing with Si nucleus of approximately $30keV$,

which is way below energy range for validity of Bethe equation. Even, for an alpha particle that carries the same initial kinetic energy, the Bethe theory would not be valid. As a matter of fact, in his article [94] Ziegler stated that the Bethe stopping power equation is valid for kinetic energies of approximately $1MeV/amu$ and above. Hence in the case of Si nucleus, Bethe theory would be valid for projectile with kinetic energy of above $27MeV$, while for the alpha particle, this energy would be above $4MeV$. Because of that, in order to estimate (find) a stopping power and range for low energy Si nucleus in Al absorber, we used SRIM (The Stopping Power and Range of Ions in Matter) software [95], developed by J.F. Ziegler. Furthermore, for comparison purposes, we used compiled data from Johannes Kepler University, Linz, Austria [15]. H. Paul [15] compiled experimental data for heavy, low energy ions stopping in different media, among which we found Si ions stopping in Al absorber. This is pictured in the graph in figure 4.1.

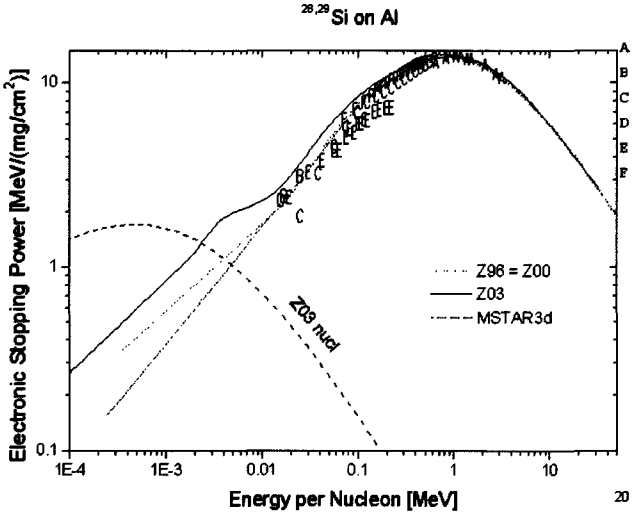

Figure 4.1: Compiled Stopping Power Data for Si in Al [15]

Evidently, from graph (figure 4.1), experimental data for Si stopping in Al exist to as low as $0.8v_0$ [96], where v_0 represents Bohr velocity. This is velocity of electron orbiting hydrogen nucleus [97]:

$$v_0 = \frac{c}{137} = 0.0073c \tag{4.9}$$

Recall that initial velocity of $35.72keV$ Si nucleus is $0.00166c$. Hence with this maximum velocity we are out of the experimental range and we must rely on SRIM theoretical calculations for stopping power. The graph in figure 4.2 shows SRIM output for Si stopping power. Evidently, it is almost identical to the one given by H.Paul.

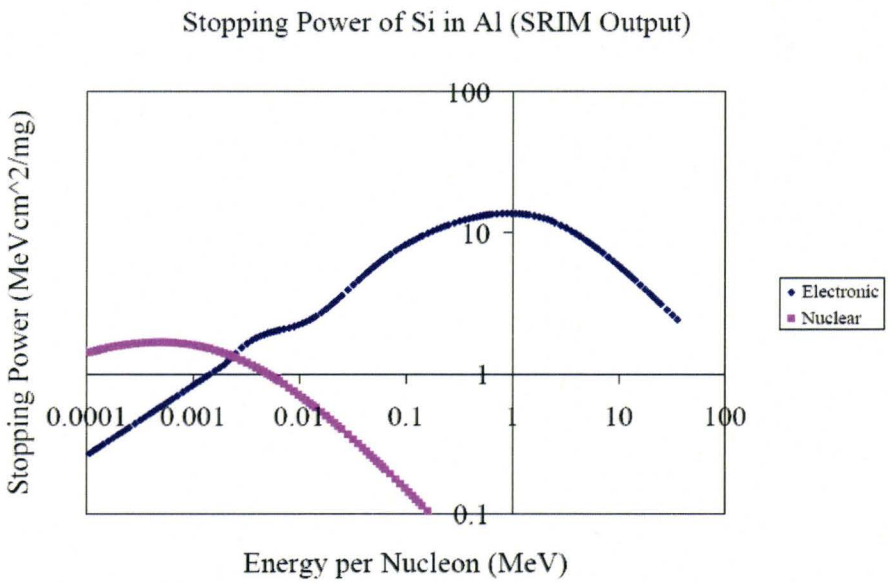

Figure 4.2: Stopping Power of Si in Al according to SRIM

Our range of interest is from zero to $35.72keV$ and that is pictured in the figure 4.3. Starting with stopping power graph in figure 4.3, equation 3.2 and knowing the initial conditions; i.e. $E(0) = 35.72keV$, we can easily construct

discrete function $E(x)$ and hence $v(x)$. Thus, at the end velocity function is given in figure 4.4:

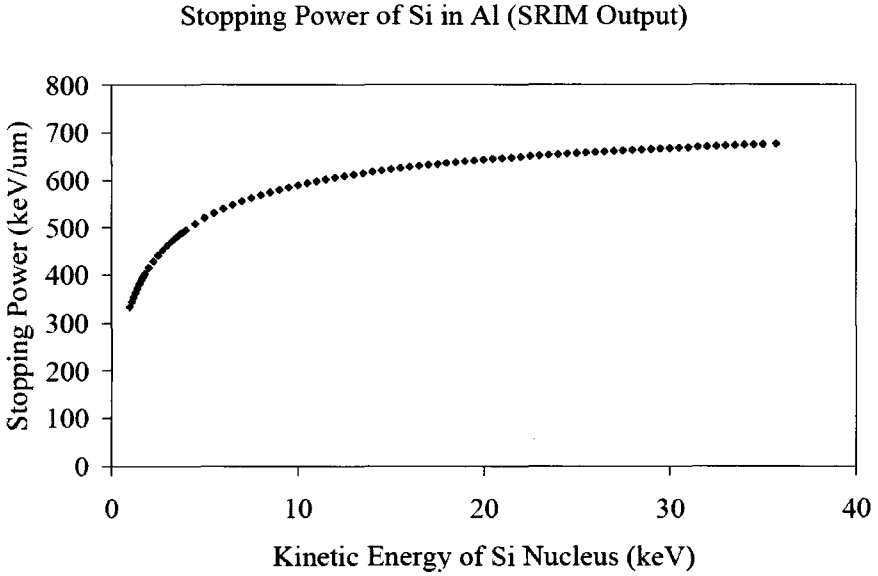

Figure 4.3: Stopping Power of Si in Al according to SRIM up to $36keV$

Note that distance is given in angstroms. Finally, from this graph, we can extract an average velocity of a Si nucleus. This is given by simple integration:

$$f_{avg} = \frac{1}{b-a}\int_a^b f(x)dx \tag{4.10}$$

Where a and b are limits of integration. In our case, those are $0A$ and $594.5A$, respectively. Hence, using trapezoid rule for numerical integration, we end up with an average velocity of Si nucleus to be $3.177 \times 10^5 m/s$, which further corresponds to K value (see equation 4.3) of 0.64. Also, we will mention here that SRIM program gives a projected range of $447A$, while this calculation, evidently, yields range of $594.5A$. In the calculations to follow, we will use lower (SRIM) number as our range, since it will give the "worst case approximation". At this point, we are ready to compare two mentioned transitions; $12.33MeV$

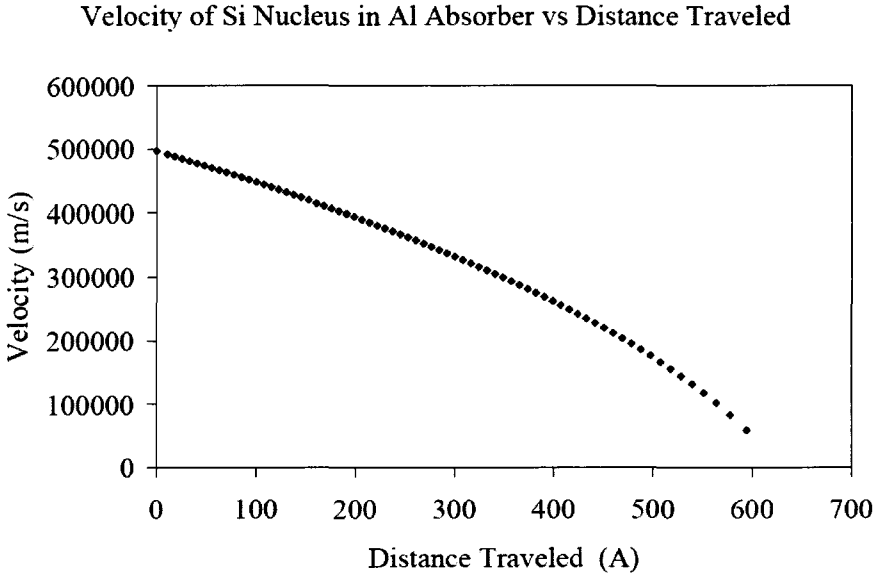

Figure 4.4: Velocity of $35.72keV$ Si Nucleus in Al Absorber

resonance direct de-excitation to the ground state [10] and $1.78MeV$ transition to the ground state that is populated mostly by $12.54MeV$ resonance. Previously in this chapter it was mentioned that this resonance makes approximately 60% of total $1.78MeV$ gamma fluence. All parameters relevant for this comparison calculation are given in table 4.1.

Using data from the table, we will compare the number of resonantly attenuated gamma rays in each case. Of course these are empirical and relative values, both normalized to the $12.33MeV$ case, which corresponds to unity (see table). For the purpose of our particular case, we will call this value "Final Comparison" (FC). It is given by the following equation:

$$FC = DF \times RS \times GY \times \#Si \times frac \times PC \tag{4.11}$$

The parameters in equation 4.11 are defined as:

Table 4.1: Empirical Comparison of $12.33MeV$ and $1.78MeV$ Transitions

Nuclear Properties	$E_p = 771keV$	$E_p = 992keV$
Si nucleus initial kinetic energy in Al target	27.76 keV	35.72 keV
Si nucleus range in Al target	356 A [95]	447 A [95]
$*$ Si nucleus time of flight in Al target	127.1 fs	140.3 fs
Transition half-life	0.045 fs [10]	475 fs [32]
Decayed fraction (**DF**)	1	0.185
Resonance strength (**RS**)	0.42 eV [56]	2 eV [56]
Gamma yield (**GY**)	75% [57]	75% [57]
# of Si atoms in absorber ($\times 10^{23} cm^{-2}$) (**#Si**)	3 [10]	$1.4 - 3.8$
Si absorber thickness	$14cm$ [10]	$7.5cm - 20cm$
Si absorber effective thickness	$7cm$ [10]	$3.75cm - 10cm$
Si absorber density	$1.003g/cm^3$ [10]	$2.53g/cm^3$ [63]
Si absorber mass att. coeff.	$0.0239cm^2/g$ [98]	$0.0473cm^2/g$ [98]
Si absorber linear att. coeff.	$0.02397cm^{-1}$ [10]	$0.11967cm^{-1}$
Fraction of gamma rays passed through (**frac**)	0.835	$0.302 - 0.658$
Proton Current (**PC**)	$30\mu A$ [10]	$30\mu A$-$60\mu A$
Final Comparison (**FC**) $7.5cm$	1	$0.324 - 0.648$
Final Comparison (**FC**) $20cm$	1	$0.403 - 0.807$

- DF - Corresponds to the fraction of decayed nuclei during the nuclear movement (before stopping time elapsed)

- RS - Represents resonance strength in eV proposed by Harrisopulos et al. [56]

- GY - Theoretical Gamma Yield proposed by Meyer et al. [57]

- $\#Si$ - Number of Si atoms in an absorber per cm^2

- $frac$ - Fraction of survived gamma rays that passed through an absorber

- PC - Proton Current

- FC - Empirical number that represents the product of all of the above

The parameters in the above equation are completely independent contributors to the fluence rate of the gamma rays of interest. To clarify the case further, looking at equation 4.11 and table 4.1, Si nucleus time of flight was calculated using equation 4.3 and K value of 0.64. Also the Decayed fraction value was calculated using the exponential decay equation and appropriate half-lives, given in the above table. Evidently, decayed fraction for $12.33MeV$ case is 1 since the half life of the transition is almost 3000 times shorter than the flight time of the Si nucleus, in $1.78MeV$ case. Moreover, the atomic density of Si atoms in a soda lime glass was calculated to be $1.878 \times 10^{22} atoms/cm^3$ out of the total atomic density $7.382 \times 10^{22} atoms/cm^3$, given in chapter 1. Hence, the former number was used to calculate the number of Si atoms per cm^2 for absorber thicknesses of $7.5cm$ and $20cm$. These numbers were used since they represent the lengths of an absorbers used in the experiments conducted in this thesis and described later in the chapter. Smith and Endt [10], managed to insert $3.01 \times 10^{23} atoms/cm^2$ of Si powder into the $14cm$ long, $0.19cm$ wide and $7cm$ high lead collimator. From these numbers it was calculated that Si density for this particular case was $1.003 g/cm^3$. Therefore, by knowing densities and mass attenuation coefficients, the linear attenuation coefficients were easily calculated. Finally, the fraction of gamma rays, passed through the absorber itself, was calculated using the exponential decay attenuation formula and effective Si absorber thickness, This value corresponds to the half of an actual absorber thickness. The Final Comparison Results for $1.78MeV$ experimental case vary from 32% to 81% compared to reference $12.33MeV$ case, depending on the proton current available and thickness of soda lime glass absorber (below referenced as "glass absorber"). In particular, by varying

proton currents from $30\mu A$ to $60\mu A$, and for glass thickness of $7.5cm$, the relative number of resonantly attenuated gamma rays varies from 32% to 65%, while for glass thickness of $20cm$ it varies from 40% to 81%. It is very important to keep in mind that the calculations above represent a single resonance, which corresponds to thin target experiments. If we are to use a thick target, and hence all possible resonances, the ratio would be improved by 1.67 times in the favor of $1.78MeV$ case. To conclude, from our preliminary calculations, based on theory and some assumptions, it is logical and very likely that usage of thick (and even thin) Al target and $1.78MeV$ gamma rays will lead toward valuable results. This means that we should be able to observe the phenomenon of nuclear resonance absorption and fluorescence with the $1.78MeV$ transition. The question is raised at this stage: What is the lowest concentration of Si that can be detected using $1.78MeV$ line? Hopefully, this could be answered in experiments to follow. Moreover, in order to wrap up the discussion fully, we are going to speculate on the possible Doppler angle position between 90° and 0°. As mentioned before, we do not have exact theoretical calculation how to predict this angle for an intermediate transition. However, with some assumptions, we can make use of theory derived and explained in chapter 1. We will recall the Doppler angle correction equation 1.44:

$$cos\alpha = \frac{E_0}{Mvc} = \frac{E_0}{\sqrt{2M_pE_pc^2}} \tag{4.12}$$

In the first part of this equation, $E_0 = 1.78MeV$, M is the mass of Si nucleus and v is its speed. The speed of Si moving nucleus (until complete stop) is calculated and given in figure 4.4. Evidently, we are not dealing with constant velocity here, therefore we will assume that the position of the Doppler angle

Table 4.2: Doppler Angle for $1.78MeV$ Transition

Kinetic Energy (keV)	Velocity $\times 10^5 m/s$	Doppler Angle (α)
35.72	4.97	87.64
32.5	4.74	87.52
29.5	4.51	87.40
26.5	4.28	87.26
23.5	4.03	87.09
20.5	3.76	86.88
17.5	3.48	86.62
14.5	3.16	86.29
11.5	2.82	85.83
9	2.49	85.29
6	2.04	84.23
3	1.44	81.82
1	0.83	75.74

will actually be spread across several values and the maximum value would be somewhere in between. Substituting these velocities into equation 4.12, we end up with an angular range from 87.64° down to 75.7°. The values are given in table 4.2. The simple calculation gave us an initial idea of the position of Doppler angle, however, the real position could be shifted further down, due to the existence of preceding high energy gamma ray, $10.76MeV$ (transition from $12.54MeV$ to $1.78MeV$). Anyhow, the actual Doppler angle position will be determined experimentally, if possible, in the sections to follow.

4.2 Experimental Set 1: Aluminum Filter vs Glass Filter

As mentioned, the idea behind this approach was to set up the experimental site similar to the one described by Smith and Endt in their studies [10] [88]. This is pictured in figure 4.5. However, instead of a NaI detector, we

used a HPGe n type Canberra detector, described earlier. Also, the absorber width in our case was $2mm$ and the distance between detector face and proton target was approximately $47cm$. The length of an absorber was $20cm$. Two types of absorbers were used; soda lime glass and Al. The reason for using Al absorber was the fact that it poses a similar attenuation coefficient to the glass absorber. Hence it is an appropriate material for comparison purposes. According to the X-COM Photon Cross Section Database [98], the linear attenuation coefficient at gamma energy of $1.78MeV$ for the glass absorber and aluminum metal is $0.119669cm^{-1}$ and $0.12366cm^{-1}$, respectively, which corresponds to the attenuation difference of less than 5%. Hence, for the same photon fluence of $1.78MeV$ gamma rays and for $20cm$ long absorbers, the ratio of linear attenuation of glass / Al is approximately 1.

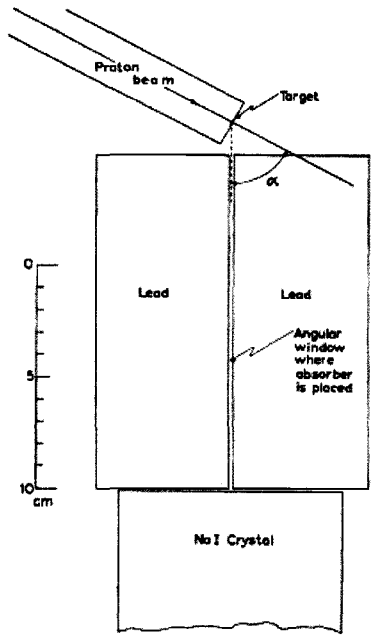

Figure 4.5: Experimental Setup According to Smith Article [10]

For this project, a special rotating table was designed. The construction was intended to be very robust so it could withstand a large amounts of heavy lead and concrete shielding, together with detectors and other equipment. The midpoint of the table was fixed to the ground right below the midpoint of the Al accelerator target, so that the table (together with all equipment) could rotate freely around the target. The rotating table allowed us to cover angles from 90° down to 0° in increments of as low as half of a degree. Together with rotation, the table had another two degrees of freedom; i.e. it could move up and down, as well as towards and away from the proton target. The very first set of runs took 5 working days to complete. The main idea of this preliminary set was to test the equipment and sensitivity, as well as to see if it is possible roughly to find the position of Doppler angle. The glass absorber was used, the nominal proton current varied from $55\mu A$ to $60\mu A$, depending on conditions of KN accelerator. Proton energy was fixed at $1000keV$. For this geometry, we were able to run from 84° down to 37° in steps of 1°. The thick pure Al proton target was used (99.999% purity). The idea was to hit the $12.54MeV$ resonance that is populated by $992keV$ protons (and of course all the resonances below, down to zero proton energy). The collection time for every angle was $30min$ real time. The gamma count normalization was performed using the total charge collected onto the Al target in units of μC. Also, the number of counts was corrected for the detector dead time, as well, although it was very low, less than 1.5%. The experiments yielded relatively poor statistics and a low count rate for the $1.78MeV$ gamma line of maximum 170 gross counts per $1800s$. The results are given below in figure 4.6.

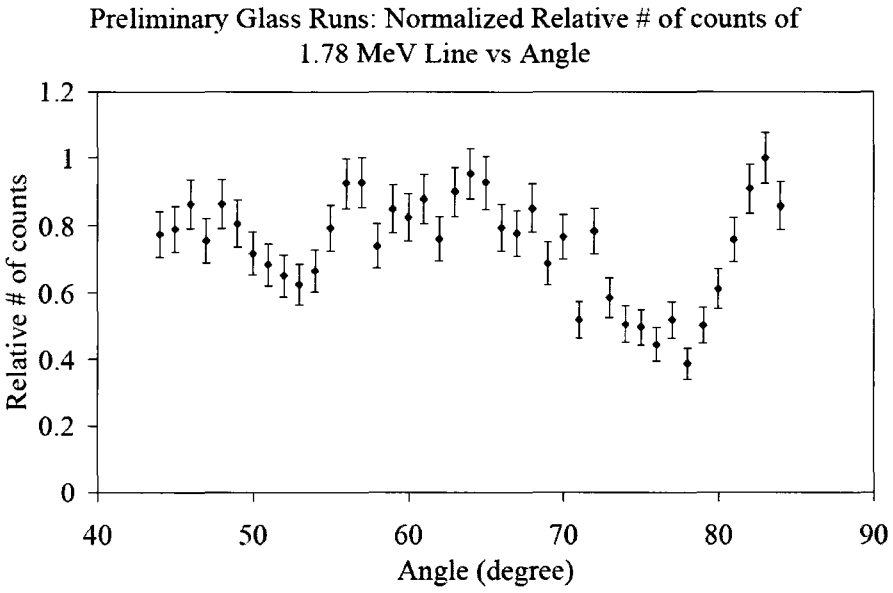

Figure 4.6: Experimental Set 1a: Preliminary glass Runs

To avoid confusion, this figure represents number of counts when the glass absorber was used only. Also, the data set was normalized to the proton current, firstly, and then to the highest count rate, so that this value reads maximum of 1. Figure 4.6 reveals evident dip at the angle of 79°, with FWHM of approximately 8°. This was a promising finding since from our previous discussion, we expected a similar feature in that angular range. Unfortunately, these results were inconclusive at the moment, for several reasons. Firstly, there is a similar, smaller feature at approximately 53°, secondly, the count statistics were relatively poor. Finally, after the complete experimental set was finished, it was realized that nominal proton energy was very close to the strongest resonance observed. In other words, the proton energy was fixed at $1000keV$, while the strongest resonance was observed at $992keV$. Therefore, even the smallest proton energy fluctuations would have caused the resonance

of interest to be missed and consequently the false results would have been obtained. For these reasons, a second experimental set was designed. The idea here was to use identical glass and Al absorbers and to compare the results in terms of the ratio, as mentioned previously. In both cases, the angular range varied from 84° down to 40° in decrements of 2°. The angular step was increased from 1° to 2° in order to reduce the experimental time by half. The complete experimental set took 7 KN accelerator operating days. The proton current varied between $55\mu A$ and $60\mu A$, as in the previous set, while proton energy was fixed at $1.2MeV$. This way, we have avoided the possibility of missing the desired resonance with small proton energy fluctuations. The detecting equipment was the same as in the previous set and the collection for every single angle took $30min$ of detector's real time. The glass and Al absorber net count results are given in figures 4.7 and 4.8.

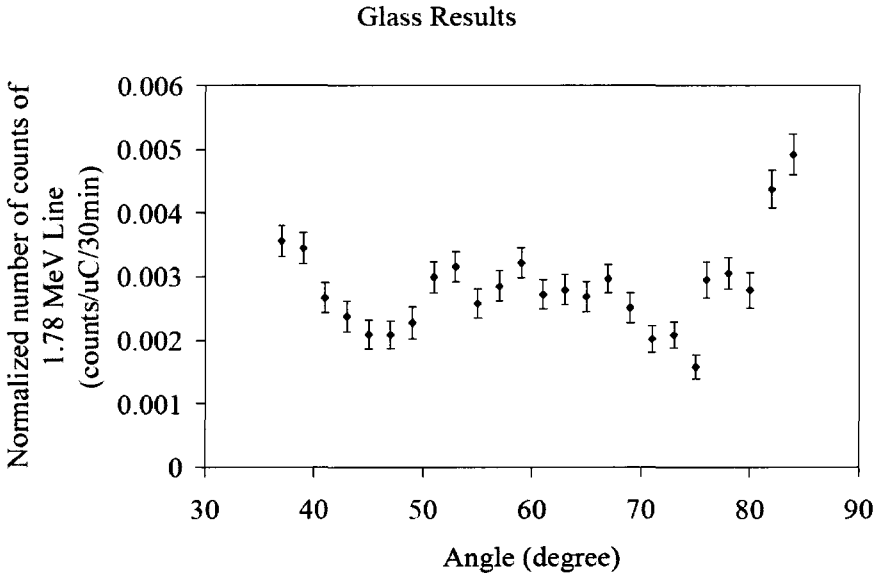

Figure 4.7: Experimental Set 1b: Preliminary glass Runs

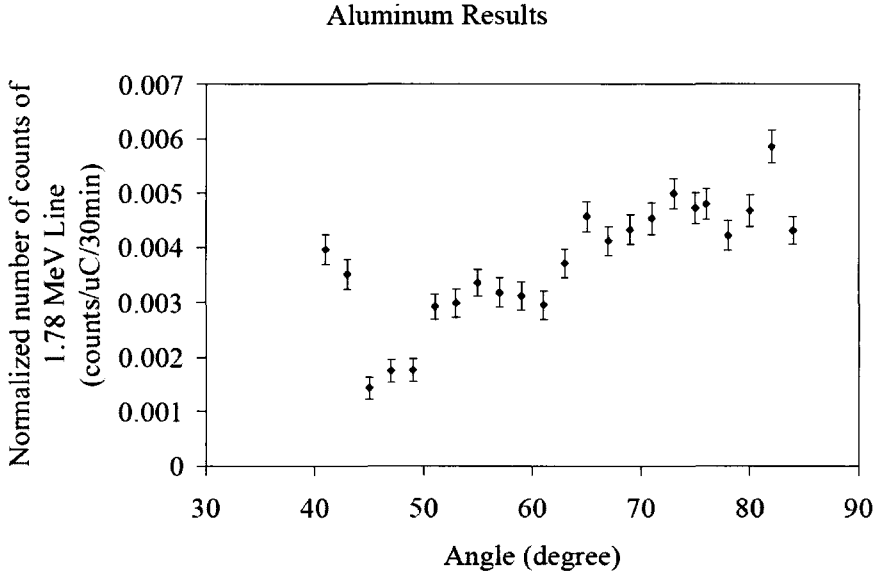

Figure 4.8: Experimental Set 1b: Preliminary Al Runs

Clearly, the glass runs reveal very similar features as in the previous experiment, which is indeed an encouraging fact. In the case of Al runs, there is a relatively steady increment of the net counts as a function of the angle, without the observable dips as in glass runs. The absence of dips in Al runs is actually a very promising fact. However, a confusing thing was a clear non-uniformity of the number of counts. Originally, we were expecting relatively isotropic distribution of the $1.78MeV$ gamma rays, however, this poses a question with regards to a possible existence of an angular distribution of these gamma rays. This feature will become more apparent later in the chapter. Also the normalized ratio, given in figure 4.9 shows a clear dip between 76° and 77°. The ratio fluctuates around 1, with relatively high error bars (mostly due to the poor counting statistics), except in the region where dip is observed, where it drops down to 0.3. Looking at results so far, we are still unable to draw a positive conclusion regarding the position of an observed dip. Furthermore,

we are even unable to confidently conclude about the existence of the feature itself. Mainly, this is due to poor counting statistics. Similarly, the existence of two dips and the non isotropic distribution of $1.78MeV$ gamma rays in Al case further complicate the case. Taking into the account these findings, a new experimental set was designed in order greatly to enhance the counting statistics and see how this will affect the final results.

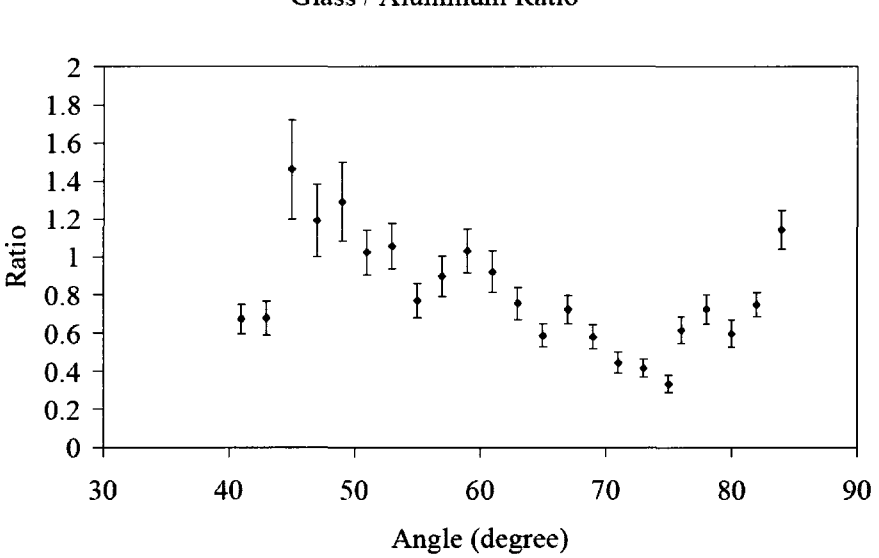

Figure 4.9: Experimental Set 1b: Ratio Glass / Al

4.3 Experimental Set 2: Wide Glass Filter Measurements with NaI Detector

After relatively promising and to some degree non-conclusive results from previous set of experiments, we decided to modify our experimental arrangement and to try to locate and maximize the feature of nuclear resonance absorption. The thick Al target was used, as usual. However, this time a

large NaI detector (6" by 6") was used as a primary detector for collection of $1.78MeV$ gamma rays, while a FIXED $LaBr_3(Ce)$ Canberra scintillator (LaBr elsewhere in the text) was used to monitor incident photon fluence as one of the means of normalization. The convenience of LaBr scintillator was its size and mobility. This is a small and very light crystal, integrated with all electronics and high voltage supply into an Al tube and connected to a computer via single USB cable. The performance of this detector in terms of counting efficiency and resolution is somewhere between HPGe and NaI detectors. The glass collimator opening was widened up to $2.5cm$ with a total length of $7.5cm$. This was done in order to maximize the photon count rate in the NaI detector and to shorten the collection time. Furthermore, presumably, the widening experimental width of the aperture should not wash out the nuclear resonance feature that we are looking for, since it was seen in the previous section that the FWHM of the possible dip observed was relatively large. Figure 4.10 represents a simplified version of the experimental setting. Also, note that in this figure the LaBr detector is not included, since it was fixed at one place (different plane) and its position was not changed during the course of measurements, as indicated.

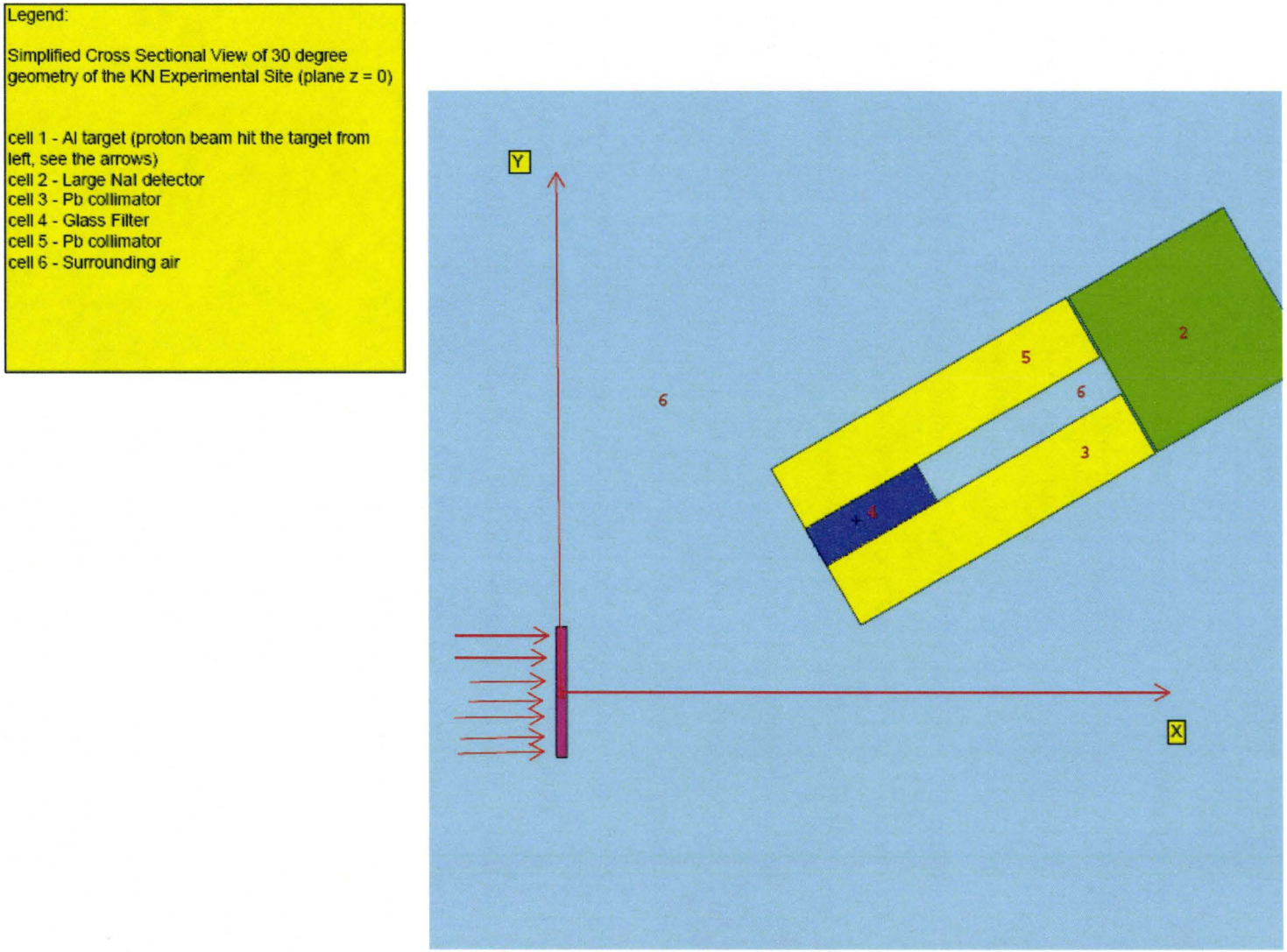

Figure 4.10: Experimental Setup: Wide Glass Collimator and Large NaI Detector

Since a larger FWHM was observed previously, the angular step was increased to 3°. Hence, we collected 21 measurements scanning a total angular range; from 90° down to 30° with the glass collimator present and the same number of measurements without the glass collimator present. In this case, instead of Al we had an empty collimator (air only). The glass and no glass runs were taken consecutively, i.e. 90° with glass filter after 90° without glass filter, etc. Glass filter measurements were collected for $20min$, while no glass filter measurements were collected for $10min$. The non glass collection times were shortened in order to save time, while good counting statistics was observed anyhow. Normalization was done in two ways. Firstly, by using total proton charge collected on the Al target (units of μC) with detector dead time corrections applied. Secondly, as mentioned above, using the fixed LaBr detector. In total, 42 NaI spectra were collected in 5 days of measurements, together with 42 LaBr spectra. Both detectors were calibrated once per day using a ^{60}Co source, in order ensure a constant amplifier gain. During the experiments, the maximum proton current on the target was approximately $20\mu A$ and the proton energy was fixed at $1.2MeV$, as before. This way, the strongest proton resonances that de-excite to the $1.78MeV$ level have been included [57]. The NaI spectra were collected using the Ortec Maestro program, while LaBr spectra were collected using the Canberra Genie program. Figure 4.11 represents the ordinary NaI spectrum obtained from each measurement.

Evidently, the $1.78MeV$ gamma line is clearly distinguishable on a log scale, as the second peak in figure 4.11, while the first peak is annihilation radiation at $511keV$. After all spectra were collected (82 in total), analysis was done using the *Origin Pro* 7 fitting tool, in a similar way to that described in

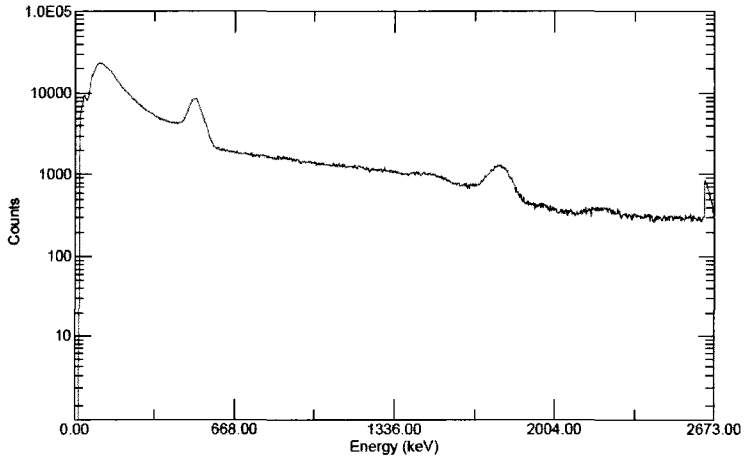

Figure 4.11: Gamma Spectrum from Thick Al Target

chapter 3. The $1.78MeV$ peak was isolated from the rest of the spectrum and a normalized Gaussian peak with linearly decreasing background was applied as a fitting function, for both detectors. This is shown in the equation 4.13

$$Y = \frac{A}{w\sqrt{2\pi}} \exp(-\frac{(x-\mu)^2}{2w^2}) - mx + B \tag{4.13}$$

In this equation A represents a total area of the $1.78MeV$ peak, w represents one standard deviation of the Gaussian distribution, μ is the peak position, B represents the spectrum background and finally, m is the slope of the linear portion of the spectrum. Of course, the total area of the peak was used as an absolute number of counts corresponding to the $1.78MeV$ gamma line, which was corrected for the detector dead time for every single measurement. An example of a NaI detector fit is given in figure 4.12.

From the fit, it is evident that a good function was applied, since we observed acceptable χ^2 and R^2 values, both close to 1. This was the case for both detectors. The idea of this experiment was to plot the normalized $1.78MeV$ peak area (count rate) against the corresponding angle, for both glass and no

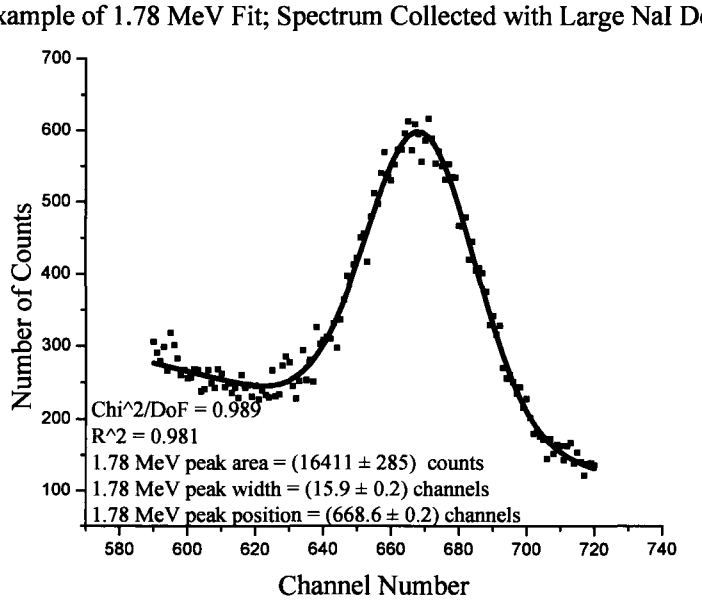

Figure 4.12: Origin Pro Fit of $1.78MeV$ Gamma Line

glass results and to obtain their profiles, from 90° down to 0°. Also, in order to look for the Doppler angle across the complete angular range, it is required to plot the ratio (glass / no glass) results to cancel out the ordinary linear attenuation of the gamma rays. Note that the same procedure was done in the previous section. In that case, the nuclear resonance attenuation dip should be clearly visible. The following simple attenuation calculation will approximate the attenuation of $1.78MeV$ gamma ray in $7.5cm$ of soda lime glass. Recall that $7.5cm$ is the thickness of the glass filter in this set of experiments. The photon intensity I is given by the simple exponential expression:

$$I = I_0 e^{-\mu t} \tag{4.14}$$

In equation 4.14, t is the thickness of material (soda lime glass), μ is the linear attenuation coefficient of the same material and I_0 is the initial photon

intensity. From table 4.1 the linear attenuation coefficient for soda lime glass at $1.78MeV$, was calculated to be $0.11967cm^{-1}$. Substituting these numbers into equation 4.14, we end up with $I = 0.4I_0$. Hence, we would expect ratio of approximately 0.4 when normalized glass results are divided by normalized no glass results. The outcome of these experiments is given below in terms of two sets of data. They both represent a relative number of counts of the $1.78MeV$ gamma line seen by the NaI scintillator, as a function of angle between incoming protons and detector position. However, they differ in terms of the normalization itself. The first set uses a normalization by total proton charge accumulated on the Al target, while the second set is normalization using the LaBr detector, as explained above. Charge collection normalization results are given in the first three figures: 4.13, 4.14 and 4.15, while LaBr normalization results are given in the following three figures: 4.16, 4.17 and 4.18.

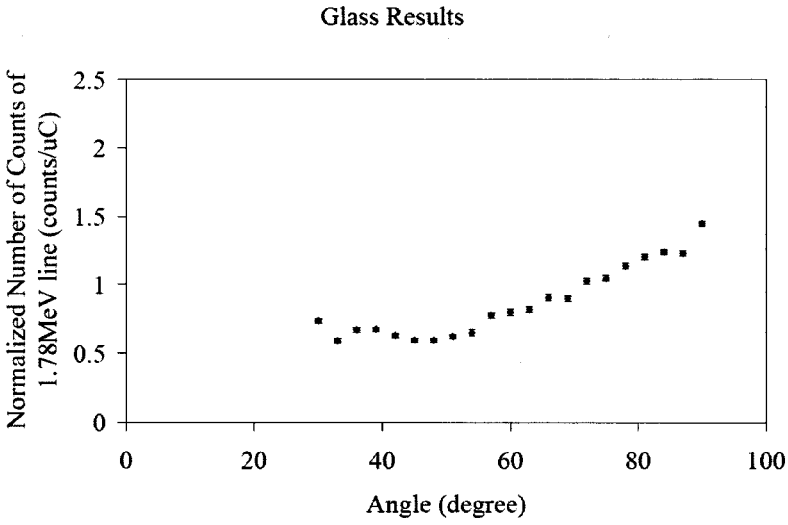

Figure 4.13: Experimental Set 2: Glass Results with Charge Normalization

Observing first two figures in either normalization sets: 4.13, 4.14, 4.16, 4.17, it is evident that V shape of angular distribution of $1.78MeV$ gamma

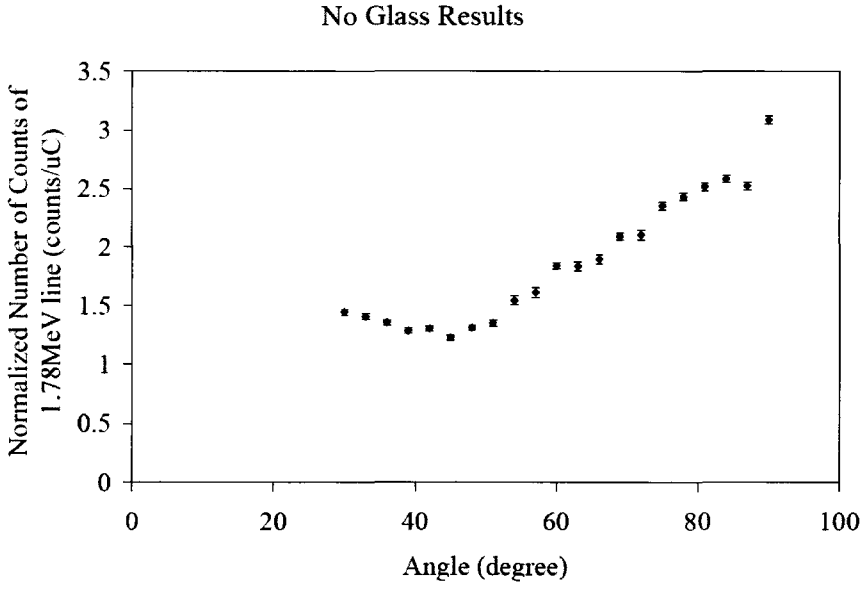

Figure 4.14: Experimental Set 2: No Glass Results with Charge Normalization

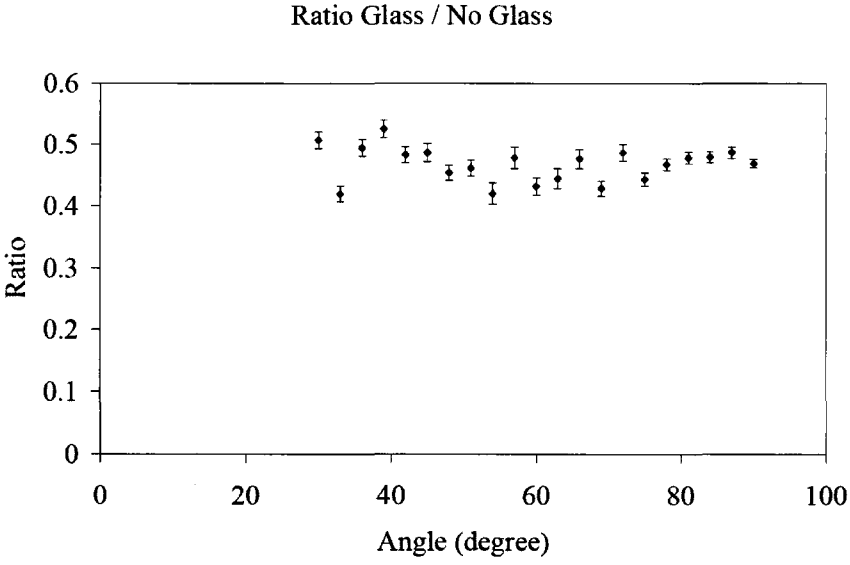

Figure 4.15: Experimental Set 2: Ratio with Charge Normalization

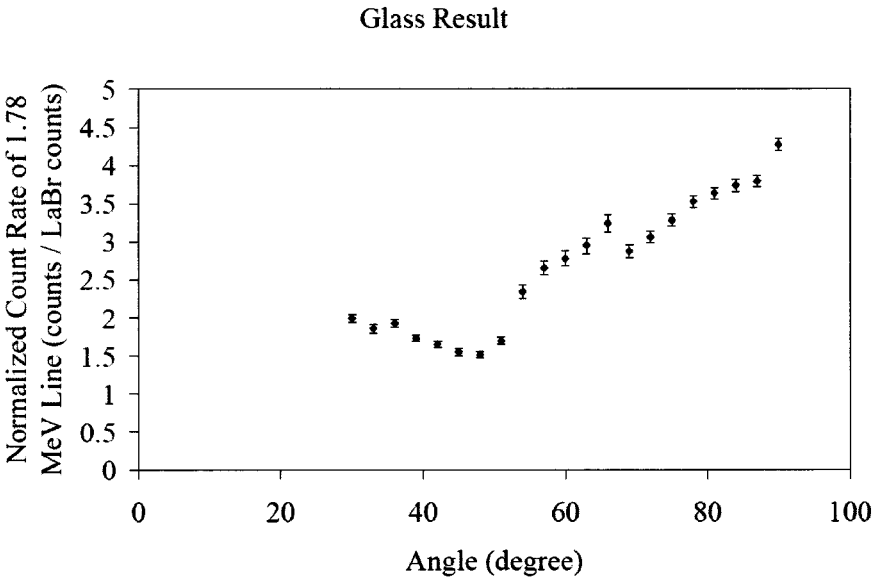

Figure 4.16: Experimental Set 2: Glass Results with LaBr Normalization

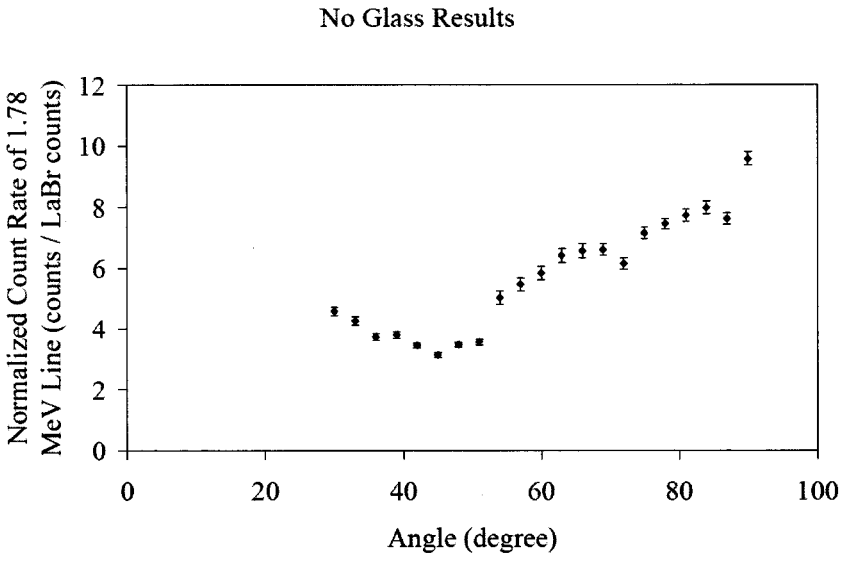

Figure 4.17: Experimental Set 2: No Glass Results with LaBr Normalization

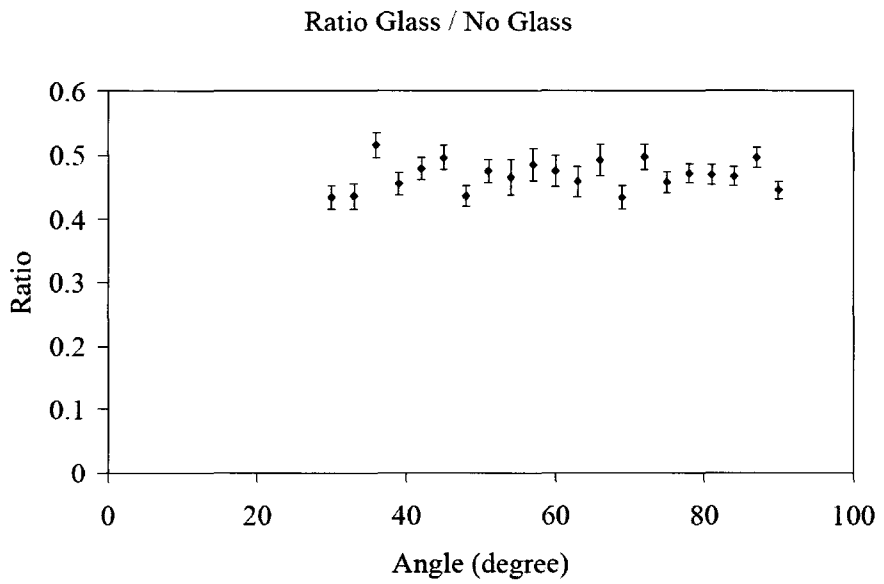

Figure 4.18: Experimental Set 2: Ratio with LaBr Normalization

rays is consistent, although more pronounced with the LaBr normalization compared to the integrated charge normalization. A similar pattern was observed in previous set of experiments with HPGe detector and Al present in collimator. The repetitive feature in our results confirms the validity of the procedure itself. Unfortunately, the origin of V shaped angular distribution of $1.78MeV$ gamma rays is not entirely known, however this is not of greatest concern at this moment. As mentioned, before all the experimental work started, the logical assumption was an existence of isotropic distribution of $1.78MeV$ gamma rays, which is obviously not the case here. On the other hand, the glass measurement did not yield a visible dip, as was the case in the previous section. They rather resemble the non glass measurements, with a V shaped profile. This outcome is the only inconsistency in our results so far. A promising fact was an evident consistency in all other features. Moreover, if we take a look at ratio graphs, we can see that photon intensity through the glass

absorber ranges between 0.4 and 0.5 which is in close agreement with the above calculation. A wide and shallow dip-like feature can be seen in the charge normalization ratio graph; figure 4.15, sitting between 45° and 75°, with absolute minimum at approximately 60°. This feature cannot be seen in the LaBr normalization case. Furthermore, this dip is not so apparent as the one seen in the previous set of experiments and it is even shifted down by 16°. Taking these facts into the account, we still cannot draw a positive conclusion regarding a location and/or even existence of nuclear resonance features. Therefore, further experimenting was required, with a rising suspicion that total proton current normalization was not reliable. In fact, the KN instruments kept giving us a very steady and constant current for significantly different gamma ray counts in the LaBr normalization detector. Also, a significant widening of a glass filter (from $2mm$ to $2.5cm$) and increment in the angle step (to 3°) might be one of the reasons for the nuclear resonance dip to disappear. Considering all these facts, a slightly different set of experiments was performed. It is described in the following section of this chapter. However, before we go further, it is important to emphasize here that this optimization is actually a trial and error procedure for finding a nuclear resonance dip. Furthermore, from the experimental experience, so far, we can conclude that complete data collection can spread throughout several days and even weeks, depending on angular range and number of data points collected. Keeping this in mind, we have to be very careful in terms of a steady condition of the KN machine and other experimental parameters, so we can merge and compare our results that are obtained during different days, with high confidence.

4.4 Experimental Set 3: Wide Glass Filter Measurements with HPGe Detector

The third set of experiments consisted of two relatively short and repetitive subsets. In fact, this was a repetition of the previous set, with a single exception. The HPGe detector was used for acquisition purposes, instead of the NaI detector. The reason for doing a repetition of the same experiment was to observe whether the latest experimental settings, with wide collimator and relatively large angular step, would yield, at least, reproducible results.

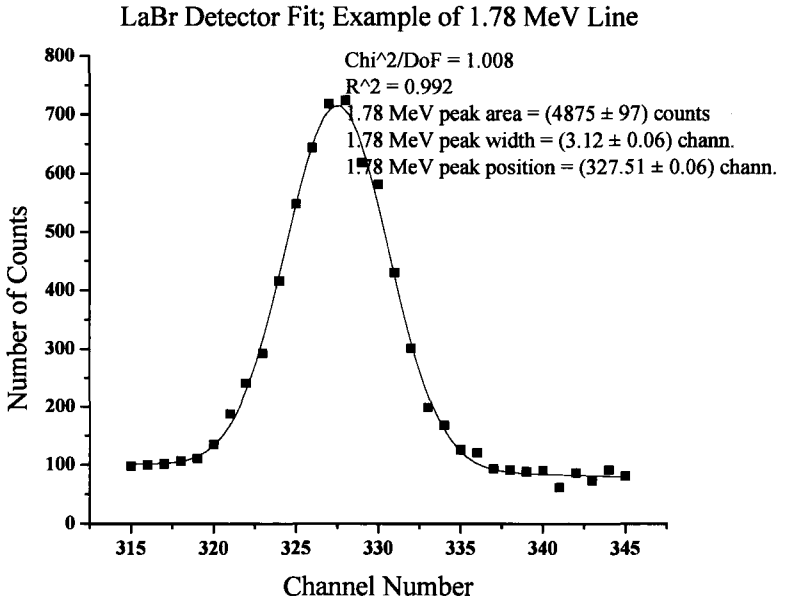

Figure 4.19: LaBr Detector Response Function Fit at $1.78MeV$ Peak

Furthermore, it was important to see if this kind of experimental setting was the right way to go towards the exploration of a nuclear resonance dip. As usual, a fixed LaBr detector was used for normalization, together with total proton charge accumulated on the target. An example of LaBr detector

response fitted function at $1.78MeV$ peak is given in figure 4.19. Obviously, a Gaussian peak was fitted together with linearly decreasing background. The same procedure was applied to all normalization spectra collected with this detector. In the case of the HPGe detector, no fitting was required, since $1.78MeV$ peak sits on a very low background. Hence, simple constant and linear background subtraction from gross count was applied. The first subset includes angular range from 90° down to 48°, while the repetition includes an angular range from 90° to 42°. The angular step in each case was 3°, with the same glass collimator as in previous experimental set; $2.5cm$ wide and $7.5cm$ long. The complete data collection took 6 KN accelerator working days. In both subsets, the glass runs took $20min$ of real time, while for no glass runs, it took $10min$ to collect a single spectrum. The nominal proton current in both cases was $30\mu A$. Finally, the proton energy was set to $1.2MeV$, as usual.

4.4.1 The First Experimental Subset; Angular Range from 90° down to 48°

The following 6 figures represent the results from the first experimental subset. The first three figures; 4.20 to 4.22 represent current normalization results, while the following three figures; 4.23 to 4.25 represent normalization with the fixed LaBr detector.

Evidently, very similar patterns in both glass and no glass runs are observed for each normalization. Unfortunately, there is not a significant dip-like pattern in ratio curves, figures 4.22 and 4.25. However, the encouraging fact is the stable glass/no glass ratio between 0.4 and 0.5, which is in accordance with

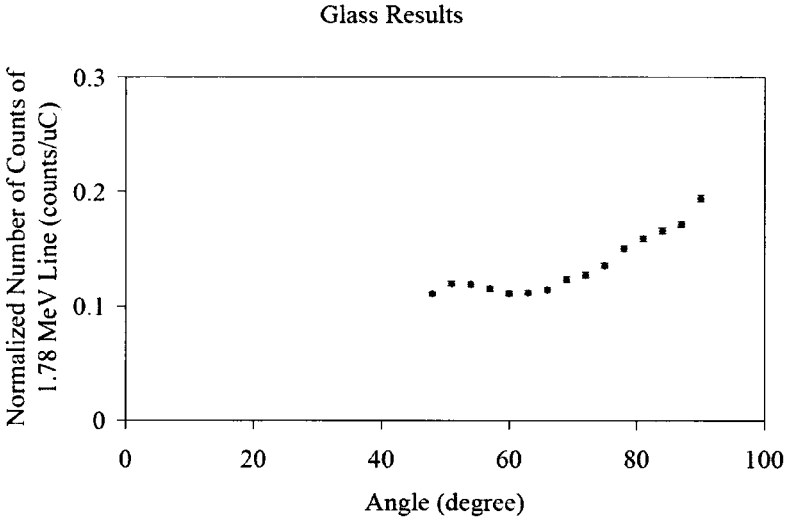

Figure 4.20: Experimental Set 3a: Glass Results with Charge Normalization

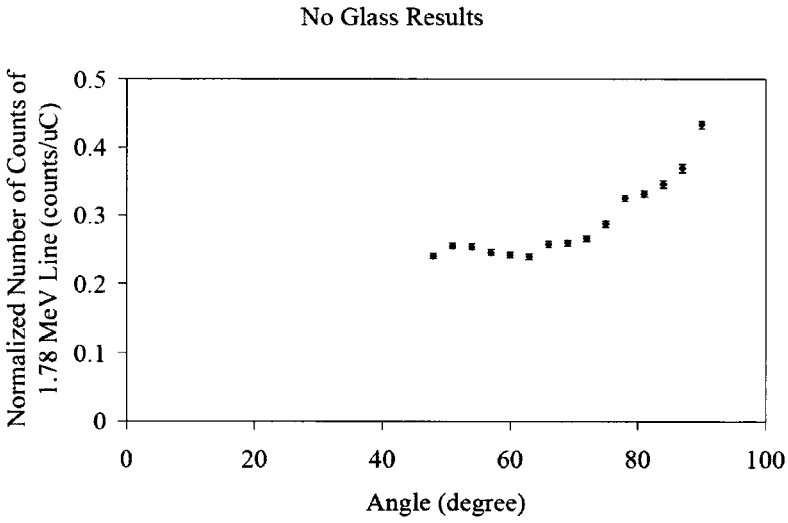

Figure 4.21: Experimental Set 3a: No Glass Results with Charge Normalization

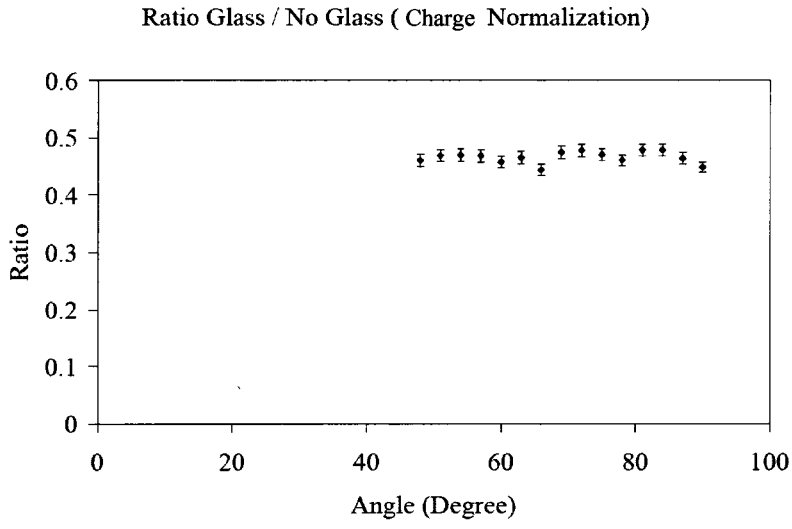

Figure 4.22: Experimental Set 3a: Ratio with Charge Normalization

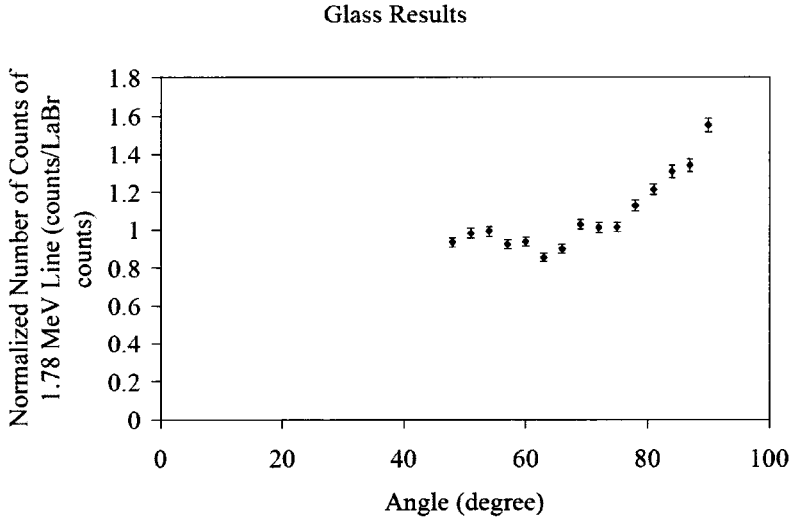

Figure 4.23: Experimental Set 3a: No Glass Results with LaBr Normalization

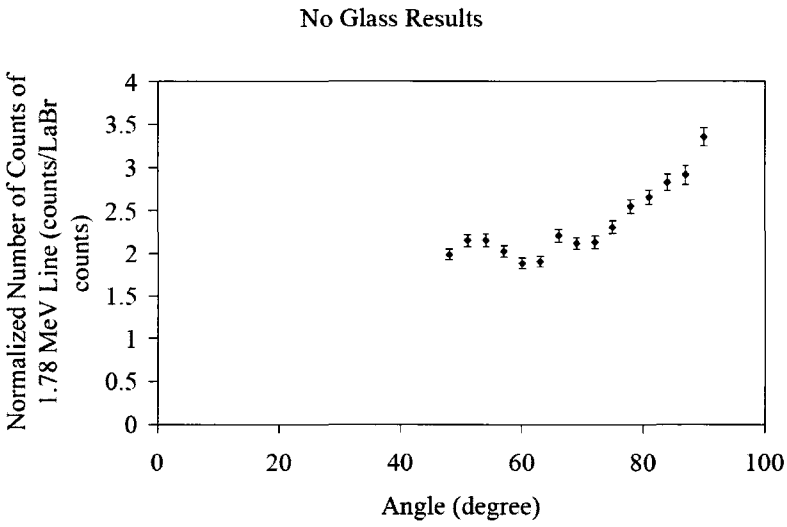

Figure 4.24: Experimental Set 3a: No Glass Results with LaBr Normalization

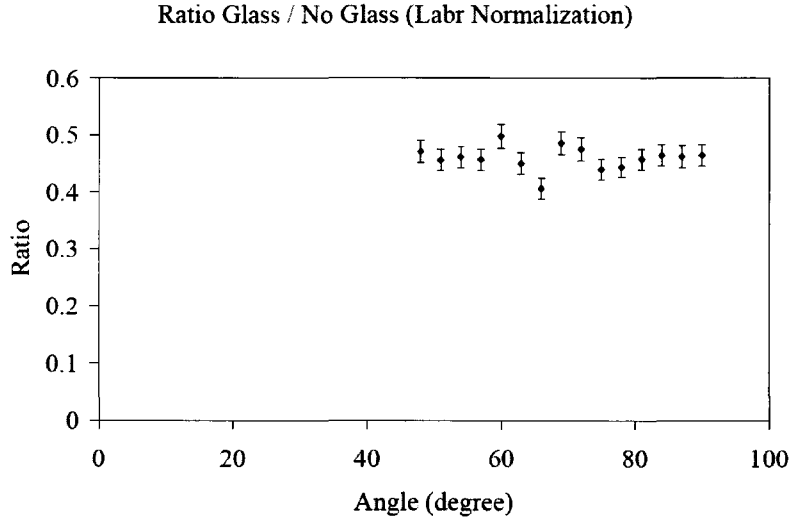

Figure 4.25: Experimental Set 3a: Ratio with LaBr Normalization

theoretical calculations and previous experiments. In particular, with the results presented in figures 4.15 and 4.18 from section 4.2 and obtained with the NaI detector This confirms the stability of the accelerator and precision of the experimental technique.

4.4.2 The Second Experimental Subset; Angular Range from 90° down to 42°

The following 6 figures represent the results from the second experimental subset. As in previous subset, the first three figures; 4.26 to 4.28 represent charge normalization results, while the following three figures; 4.29 to 4.31 represent normalization with the fixed LaBr detector.

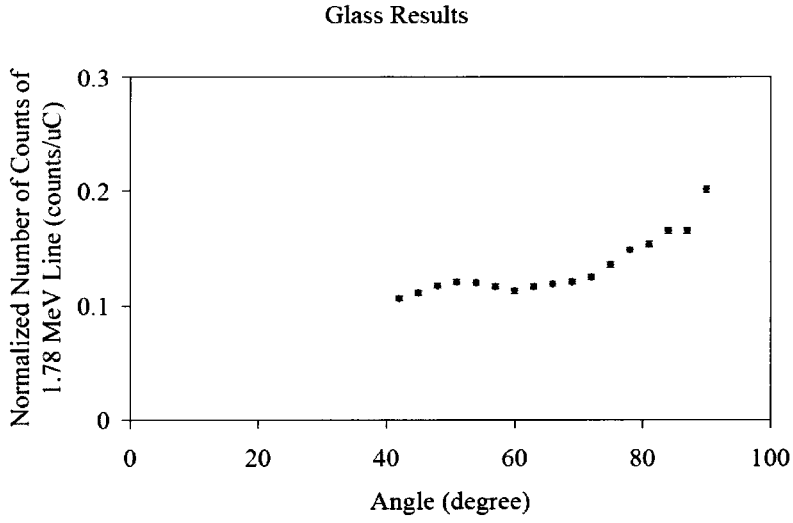

Figure 4.26: Experimental Set 3b: Glass Results with Charge Normalization

Similarly, as in the previous case the second subset shows no significant dip-like feature that could correspond to the presence of nuclear resonance. Also, the ratio between glass and no glass measurements varies between 0.4

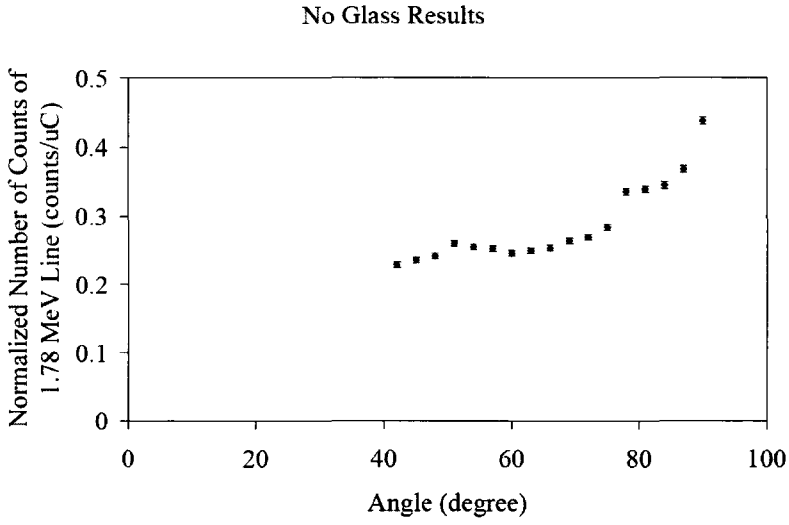

Figure 4.27: Experimental Set 3b: No Glass Results with Charge Normalization

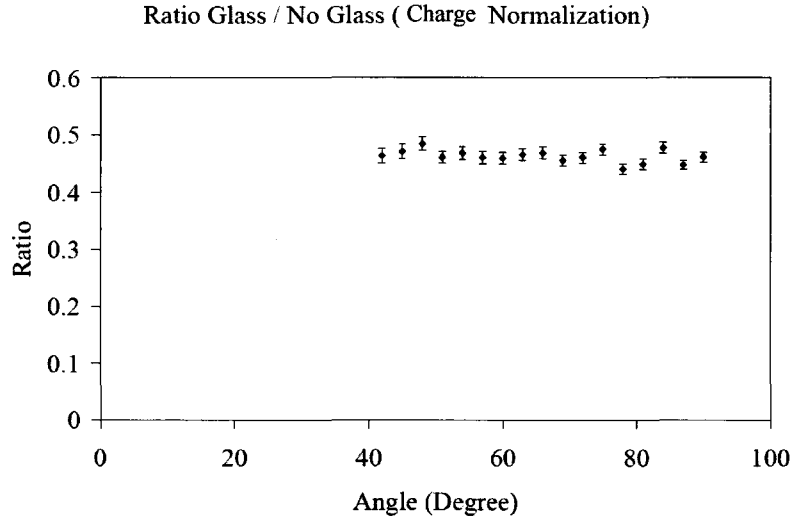

Figure 4.28: Experimental Set 3b: Ratio with Charge Normalization

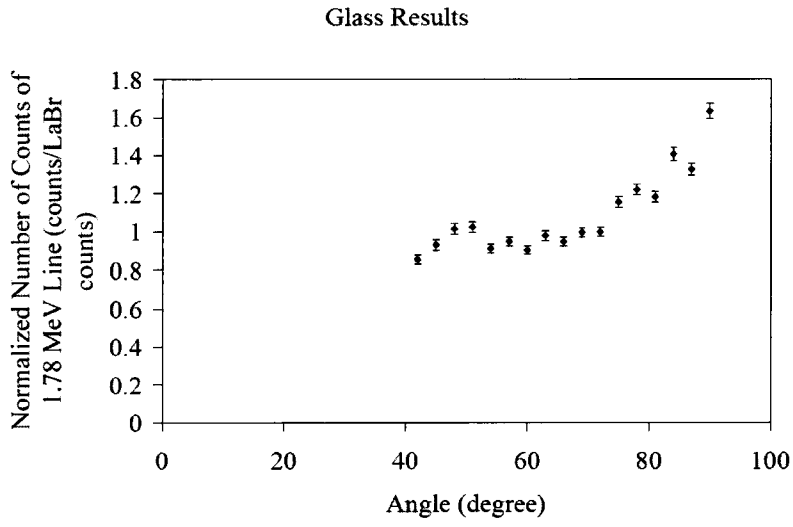

Figure 4.29: Experimental Set 3b: No Glass Results with LaBr Normalization

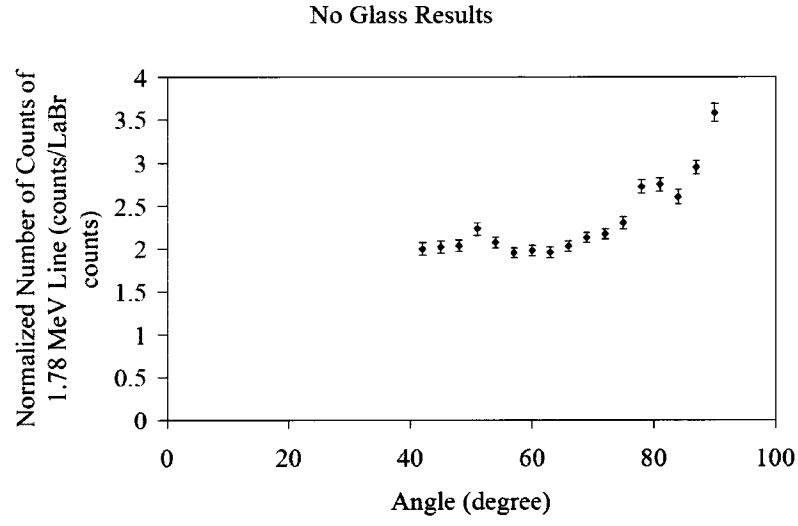

Figure 4.30: Experimental Set 3b: No Glass Results with LaBr Normalization

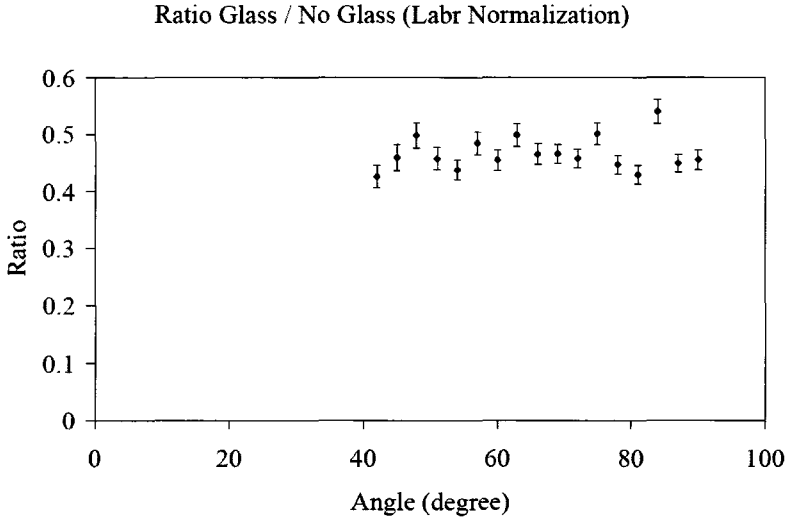

Figure 4.31: Experimental Set 3b: Ratio with LaBr Normalization

and 0.5, as usual. Hence from the results so far we can conclude that the experimental procedure was valid, unfortunately it could not lead towards the desired results, since no dip-like feature could be observed. So far, we were able to reproduce the same results three times in a row; one with NaI detector and twice with HPGe detector. Unfortunately, no positive conclusion in regards to the presence of nuclear resonance dip can be drawn from these experiments.

4.5 Experimental Set 4: Comprehensive Narrow Glass Filter Measurements with HPGe Detector

As the title suggests, this experimental set represents a comprehensive and thorough approach in searching for nuclear resonance dip. The nominal proton current at KN accelerator was fixed at its maximum; $60\mu A$, with the usual proton energy of $1.2MeV$. The angular range covered was from 88° down

to 42°, with an angular step of 1°. In total, 94 runs were performed, 47 with the glass filter ($30min$ real time per run) and the corresponding 47 without the glass filter ($10min$ real time per run). The whole experimental set took 12 working days to complete. The experimental design was somewhat different and more complicated compared to the previous ones. Three detectors were used. HPGe detector and small NaI (3" by 3") scintillator for direct, angle dependent, collection of $1.78MeV$ gamma rays together with fixed large NaI detector for normalization purposes. The large NaI detector was at the same position throughout the duration of the experiments. The HPGe detector was placed behind a $20cm$ by $20cm$ glass filter, sandwiched by a lead collimator. The face of the HPGe detector was completely shielded by the collimator and glass filter. The width of the glass filter was $4mm$. The midpoint of HPGe detector was aligned with a midpoint of Al target. The total distance between HPGe and Al target was $27cm$ ($20cm$ of a collimator plus another $7cm$ from the other side of a collimator to the Al target). The small NaI detector was placed $5cm$ above the mid point of the lead collimator, facing it upside down. The distance between the midpoint of the small NaI detector and the Al target was close to $23cm$. Figures 4.32 and 4.33, respectively represent y and z planes, of the experimental site. Obviously, a small NaI scintillator is used for benchmark purposes, as an additional monitor only and for checking the validity (precision) of an experiment. No resonantly absorbed features would be seen using this detector. In other words, one can expect glass / no glass ratio of 1, when this detector is analyzed. A constant ratio of 1 would be good indication of the stability of the proton beam and precision of the experiment itself.

Figure 4.32: Experimental Setup: Narrow Glass Collimator y plane view

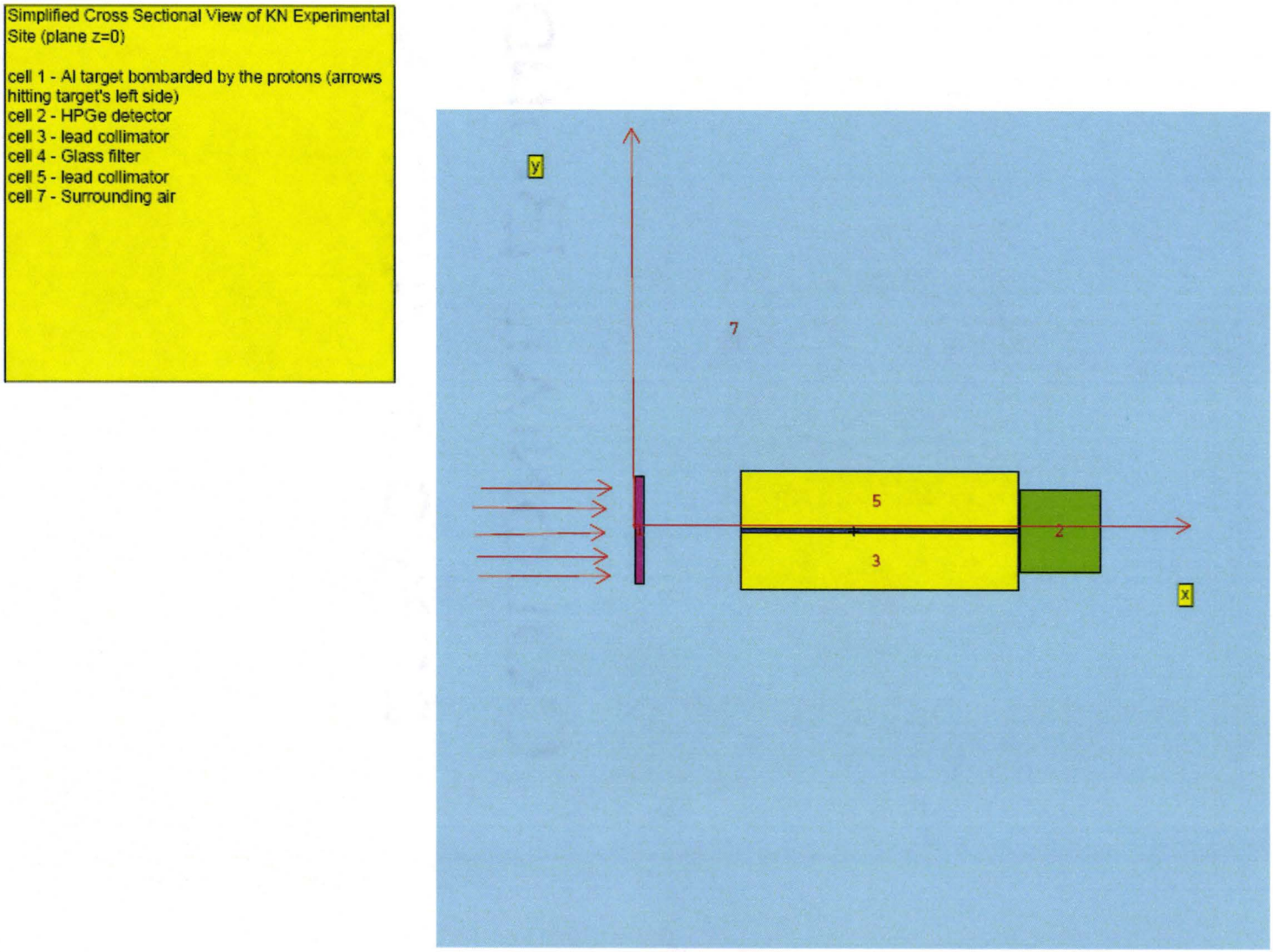

Figure 4.33: Experimental Setup: Narrow Glass Collimator z plane view

The large NaI detector is not included in the figures, since it was fixed at one position and was not moved throughout the set of measurements. The results of these measurements will be organized in three subsections. Firstly, we will compare glass and no glass runs of angle dependent detectors; (small NaI and HPGe). The comparison will include only net count results, without any normalization, since the data were taken simultaneously, at the same angle for each detector. The dead time correction will be applied only. Secondly, a single detector will be compared in glass and no glass runs, i.e. HPGe glass and no glass runs are going to be compared and small NaI glass and no glass runs will be compared. In this case, a charge normalization will be applied. Clearly, since this is not inter-comparison between different detectors in the same run, a normalization is required. Finally, the third subset is the same as the second one, however, large fixed NaI detector normalization will be applied instead.

4.5.1 Direct Comparison of Angle Dependent Detectors

This section describes ratio of total counts of HPGe detector over small NaI detector for glass and no glass runs. Since, experimental conditions for the small NaI detector were the same in either set, we have approximately 10 times higher ratio for no glass runs (the thickness of glass filter was $20cm$). The results are given in figures 4.34 and 4.35.

As expected, the ratio is approximately 10 times higher for the glass runs. However, there are couple of inconsistencies in both figures. In the first figure, the ratio reads between 0.005 and 0.006 for the angular range between 88° and

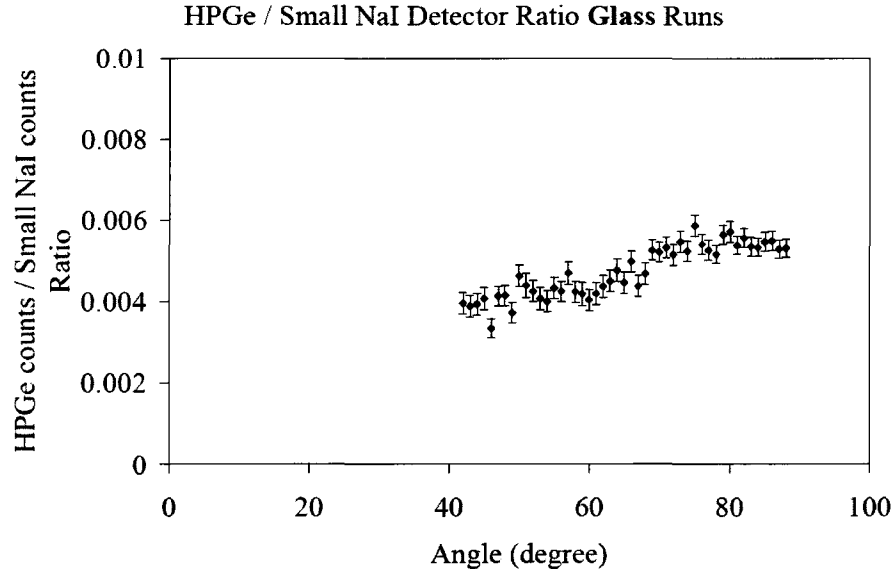

Figure 4.34: Experimental Set 4a: HPGe / Small NaI Ratio for Glass Runs

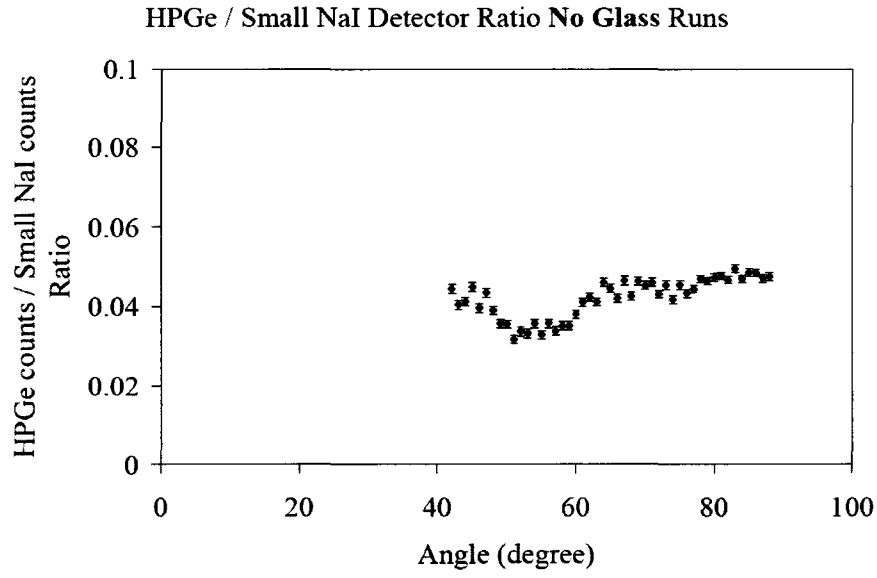

Figure 4.35: Experimental Set 4a: HPGe / Small NaI Ratio for no Glass Runs

65°, and then it drops to approximately 0.004 below 65° and all the way down to the last measurement at 42°. Moreover, in the second graph, the ratio stays constant between 0.04 and 0.05, with visible dip to 0.03 between 49° and 60°. At the beginning it was expected that the ratio in both cases (glass and no glass) had to be relatively constant. However, by careful examination of the experimental geometry, it was found that the two angles of interest, i.e. the angle between proton beam and small NaI detector (φ) and the angle between proton beam and HPGe detector (θ) were not the same. In fact, they are related by the following equation:

$$\cos\varphi = -\frac{r}{\sqrt{r^2+h^2}}\cos\theta \tag{4.15}$$

Where r represents the shortest distance between small NaI detector and vertical line that runs through the center of Al target and h represents the distance between small NaI detector and the line that connects center of Al target with the center of HPGe detector. The detailed derivation of this equation is given in appendix A. In our case, $r = 17cm$ and $h = 15cm$, hence the equation will read:

$$\cos\varphi = -0.75\cos\theta \tag{4.16}$$

This tells us that there is a significant discrepancy between the angles of interest. For example, when $\theta = 60°$, $\varphi = 112°$ and when $\theta = 40°$, $\varphi = 125°$. In general, the angle θ varies between 0 and 90°. At the same time, the angle φ will vary between 139° and 90°. Therefore, when doing simultaneous comparison between small NaI and HPGe detectors we are not including the same angular distribution. Furthermore, by thorough examination of KN accelerator's conditions during these runs, it was found that there were sig-

nificant energy fluctuations between $1MeV$ and $1.3MeV$, during the no glass runs. Particularly, fluctuations occurred because of the accelerator's vacuum pump problems during the no glass runs between 57° and 48°, which clearly corresponds to the evident drop in ratio to 0.3, in figure 4.35. These energy fluctuations can cause different numbers of resonances to be included, or excluded, and hence significantly different fluence rates of $1.78MeV$ gamma rays. Also, it was found that energy fluctuations caused the proton beam shape to change, as well as the spots on the Al target where the beam actually hits. The latter can significantly change the experimental geometry itself. The vacuum pump was replaced after the complete experimental set was finished. However, it is good to keep in mind that the experimental uncertainties caused by these errors have significant influence on experimental precision and results presented in the following sections.

4.5.2 Charge Normalization Results

The following are glass and no glass results, along with their ratios for HPGe and small NaI. This particular subsection represent normalized results using time integrated proton current, or total proton charge accumulated on the Al target. There are 6 figures in total. The first three represent a HPGe results and following three represent small NaI results. To remind the reader, the expectation for small NaI scintillator results is the RATIO of 1 for glass / no glass.

There is a similar pattern in HPGe glass and no glass results; figures 4.36 and 4.37. Furthermore, these are similar to the small NaI results; figures 4.39

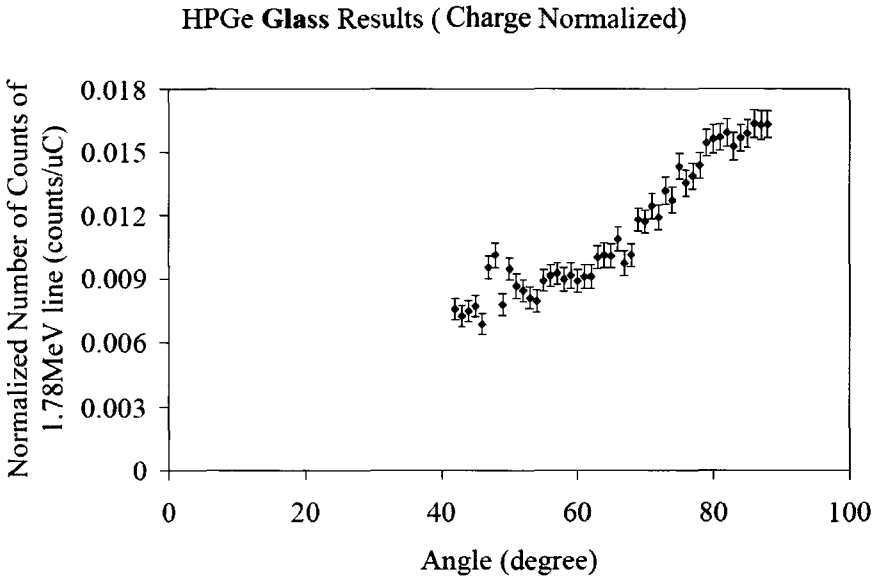

Figure 4.36: Experimental Set 4b: HPGe Glass Results with Charge Normalization

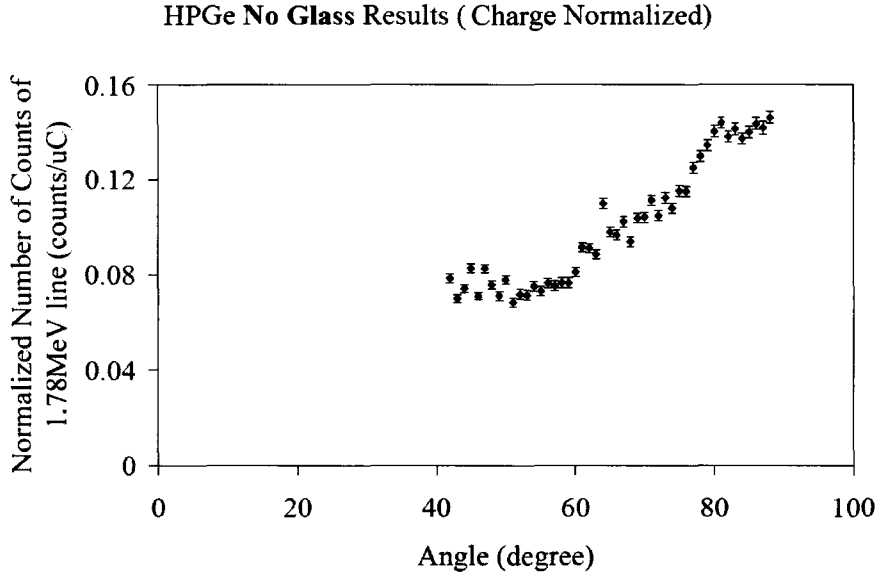

Figure 4.37: Experimental Set 4b: HPGe No Glass Results with Charge Normalization

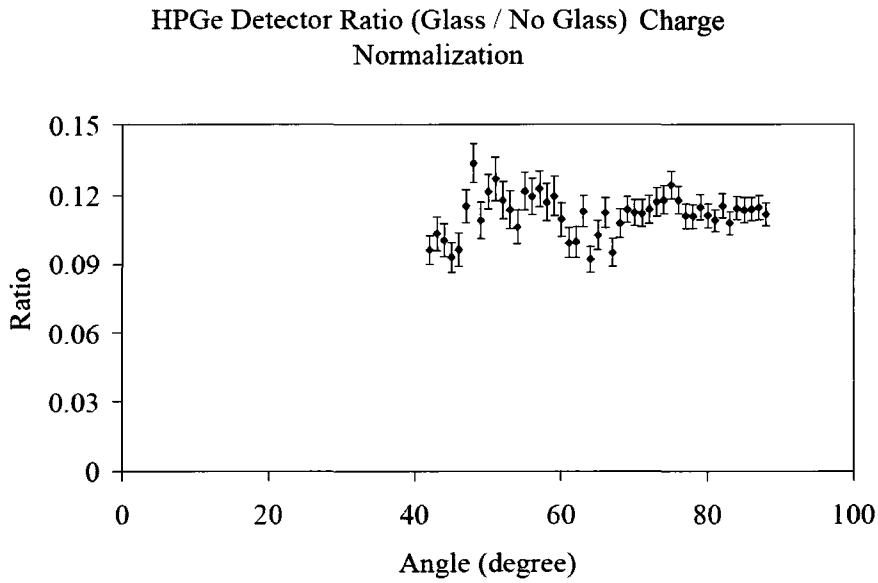

Figure 4.38: Experimental Set 4b: HPGe Ratio with Charge Normalization

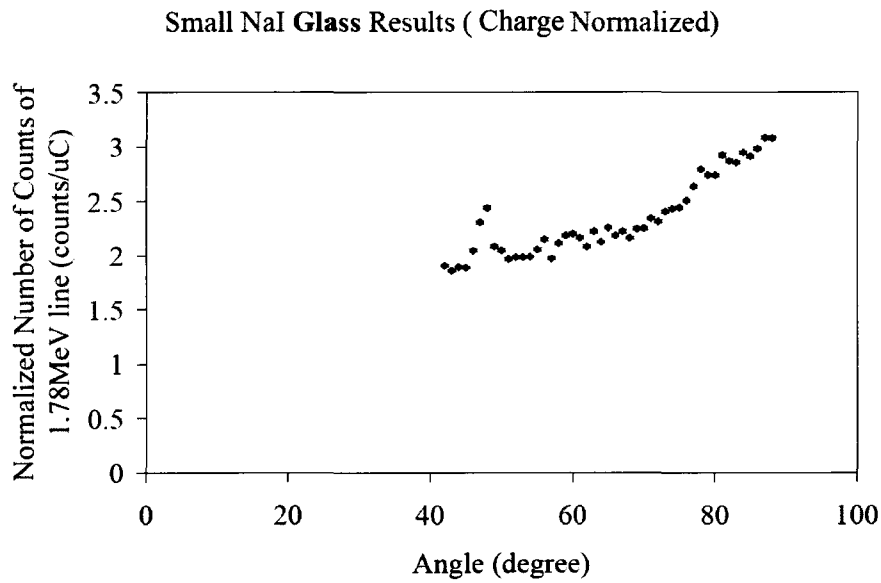

Figure 4.39: Experimental Set 4b: Small NaI Glass Results with Charge Normalization

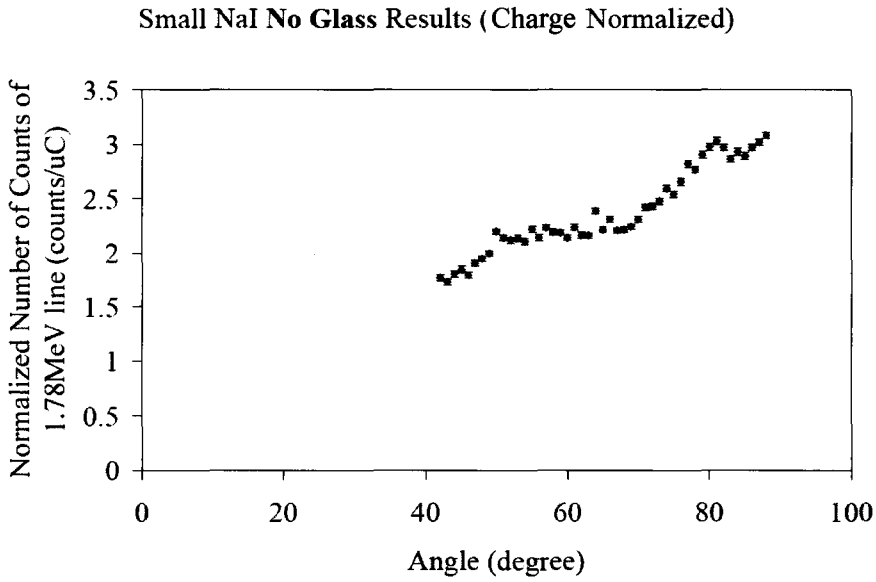

Figure 4.40: Experimental Set 4b: Small NaI No Glass Results with Charge Normalization

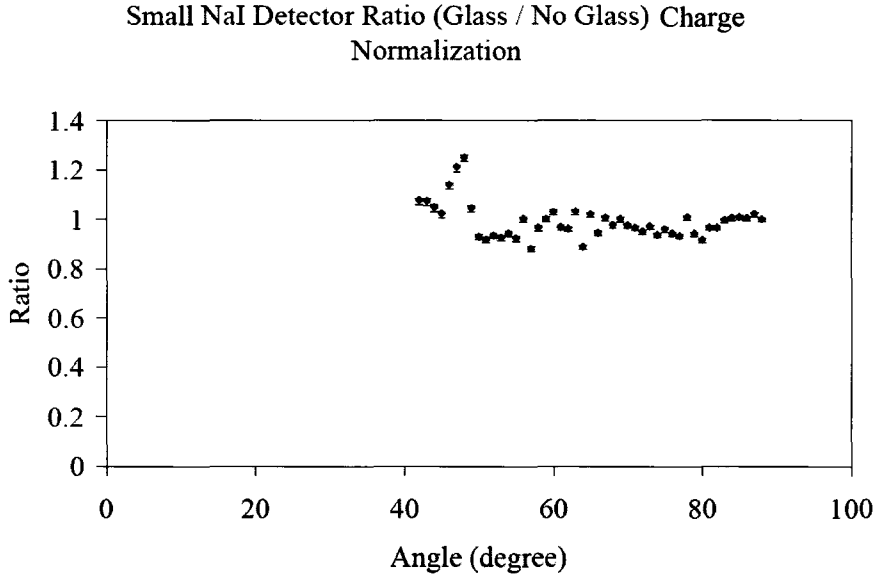

Figure 4.41: Experimental Set 4b: Small NaI Ratio with Charge Normalization

and 4.40, with the exception of the small increase in counts in the small NaI glass results; figure 4.39. This suggests a possible angular distribution of $1.78MeV$ gamma rays. Particularly, this peak is located between 45° and 51°. This inconsistency could be explained by the experimental uncertainties discussed. The small NaI results are further summarized in the ratio graph, figure 4.41. This figure gives steady ratio value of approximately 1, as expected, with a significant peak between 45° and 51°, resulting from the small NaI glass measurements, discussed above. As far as the HPGe ratio is concerned, it fluctuates around 0.1, which is in full agreement with theoretical calculations ($20cm$ long glass absorber). Furthermore, there is a significant sign of a decreasing ratio between 58° and 72°. Also, there is a small drop of ratio at approximately 46°. The former one is of particular interest, since the feature is preserved in the results that follow (large NaI normalization).

4.5.3 Large NaI Normalization Results

Finally, the following 6 figures represent the same set of results as the previous 6 figures. In this case however, for normalization purposes, a large NaI detector was used, instead of proton charge. The HPGe glass and no glass results; figures 4.42 and 4.43 do have very similar patterns. Also it is very similar to the HPGe results from the previous section, when charge normalization was performed. The ratio of HPGe results, given in figure 4.44 is again very similar to the HPGe ratio from charge normalization results, with fluctuations around 0.1. Also, the dip like feature between 58° and 72° is present. Therefore we can conclude that HPGe results for the complete

experimental set are very stable and that the dip like feature is reproducible using either normalization. However, it is not very significant, so that we cannot draw any conclusions regarding it as a possible representation of an actual nuclear resonance absorption dip. Furthermore, the small NaI no glass results, normalized by the large NaI counts; figure 4.46, experience a wide increment (peak) between 46° and 63°. Again, this is probably due to the experimental uncertainties described earlier. It is also carried through to the ratio graph, figure 4.47. Now, in order to eliminate uncertainties and errors due to the angular discrepancies between small NaI and HPGe detector, it was decided to modify the experimental site, as well as to introduce a thin *Al* targets. This is described in the sections to follow.

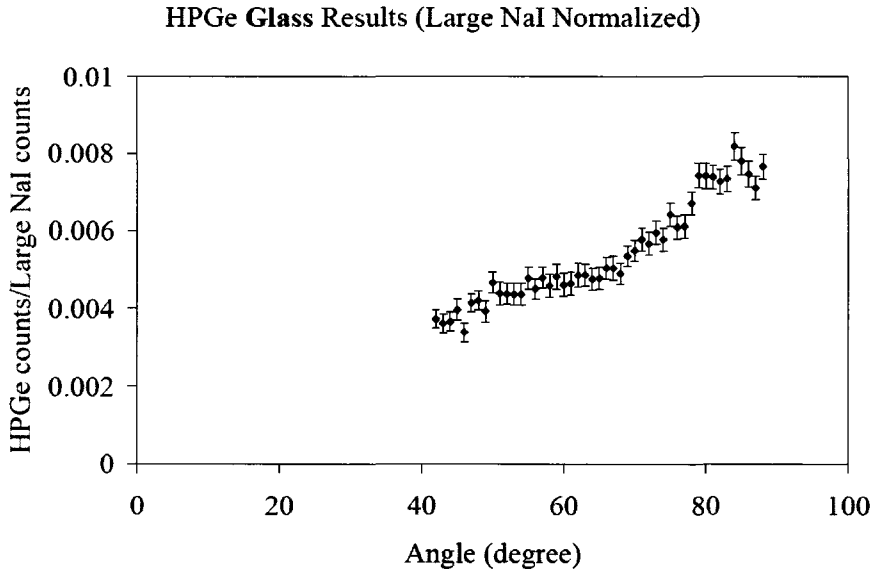

Figure 4.42: Experimental Set 4c: HPGe Glass Results with Large NaI Normalization

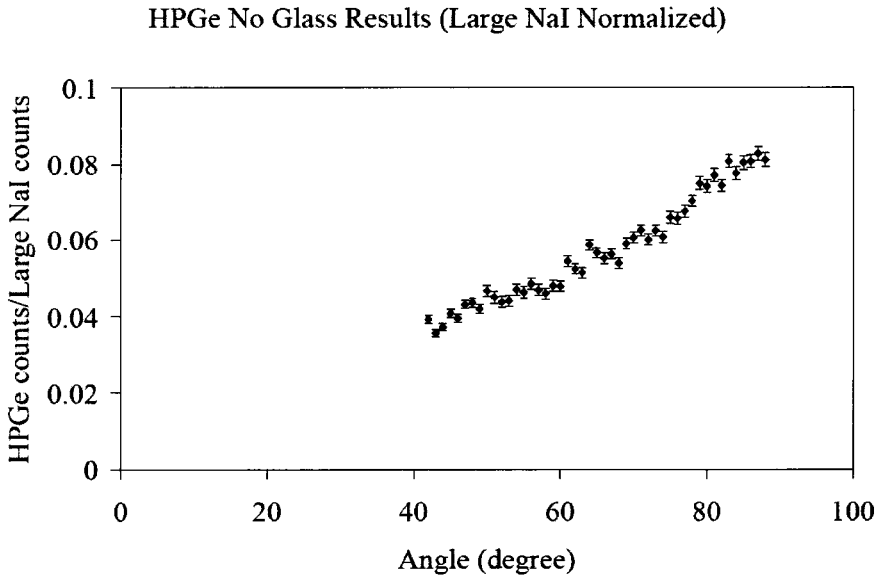

Figure 4.43: Experimental Set 4c: HPGe No Glass Results with Large NaI Normalization

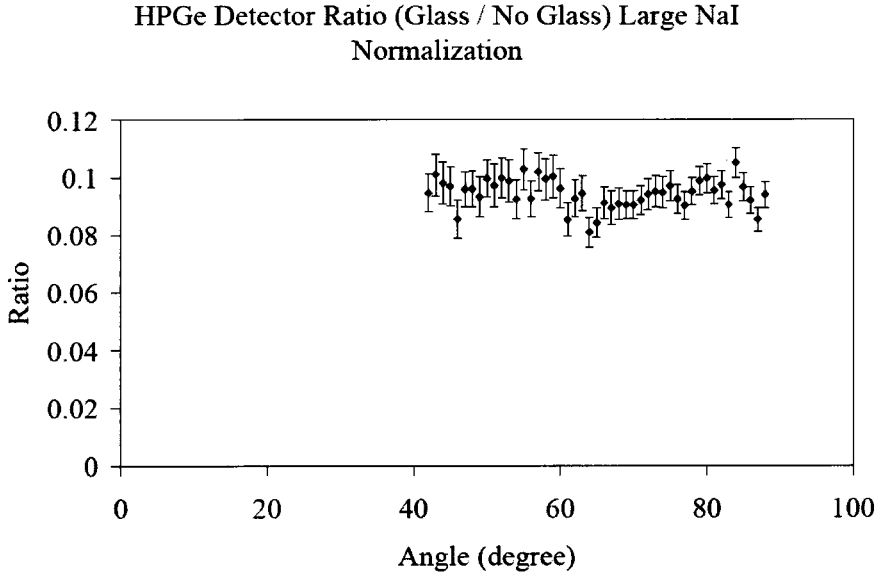

Figure 4.44: Experimental Set 4c: HPGe Ratio with Large NaI Normalization

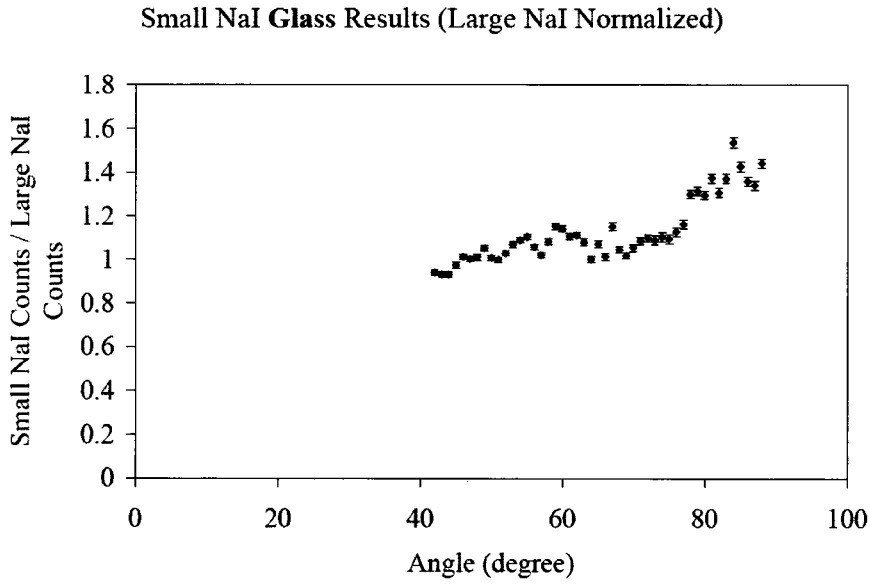

Figure 4.45: Experimental Set 4c: Small NaI Glass Results with Large NaI Normalization

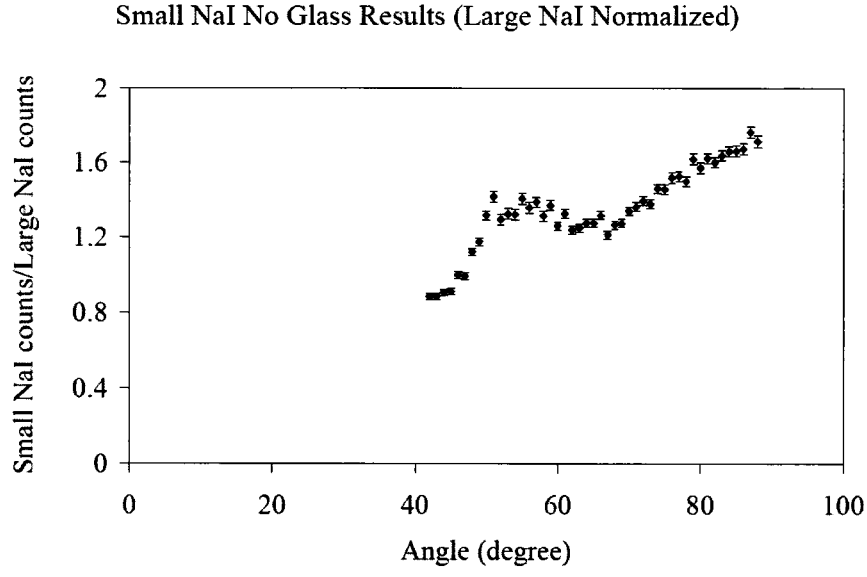

Figure 4.46: Experimental Set 4c: Small NaI No Glass Results with Large NaI Normalization

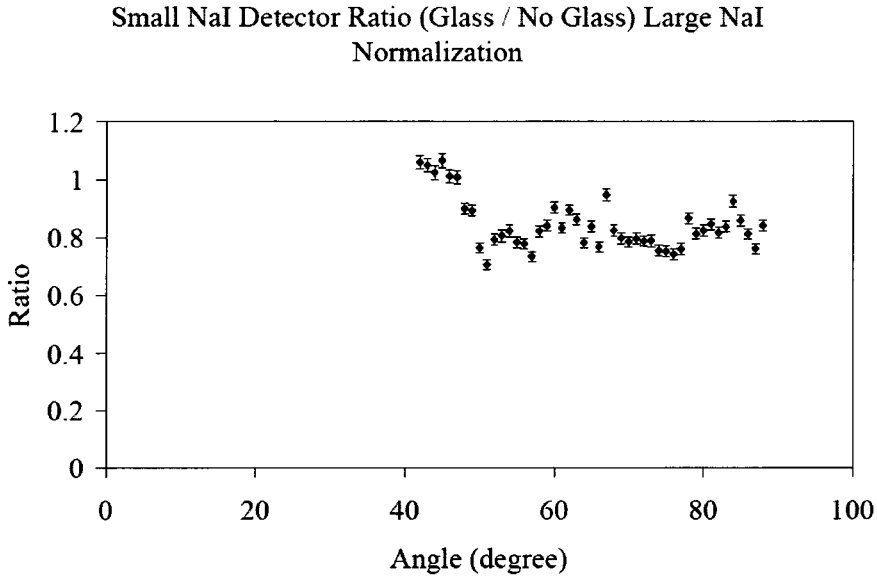

Figure 4.47: Experimental Set 4c: Small NaI Ratio with Large NaI Normalization

4.6 Experimental Set 5: Vertically Symmetrical Arrangement of HPGe and Small NaI Detectors

As the title suggests this section describes two experimental sets where the movable small NaI detector was placed in a vertically symmetrical position with the HPGe detector, with respect to the proton target. This is pictured in figure 4.48. This way, we have ruled out the obvious angular discrepancy between two detectors. From our discussion in the previous section and from the appendix calculations, it is evident that the angle of interest for the HPGe detector and the small movable NaI detector is drastically different. Hence, we decided to fix that and to determine the relationship in counts for these detectors experimentally, when they are vertically symmetrical with respect to the proton Al target. In this case, the angle of interest is identical for both

detectors. Logically, we expected a relatively constant ratio between detectors' counts.

Figure 4.48: Experimental Setup: Vertically Symmetrical Arrangements of Small NaI and HPGe Detectors

Two independent and identical experiments were performed on two consecutive days. On each day, 8 measurements were taken, $30min$ each, with both detectors, simultaneously. The usual KN operating conditions were maintained; $60\mu A$ of nominal proton current at $1.2MeV$ fixed energy. Large angular steps of 5° and 10° were taken, from 80° down to 30°. The first and second day results are presented below in figures 4.49 and 4.50, respectively. Furthermore, day 1 / day 2 ratio of the results is presented in figure 4.51

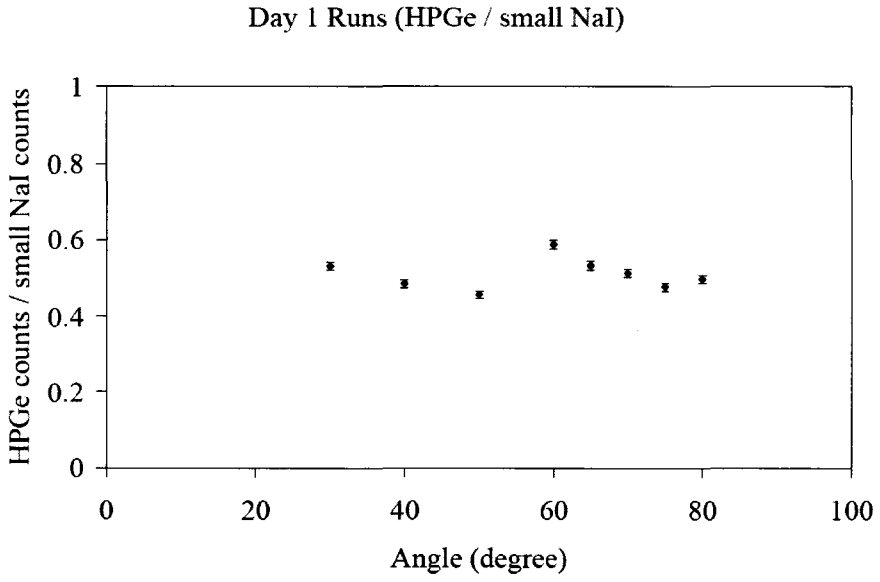

Figure 4.49: Experimental Set 5: Day 1 Results

Evidently, day 1 and day 2 results have identical relationship with respect to the angle. The ratio of detectors' counts follows the identical pattern on day 1 and day 2. Also, the ratio is relatively constant, as we have expected. The mean ratio value (HPGe counts / small NaI counts) on day 1 is 0.51, with standard deviation of 0.041, (8.05%) while mean ratio on day 2 is 0.47, with standard deviation of 0.035 (7.37%). Moreover, day 1 / day 2 ratio gives mean value of 1.083, with standard deviation of 0.034 (3.12%). The results are as

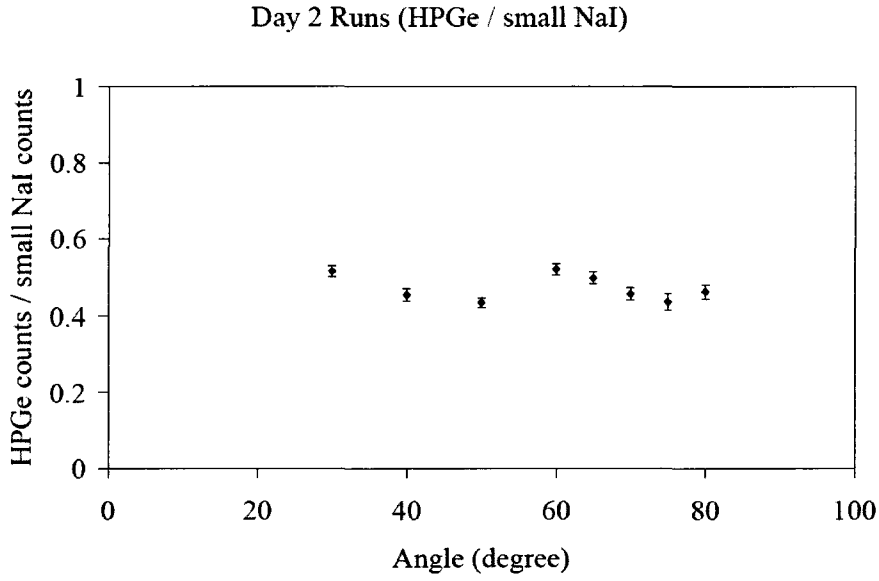

Figure 4.50: Experimental Set 5: Day 2 Results

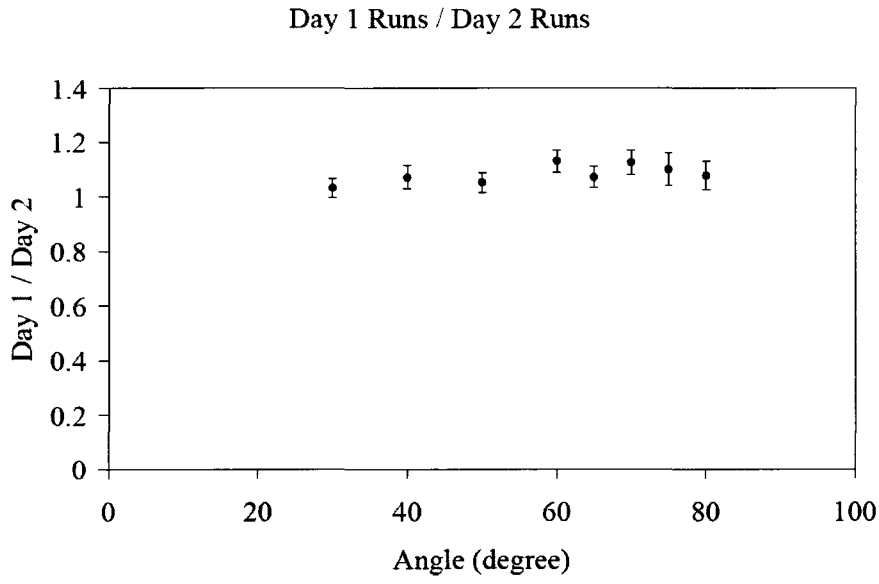

Figure 4.51: Experimental Set 5: Day 1 / Day 2 Ratio

expected and this detector arrangement was adopted for the following detailed experimental set, where a thin Al proton target was introduced for the first time.

4.7 Experimental Set 6: Preliminary Thin Target Experiments for Accurate Proton Energy Calibration

As outlined in the previous section, from the thick Al target, where all possible resonances can be included, we decided to switch to the thin target and to focus on a single and strongest resonance; $12.542MeV$, populated by $992keV$ protons. The experiments are very similar to the one performed in chapter 3. For this purpose, 4 identical thin targets were prepared by evaporating Al onto a copper backing. The Al thickness on each target was $0.4\mu m$. According to Meyer [57], there are 4 resonances nearby the $992keV$ resonance that might be of interest. Two of them are below and the other two are above $992keV$ resonance. Those are $923keV$ ($12.475MeV$ level occupied, with 91% branching to the $1.78MeV$ first excited state), $937keV$ ($12.489MeV$, 48% branching), $1002keV$ ($12.552MeV$, 64% branching) and $1025keV$ ($12.574MeV$, 26% branching). Obviously, the closest one is the $1002keV$ resonance, with only $10keV$ energy difference. Firstly, using the approach from section 3.1 and equation 3.2, we can convert the stopping power vs energy into the energy loss as a function of distance. This is shown in figure 4.52.

From these calculations, for the given Al target thickness, it is evident that the $992keV$ resonance can interfere with the $1002keV$ resonance only, and

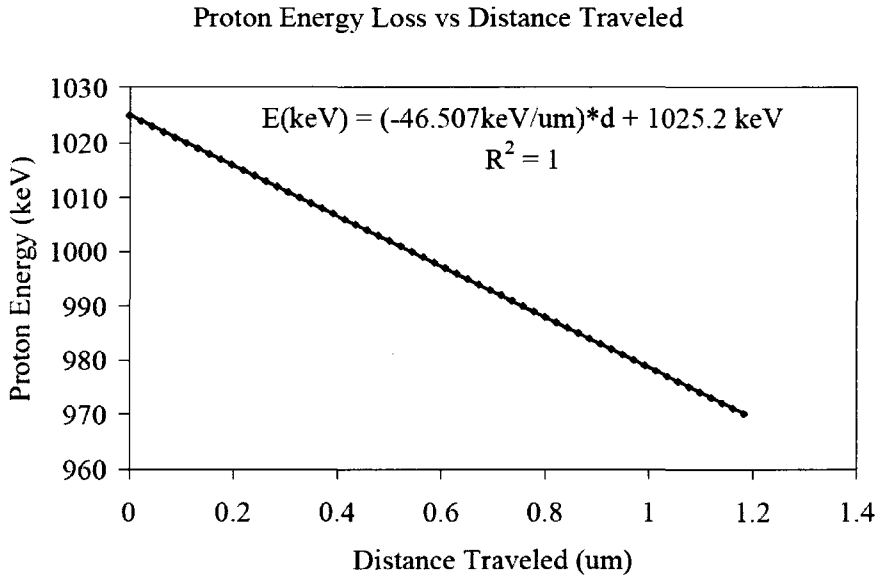

Figure 4.52: Proton Energy Loss vs Distance Traveled

there would be absolutely no interference with the other nearby, (above listed) resonances. However, Chronidou [58] and Harissopulos [56] in their articles do not mention the $1002keV$ resonance as one with a significant strength. Therefore, its gamma yield is insignificant, as well. Finally, it can be concluded that $992keV$ resonance is very well isolated and it has great potential for thin target measurements. The accelerator was started at $980keV$ and the energy was gradually raised by $1keV$ for each run. The $1.78MeV$ gamma line did not appear until we hit $1008keV$ proton energy, it peaked up at $1012keV$ and finally the plateau was formed at $1014keV$. This is shown in figure 4.53.

Evidently, according to this experiment, the KN machine was not properly calibrated. It was shifted up by approximately $22keV$. The same feature was observed in chapter 3 with $771keV$ protons. Therefore, we had to take that into the account when running thin target experiments. Also from figure 4.53,

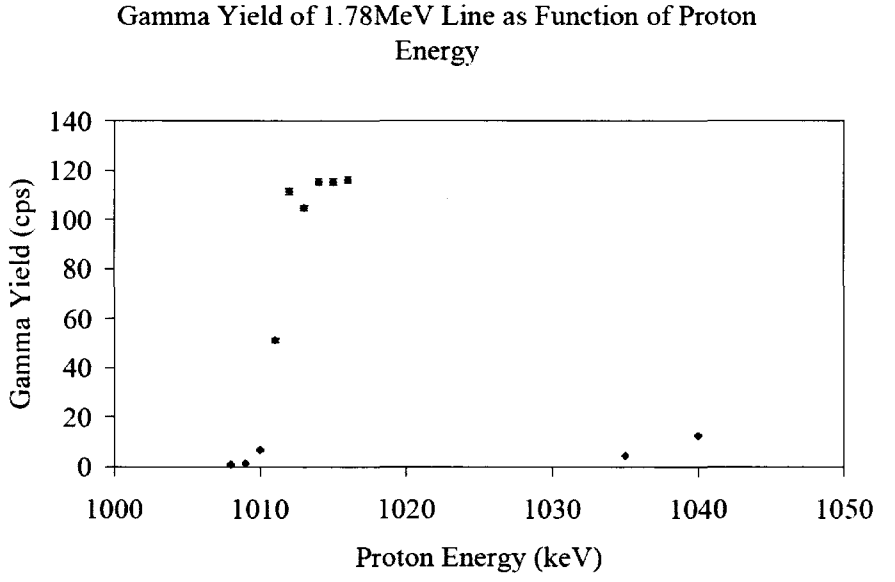

Figure 4.53: Gamma Yield as a Function of Proton Energy

it is clear that the gamma yield drastically drops by $1035keV$, since the $992keV$ resonance is avoided in this case. Lastly, during these experiments it was noted that the total gamma yield from $1.78MeV$ line dropped by approximately 40% when compared to the thick target experiments. This indicates that only a single proton resonance $992keV$ accounts for 60% of a total $1.78MeV$ gamma ray yield. After the calibration, we were ready for another comprehensive set of experiments with the thin Al target.

4.8 Experimental Set 7: Vertically Symmetrical Arrangements of HPGe and Small NaI Detector; Thin Target Comprehensive Set

This was the last experimental set where the $1.78MeV$ gamma line was observed for nuclear resonance absorption. In this comprehensive set we used

a thin Al target. Also, the energy of proton beam was fixed at $1014keV$, in order to overcome the KN machine energy shift and to center the energy at the $992keV$ resonance. Two Al targets were used, with constant rotation, in order to preserve their freshness and to avoid deterioration as much as possible. It is important to mention here that we were able to hit three independent fresh spots at the single target by two rotations of 120°. Hence, with this method, the lifetime of the same target was maximized. As the title suggests, the detector setup was vertically symmetrical as pictured in figure 4.48. The distance between Al target and detectors was $32cm$. The usual lead collimator was used with $a6mm$ thick and $20cm$ long glass absorber. The angular range covered was from 80° down to 30°, with 1° decrement. In total, 51 glass data points ($30min$ real time per run) and 51 no glass data points ($10min$ real time per run) were collected during the course of 10 working days. The fixed large NaI detector was used for normalization purposes, together with total, time integrated current. The results are organized as usual, in the same manner as in section 4.5.

4.8.1 Direct Comparison of Angle Dependent Detectors

The first two graphs; figures 4.54 and 4.55 represent the ratios of HPGe and small NaI detectors for glass and no glass runs. As before, no normalization is required since we are comparing data that have been collected simultaneously. Our expectation was a steady and constant ratio for both comparisons. Also, the glass ratio should be approximately 10% of a non glass ratio, since the glass filter was present in front of the HPGe detector only, during the glass

runs. No glass filter was present in front of the small NaI detector in either case.

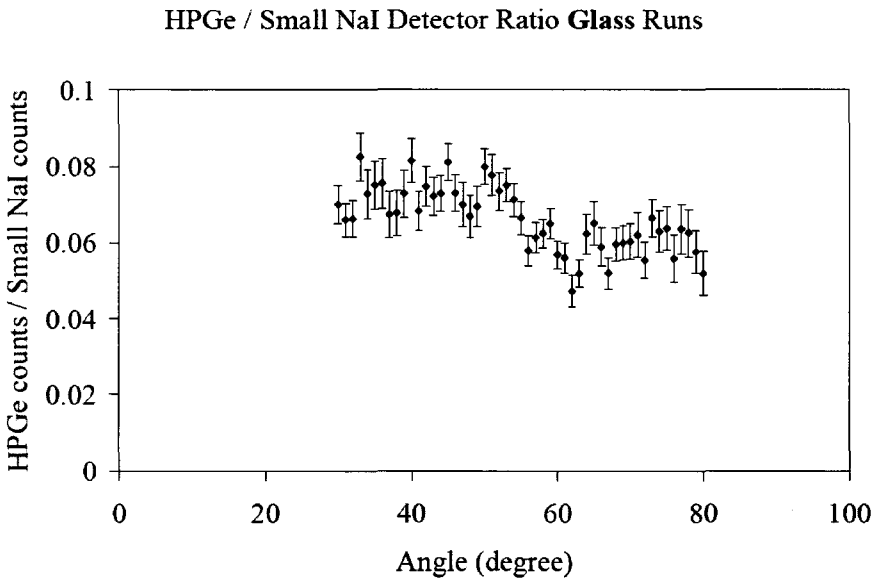

Figure 4.54: Experimental Set 7a: HPGe / Small NaI Ratio for Glass Runs

Looking at figures 4.54 and 4.55, we can conclude that the average ratio of glass case is indeed approximately 10% of no glass case. Unfortunately, the graphs do not show a constant and steady ratio as expected. Especially, this is the case with no glass ratio, where it fluctuates between 0.4 and 0.7, with evident decrease from 77° down to 65° and then a sudden increase all the way down 30°. The glass ratio is somewhat more stable and reads approximately 0.05 between 80° and 62°. Below that, it smoothly jumps to 0.07 and stays constant all the way down to 30°. Overall, so far, our data analysis shows that there is an obvious problem with the whole experimental set. This will become more obvious in the analysis to follow.

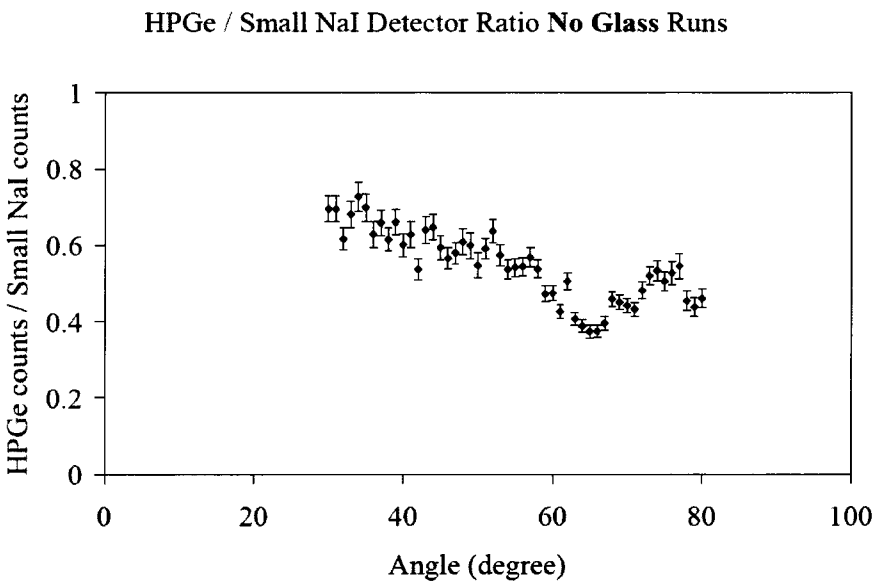

Figure 4.55: Experimental Set 7a: HPGe / Small NaI Ratio for no Glass Runs

4.8.2 Integrated Proton Current Normalization Results

The following 6 figures: 4.56 to 4.61 represent both HPGe and small NaI results, normalized by the total charge. The first three graphs 4.56 to 4.58 correspond to the HPGe detector, while the following three 4.59 to 4.61 correspond to the small NaI detector.

In this experimental subset, similar patterns are observed in both ratio figures 4.58 and 4.61. However, no significant features that could qualify for a nuclear resonance attenuation dip are observed. It can easily be concluded that this set of results differs from the previous ones. Moreover, all the patterns (glass and no glass) for both detectors are significantly different from the patterns in previous experimental sets. One of the possible explanations for these results could be in the duration of the experiment itself (10 working days). This could have caused a deterioration of the already very thin *Al*

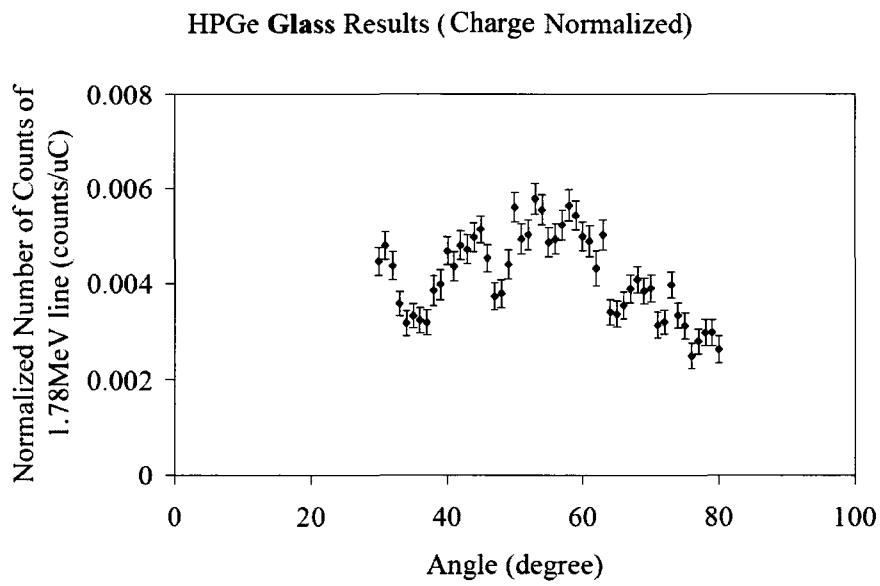

Figure 4.56: Experimental Set 7b: HPGe Glass Results with Charge Normalization

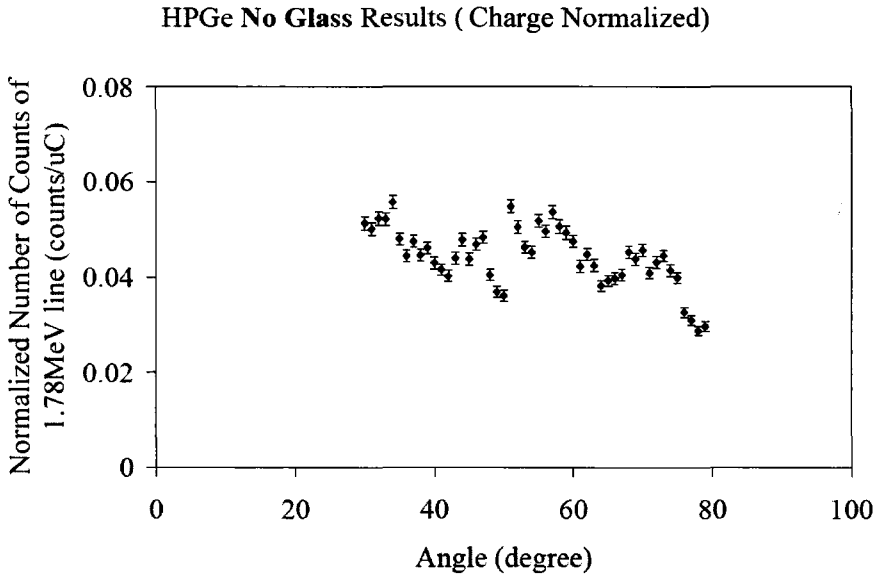

Figure 4.57: Experimental Set 7b: HPGe No Glass Results with Charge Normalization

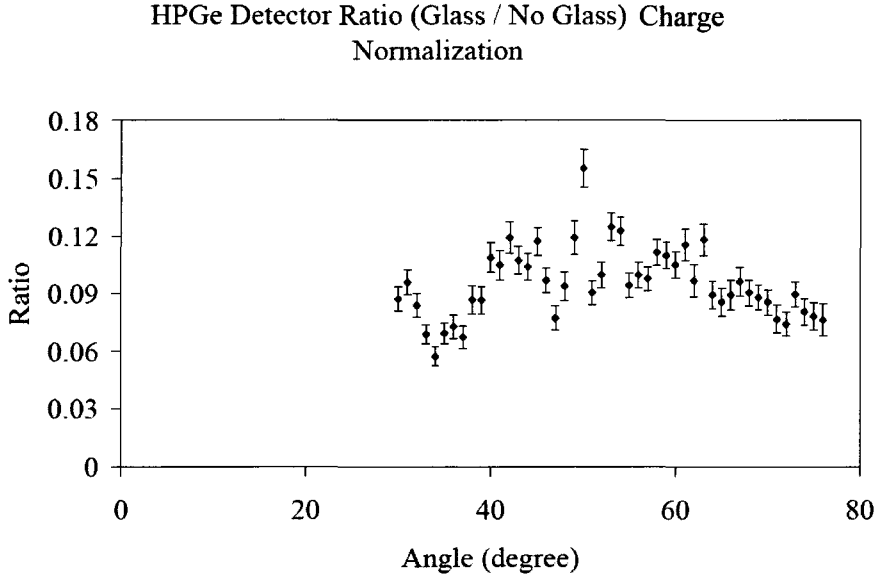

Figure 4.58: Experimental Set 7b: HPGe Ratio with Charge Normalization

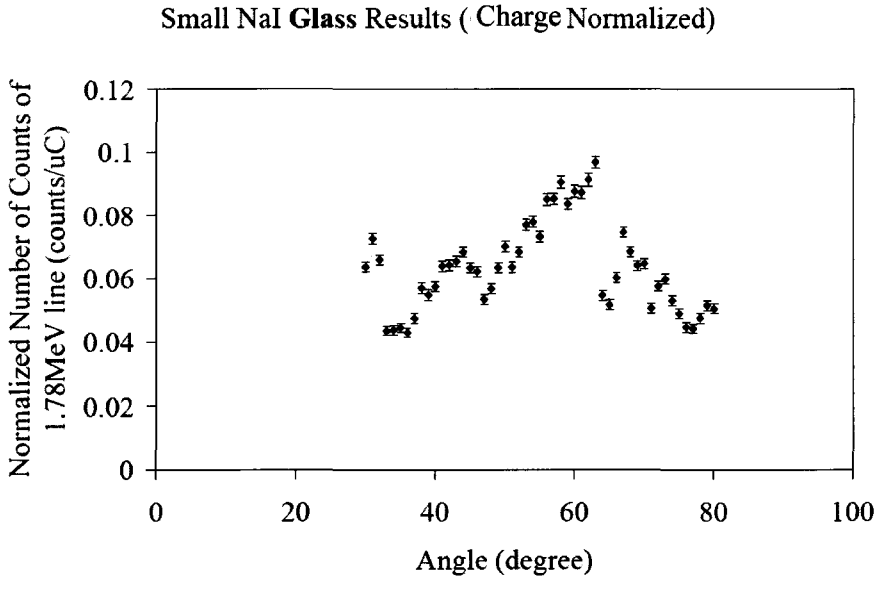

Figure 4.59: Experimental Set 7b: Small NaI Glass Results with Charge Normalization

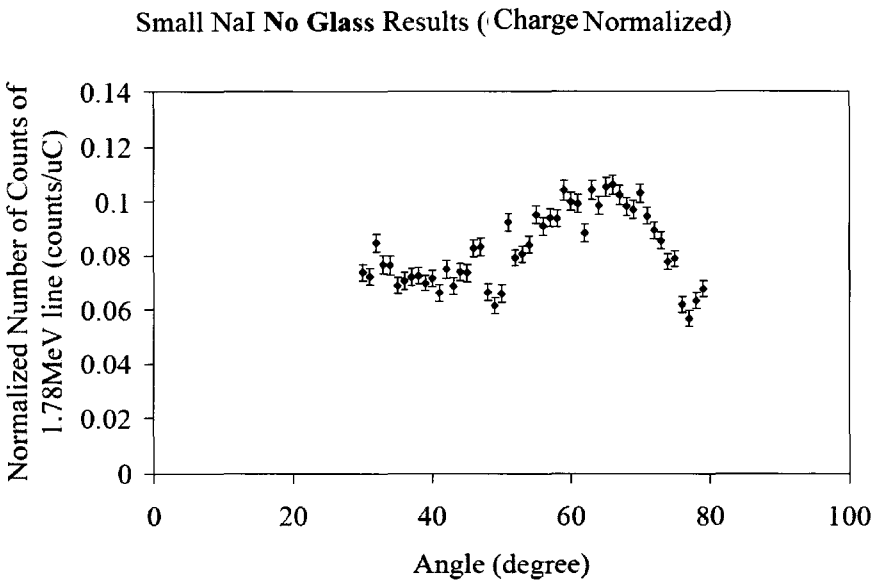

Figure 4.60: Experimental Set 7b: Small NaI No Glass Results with Charge Normalization

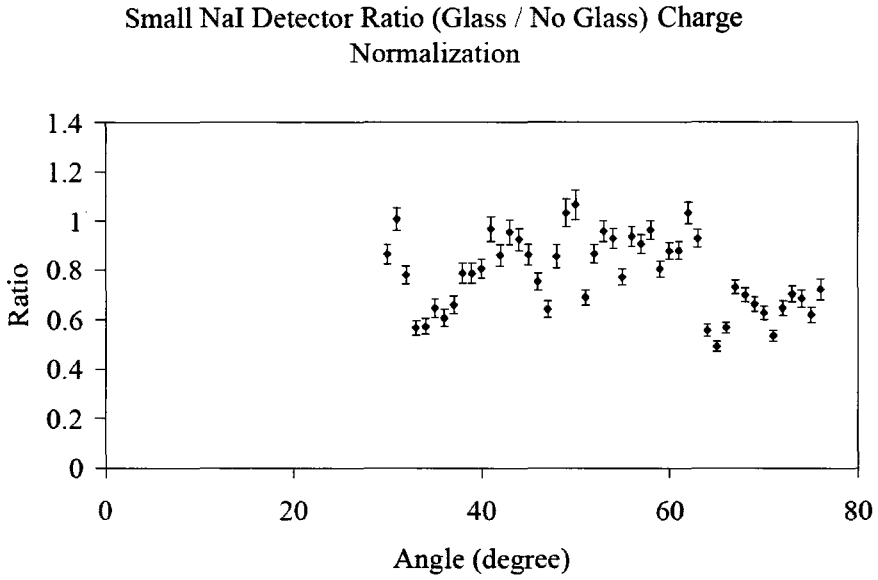

Figure 4.61: Experimental Set 7b: Small NaI Ratio with Charge Normalization

target, regardless constant rotation and constant usage of the fresh parts of the target. Furthermore, since we are using a single resonance, the margin for error in proton energy shift is very small and even slightest energy fluctuations can cause the resonance of importance to be missed. The same explanations can be applied for the following subset as well.

4.8.3 Large NaI Normalization Results

The following 6 figures: 4.62 to 4.67 represent both HPGe and small NaI results, normalized by the counts from large fixed NaI detector. The first three graphs 4.62 to 4.64 correspond to the HPGe detector, while the following three 4.65 to 4.67 correspond to the small NaI detector. Similarly, as was the case with the previous subset, we experienced the same problems here. Therefore, with the present experimental equipment and KN accelerator in the present condition, it may be very hard to use a thin Al target and to induce, or even look for the nuclear resonance absorption phenomenon in Si, with the $1.78MeV$ gamma line. In fact, based on these findings it is very hard to obtain meaningful results at all. All possible logical expectations turned out to be invalid. No reproducible results were seen, as was the case in the previous runs. Indeed, this is the biggest problem for this particular experimental arrangement. The thick target experiments yielded much better and more reproducible results. From these experiments it can be concluded that exposing the thin target to long and durable proton bombardment cannot be the way of exploring nuclear resonance absorption and fluorescence.

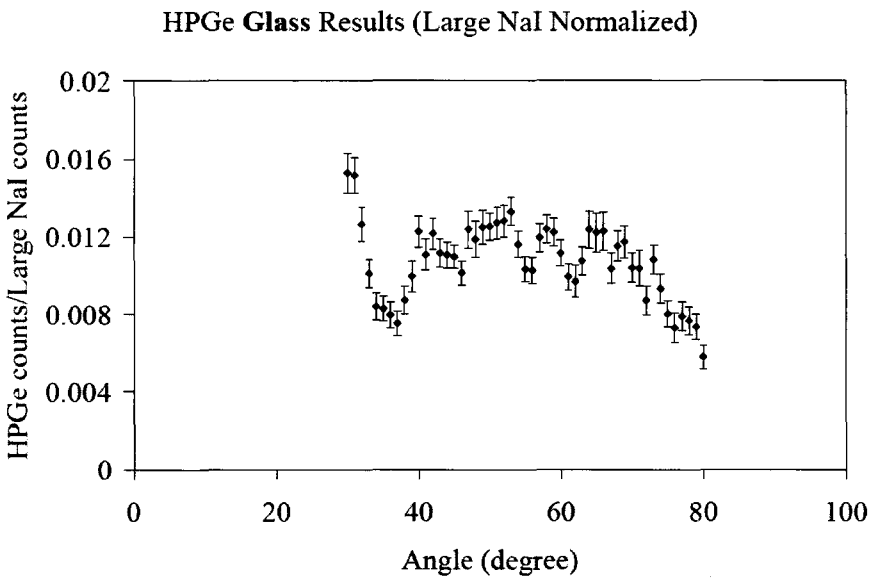

Figure 4.62: Experimental Set 7c: HPGe Glass Results with Large NaI Normalization

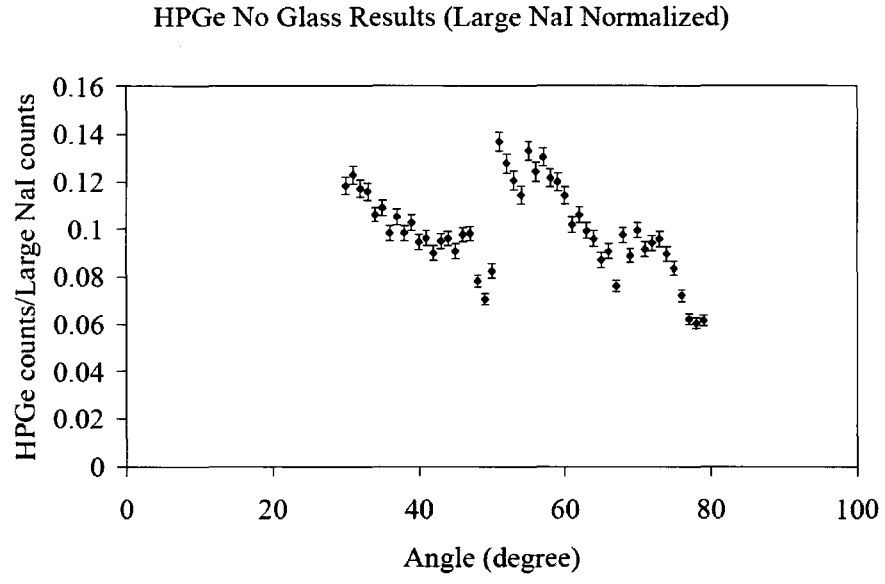

Figure 4.63: Experimental Set 7c: HPGe No Glass Results with Large NaI Normalization

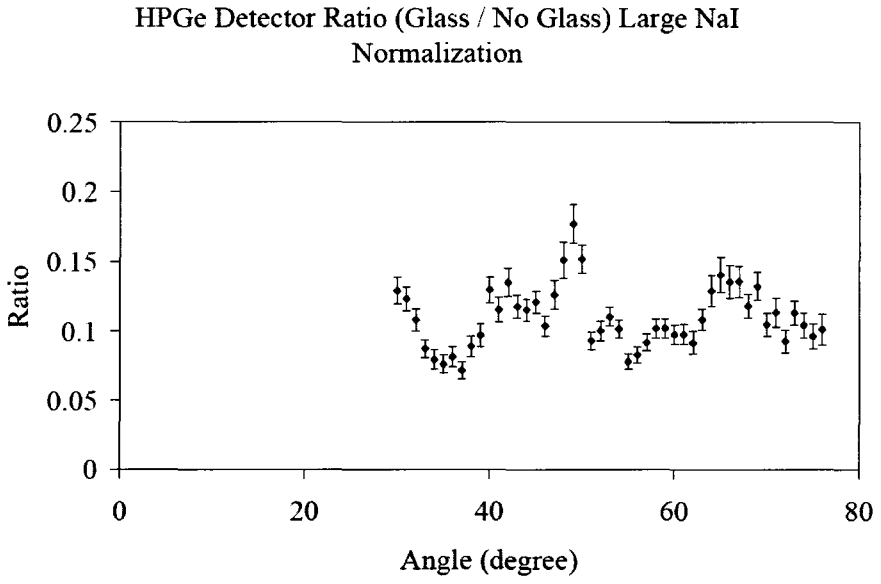

Figure 4.64: Experimental Set 7c: HPGe Ratio with Large NaI Normalization

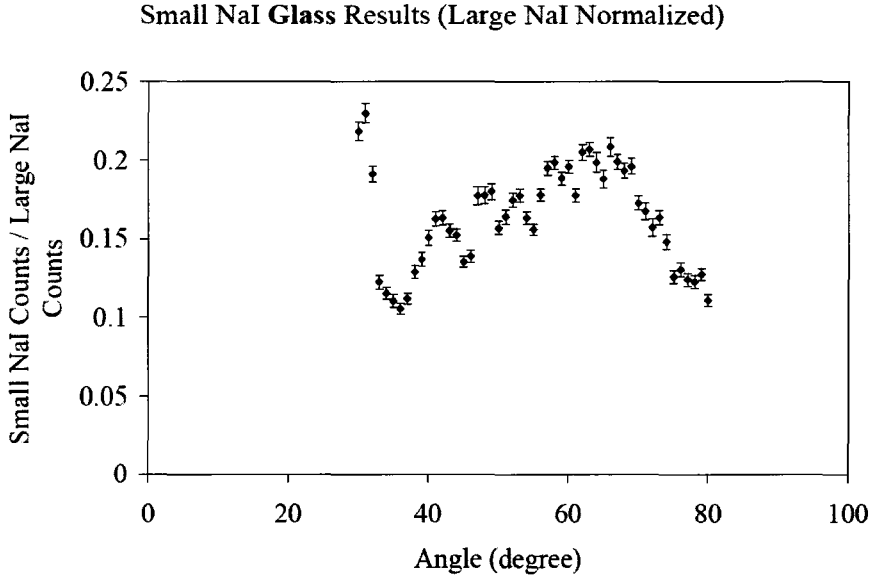

Figure 4.65: Experimental Set 7c: Small NaI Glass Results with Large NaI Normalization

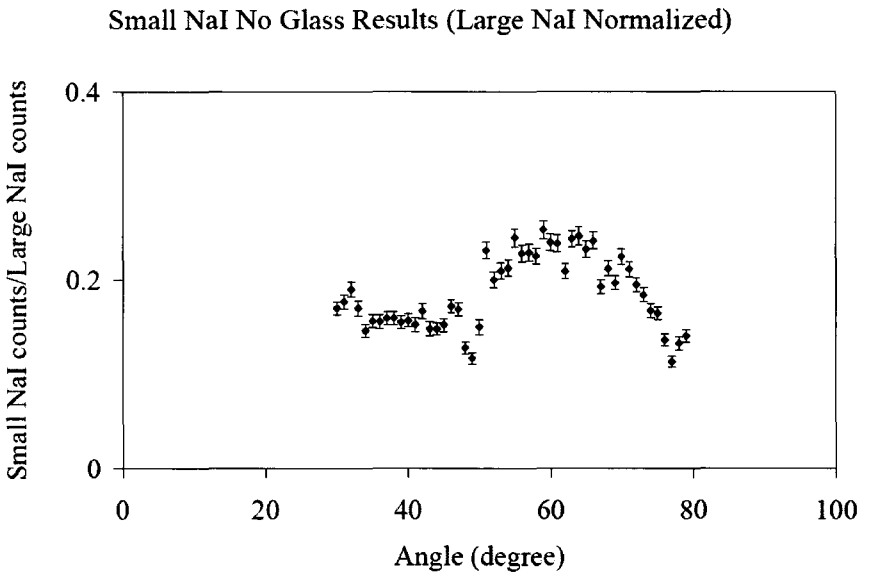

Figure 4.66: Experimental Set 7c: Small NaI No Glass Results with Large NaI Normalization

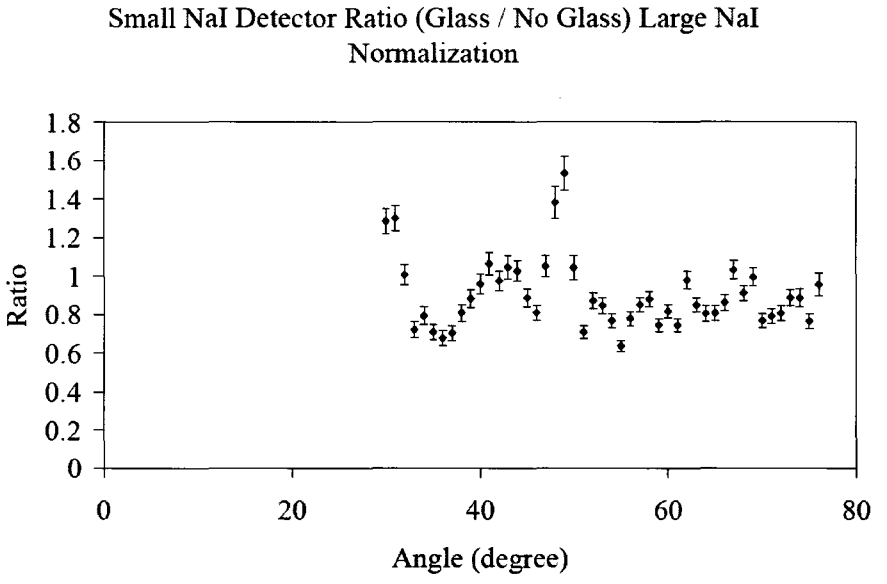

Figure 4.67: Experimental Set 7c: Small NaI Ratio with Large NaI Normalization

4.9 Summary of all Experimental Results in Chapter 4

For clarity, we will summarize the results with all important features obtained with the $1.78MeV$ first excited state of silicon.

EXPERIMENTAL SET #1

- **Detection Used:** HPGe
- **Filter:** Glass vs Al, (width: $2mm$, length: $20cm$), detector-source distance: $47cm$
- **Proton Beam:** $55\mu A$-$60\mu A$, $1MeV$ and $1.2MeV$
- **Normalization:** Charge collection
- **Number of Data Points:** 41 and 25 (two subsets)
- **Results:** Poor statistics, two reproducible subsets, two repetitive dips observed, inconclusive results.

EXPERIMENTAL SET #2

- **Detection Used:** large NaI
- **Filter:** Wide glass filter, (width: $2.5cm$, length $7.5cm$, detector-source distance $47cm$)
- **Proton Beam:** $20\mu A$, $1.2MeV$
- **Normalization:** Charge collection and fixed LaBr detector

- **Number of Data Points:** 21 (3° steps)
- **Results:** Visible V shape response consistent for both normalizations. Steady glass/no glass ratio of 0.4 as expected. No conclusion about possible dip.

EXPERIMENTAL SET #3

- **Detection Used:** HPGe
- **Filter:** Wide glass filter (width: $2.5cm$, length $7.5cm$, detector-source distance $47cm$)
- **Proton Beam:** $30\mu A$, $1.2MeV$
- **Normalization:** Charge collection and LaBr detector
- **Number of Data Points:** 15 and 17 (two subsets)
- **Results:** Subsets reproducible, similar to the previous results. Steady glass/no glass ratio of 0.45 as expected. The results essentially the same as in previous set. No conclusion about possible dip.

EXPERIMENTAL SET #4

- **Detection Used:** HPGe
- **Filter:** Glass, (width: $4mm$, length $20cm$, detector-source distance $27cm$)
- **Proton Beam:** $60\mu A$, $1.2MeV$

- **Normalization:** Charge collection and LaBr detector
- **Number of Data Points:** 47 (ranging from 88° to 42° (angular step: 1°)
- **Results:** Technical problems with KN accelerator encountered. Due to this problem, some of the results were strange, with expected glass/no glass ratio of 1 for NaI detector and 0.1 for HPGe detector. Still no positive conclusion regarding nuclear resonance dip.

EXPERIMENTAL SET #5

- **Detection Used:** HPGe and small NaI
- **Filter:** Glass, (width: $4mm$, length $20cm$, detector-source distance $27cm$)
- **Proton Beam:** $60\mu A$, $1.2MeV$
- **Normalization:** No normalization, comparison of vertically symmetrical detectors.
- **Number of Data Points:** 8
- **Results:** As expected. Ratio of 1 obtained for two identical experimental sets, taken on two consecutive days. This experiment confirmed the stability of a KN accelerator over the course of two days.

EXPERIMENTAL SET #6

- **Detection Used:** HPGe

- **Filter:** No filter used
- **Proton Beam:** Energy varying
- **Normalization:** No normalization
- **Number of Data Points:** 10
- **Results:** Proton energy calibration at $992keV$. The up shift of more than $20keV$ observed. Successful energy calibration of the KN accelerator.

EXPERIMENTAL SET #7

- **Detection Used:** HPGe
- **Filter:** Glass, (width: $6mm$, length $20cm$, detector-source distance $32cm$)
- **Proton Beam:** $992keV$
- **Normalization:** Charge collection and large NaI
- **Number of Data Points:** 51 (ranging from 80° to 30° (angular step: 1°)
- **Results:** Totally, inconclusive. Perhaps, due to longevity of experiments and consequently deterioration of the target. Features that could not be explained appeared everywhere in the results.

Chapter 5

Preliminary Dosimetry, Conclusion and Future Work

5.1 Conclusion and Preliminary Dosimetry

Chapters 2, 3 and 4 represent all the experimental work performed during the course of this thesis. Numerous different, similar or repeated experiments were conducted in order to explore the possibility of optimizing the experimental site at the McMaster KN Accelerator for nuclear resonance absorption and fluorescence experiments with the Si nucleus. As we have seen some results were very satisfactory and in very good agreement with the literature, while some were inconclusive and needed more research and experimental development. In particular, this was the case with $1.78MeV$ first excited state of Si and experiments in chapter 4. Overall, we can say that this pilot project can serve as very strong base for further exploration of the phenomenon of nuclear resonance fluorescence and absorption. Furthermore, this can serve as a base for usage of this phenomenon in detection of nuclides of interest *in vitro* and *in vivo*. We have also seen all the difficulties associated with this

experimental technique and finally all the limitations of the present McMaster KN accelerator.

In chapter 2, we started with thick target gamma yield experiments and we were using both NaI and HPGe detectors in order to check for the total gamma yield from the reaction of interest; $^{27}Al(p,\gamma)^{28}Si$. The results obtained and presented here were in very good agreement with existing literature. Moreover, they were repeatable and consistent regardless the detector used. Proton energy dependent and step like increasing, total thick target gamma yields were observed with a NaI detector. Furthermore, when using a HPGe detector, different increasing gamma yields were observed from single lines, corresponding to different nuclear reactions. In particular those were: $^{27}Al(p,p'\gamma)^{27}Al$ and $^{27}Al(p,\alpha\gamma)^{24}Mg$, and $^{27}Al(p,\gamma)^{28}Si$. Corresponding observed gamma lines were: $844keV$, $1014keV$ and $1369keV$, together with the $1.78MeV$ line coming from the very last reaction. The relative gamma yields from these lines were in very close agreement with the literature. This is thoroughly discussed in chapter 2. Finally, these results served as a very good starting point for the continuation of the exploration of the nuclear reaction of interest and the phenomenon of nuclear resonance fluorescence and absorption.

In chapter 3 we performed more specific experiments, where NRF and NRA phenomena were observed directly. Particularly, for these experiments we used a thin Al target and the well known $12.33MeV$ transition in order to induce NRF and NRA. Evidently, the results obtained in three independent and similar experiments were in very good agreement with the literature [10]. Also they were repeatable and consistent, with an existing nuclear resonance

dip of approximately 20% (transmission), centered at an angle of 71°. The results were consistent both with HPGe and NaI detectors. All the experimental findings from chapter 2 and 3 were very encouraging for further exploration of other possible means of inducing NRF on Si, using proton capture on pure Al.

Chapter 4 deals with the new approach of choosing the first excited state of Si, which is $1.78MeV$ above ground state. Unfortunately, these experiments did not yield conclusive results about the possible presence of nuclear resonance absorption phenomena at $1.78MeV$. The empirical calculations and comparisons performed have suggested comparable outcomes and close agreement between the $12.33MeV$ and $1.78MeV$ lines. However, the experiments in chapter 4 did not yield the expected results. The experimental sets were very long, requiring great stability of the KN accelerator. Unfortunately, in many attempts we have observed huge instabilities of this machine. This was discussed and elaborated thoroughly. As a consequence, these experiments should be repeated under better conditions and with using a better and more advanced accelerators, if possible.

Also, there is a problem of a blurring of the $1.78MeV$ line due to the additional recoil effects of the preceding cascade radiation [99]. This radiation has a nominal energy value of around $10MeV$. The recoil energy of the Si nucleus due to $10MeV$ gamma ray is about $4keV$, according to calculations in section 1.3. Also, according to calculations in section 4.1, the initial kinetic energy of the recoil Si nucleus is around $35keV$. This is transferred purely from the incoming proton (proton capture). The $4keV$ recoil energy due to

preceding $10MeV$ (nominal) gamma ray further complicates the situation and for sure works against resolution of the possible Gaussian nuclear resonance absorption dip from $1.78MeV$ line, even though there is an order of magnitude difference between this value and the recoil due to proton capture.

At the end preliminary radiation dose measurements were performed in order to check for the maximum gamma dose rates that come from the accelerator target, used in the usual experimental setups. These measurements were performed with a $600cc$ ionization chamber, connected to a Farmer dosemeter (model: $2570A$).

For the first two measurements, the ionization chamber was set directly in front of the proton target, with no shielding present. The distance between the proton target and chamber build up cap was $4cm$, only. The nominal proton current was set to its maximum; $60\mu A$ while the proton energy was at $2.2MeV$. This way, we ensured that the maximum photon dose output was observed. Two consecutive $30min$ measurements were taken. The first measurement yielded an exposure of $4.39mR$, while the second one yielded $4.14mR$. Taking into the account an approximate conversion factor ($1mR = 9.5\mu Gy$), we end up with an average accumulated dose of $40.5\mu Gy/$ in $30min$ for the nominal proton current of $60\mu A$.

Similarly, two $30min$ measurements that followed, were performed under the same conditions as above. However, in this case, the distance between the chamber and proton target was $60cm$ without lead shielding present. Two consecutive readings were obtained: $0.07mR$ and $0.12mR$. On average, this

would yield a total $30min$ photon dose of $0.9\mu Gy$ for the nominal proton current of $60\mu A$ and proton energy of $2.2MeV$.

At the end, the last $30min$ measurement was performed at the same distance as the previous two measurements. However, this time a $14cm$ Pb shield was placed between the chamber and proton target. This was the same shield that was used throughout this work, with usual soda lime glass absorber ($4mm$ thick) sandwiched between two lead slabs. In $30min$, no cumulative exposure was seen for this measurement. In other words, dose of zero is measured in this case. However, in order to perform a conservative dose estimates for this particular case, we will consider no shield $60cm$, $30min$ dose of $0.9\mu Gy$. In a hypothetical experiment, if we were able to produce 100 times the photon fluence (i.e. proton current of $6mA$ would yield this photon fluence), the dose would simply be around $90\mu Gy$. Furthermore, under another conservative assumption that all the photon dose comes from high energy gamma rays ($12.33MeV$) and if we set up lead shield of $14cm$ between the dosemeter and the Al target we would finally end up with a photon dose that is attenuated to approximately 0.022%. Note that this number is derived from the fact that a linear attenuation coefficient for the $12.33MeV$ gamma ray in Pb is $0.6027cm^{-1}$ [98]. These measurements showed that no significant photon dose is observed and therefore the dose cannot pose a significant concern in potential usage of this technique for *in vivo* measurements. This is even true for the hypothetical proton currents that are 1000 times higher than the maximum current used in these experiments.

In chapter 3 we have seen that using $12.33MeV$ line, our sensitivity for detecting Si was at least 5%. If we were to increase proton current 100 times, as discussed, the sensitivity of silicon detection would improve as a square root of the current and our detection limits would consequently drop to about 0.5%. Similarly, if we were able to run at even higher currents ($60mA$, for example), our detection limits would be as low as 0.15%. In summary, this conservative estimate shows that proton currents of about $60mA$ would bring a detection limits of Si to as low as $1500ppm$, with a photon dose as a non significant factor. This is still above the nominal concentration of Si in human tissue ($350ppm$). However, this conservative calculation shows that Si detection would improve significantly, using higher proton currents.

In the realistic case this number would perhaps be even lower, since possible *in vivo* measurements would be performed in human tissue, which has mass density of about 2.53 times less than soda lime glass [63]. As a rule of thumb, in human tissue, proton currents of approximately $60mA$ would indirectly induce the nuclear resonance transmission phenomenon detectably with Si nuclei in the concentrations probably lower than $1000ppm$. This is valid for the $12.33MeV$ line and experiments similar to the one performed in chapter 3. So far, we do not have a definite conclusion for the experiments performed with the $1.78MeV$ line. However, in the hypothetical situation; if we were able to obtain proton currents in mA, it would be important to repeat experiments with the $1.78MeV$ line. Essentially, the majority of experiments performed in chapter 4 should be simply repeated. However, creating mA proton currents is another issue and another task that is practically impossible with present KN or Tandem Accelerators at McMaster University. Nevertheless, today, there

are commercially available accelerators that can produce high proton currents of several mA, coupled with proton energies between 0.4 and $4MeV$. These accelerators were developed in late 2009 by a Belgium company IBA-Industrial, formely Radiation Dynamics. Currently, $10mA$ machines are available commercially. The price of such a machine is in the order of 3 million USD. A commissioning with all appropriate testings could take up to 18 months. The accelerators were described by Cleland et al. [100] at the AIP conference in late 2009. In fact, the accelerator was patented by the same author in early 2010. The dc proton source is compact high-current microwave-driven, dissipating high power of more than $40kW$ of protons [100]. The main purpose of these machines should be Boron Neutron Capture Therapy (BNCT) and detection of explosives (nitrogen) using nuclear resonance fluorescence. The later is based on already discussed $^{13}C(p,\gamma)^{14}N$ reaction and $9.17MeV$ resonance line. Considering all that has been said so far and the fact that radiation dose is not a significant issue, the use of these high current, medium energy accelerators should be the future step in the nuclear resonance exploration of *Si in vitro* and possibly *in vivo*. Both $12.33MeV$ and $1.78MeV$ gamma line experiments should be repeated and reassessed. Moreover, this thesis should be a very strong starting point for further research.

5.2 Future Work

As previously mentioned, all the experiments from chapters 3 and 4 should be reassessed with a new generation of accelerators capable of delivering very high proton currents in mA and energies up to approximately $3MeV$. The ex-

periments with the $12.33MeV$ line should be repeated with doped phantoms with different concentrations of Si in order to establish minimum detection limits (MDL). The advantage of these experiments is the fact that no angle exploration for maximum Doppler shift is needed, since it is already experimentally established at 71° with respect to incoming proton beam. On the other hand, all the experimental work with $1.78MeV$ line should be repeated from the very beginning because an angle of maximum Doppler shift could not be defined from our experiments in chapter 4. However, in both cases, much better statistics paired with a shorter acquisition times will certainly be experienced. This is because the proton current would be in order of 1000 times higher, compared to present capabilities. As far as photon doses are concerned, we have already seen that even for mA proton currents this would be negligible.

The other possible way of exploring detection of Si could be the Proton Induced Gamma Emission technique (PIGE). This technique is rather similar to the one performed in chapter 2, where proton induced gamma yields from various nuclear reactions on Al were observed. The experiments would involve a proton beam directly onto the target of interest. In this case it would be a Si target. In other words, it would be a direct proton capture or proton scatter of Si nuclei. Two reactions of interest are: $^{28}Si(p,p'\gamma)^{28}Si$ and $^{28}Si(p,\gamma)^{29}P$. The scattering reaction produces a gamma ray at $1.78MeV$, while the proton capture reaction gives off a gamma ray at $1.38MeV$. There are many studies that deal with PIGE from the Si nucleus. We will mention some of them here and some have already been mentioned before. For example, Savidou et al. [14] found the highest yield of $1.78MeV$ gamma rays from scattering reac-

tion at $4MeV$ proton energy. The yield was in the order of $10^7 counts/\mu Csr$. For comparison purposes, the same study quotes $1.78MeV$ gamma yield from $^{27}Al(p,\gamma)^{28}Si$ reaction at $1.77MeV$ proton energy to be $6.7\times10^3 counts/\mu Csr$. Obviously, almost 3000 times higher yields of $1.78MeV$ are observed with direct PIGE of Si. At the same time, Kiss et al. [101] quote the yield of the capture reaction to be: $91 counts/\mu Csr$ at $2.4MeV$ of proton incident energy, while scattering yield was quoted to be: $7.2 \times 10^6 counts/\mu Csr$ at $3.8MeV$ of proton energy. Evidently, the numbers from these two independent studies are in very close agreement. Furthermore, Kenny et al. [102] calculated $1.78MeV$ yield to be $4.0 \times 10^2 counts/\mu Csr$. These experiments were done with $2.514MeV$ protons. So far we can see a huge drop of gamma yield with a decrease in proton kinetic energy. Another interesting study was done by Hanson et al. [103]. Here, they have compared ratio of Al to Si in zeolite, using prompt inelastic scattering. In particular, they have observed the $844keV$ and $1014keV$ lines of Al and the $1.78MeV$ line of Si. The proton energy was at $3.4MeV$. The ratio of gamma yields actually determined the actual ratio of these metals in zeolite samples. Similar studies were done by Antilla et al. [104], Deconninck [105] and Deconninck & Demortier [106]. Moreover, Demortier and Bodart [107] measured phosphorus by (p,γ) reactions. Interestingly, they have manage to achieve sensitivity between 50 and $1000ppm$, with a proton currents of as low as $0.01\mu A$. The proton energies varied between $1MeV$ and $2.5MeV$. One of the most important issues in these kinds of experiments, which are at the same time charged particle activation experiments, is the correction for the stopping power, based on CSDA. Isshii et al. explain this in detail and give the theoretical background in their two articles [108] [109].

There are several problems associated with detection of Si using the PIGE technique at the McMaster KN accelerator. The most obvious one is the fact that highest gamma yields are observed above $3.5MeV$. We can see from the studies discussed that gamma yields abruptly decrease as we decrease proton energy. Unfortunately, currently KN machine is capable of delivering $2.5MeV$ only. Furthermore, the technique had to be done *in vitro*. In other words, a tissue sample would have to be taken from the patient and the proton target would have to be made out of this tissue sample. Therefore, the technique would have to be invasive. Of course, calibration studies would have to be performed beforehand and MDL would have to be established for standard Si doped proton targets.

END.

Appendix A

Derivation of the relationship between the angles θ and φ, asymmetrical position of HPGe and NaI detectors with respect to the proton beam

This appendix derives equation 4.15. This is the relationship between the angles θ and φ. From figures 4.32 and 4.33, they represent the angle between the proton beam direction and the HPGe detector and the corresponding angle between the proton beam direction and the NaI detector, respectively. This is an asymmetrical case described before in chapter 4. A three-dimensional representation of the asymmetrical experimental site is given in figure 5.1 below. In fact this is a three-dimensional representation of figures 4.32 and 4.33. From this figure, point D represents the position of the Al proton target. Protons hit the target from the left and therefore, the direction of their movement is along line DE. Point E, represents the original position of the HPGe detector (at 0° geometry). At the same time, point B represents position of the NaI detector. The new positions of the HPGe and NaI detectors are points F and C, respectively, after rotation of the whole system through an angle θ.

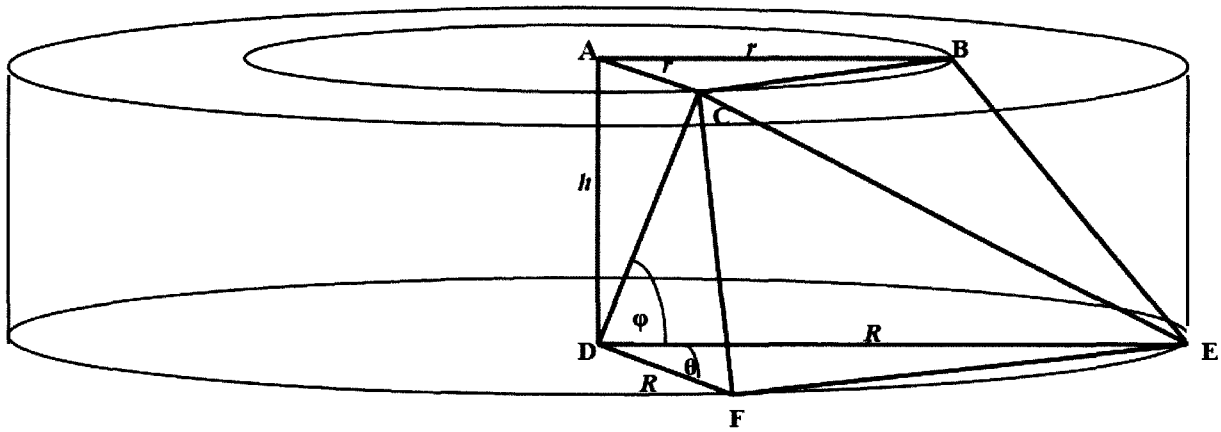

Figure 5.1: Angles of Interest

To further clarify the figure, consider the truncated pyramid $ABCFDE$. We are going to derive the relationship between angles of interest; θ and φ. In order to do that, we are going to isolate several triangles from this picture. Consider $\triangle ABC$, by Cosine rule, we have:

$$BC^2 = 2r^2(1 - \cos\theta) \tag{5.1}$$

Similarly, from $\triangle DEF$, we have:

$$FE^2 = 2R^2(1 - \cos\theta) \tag{5.2}$$

Also, from the right angle $\triangle DAC$, we have:

$$DC^2 = h^2 + r^2 \tag{5.3}$$

Furthermore, consider the right trapezoid $\square ACDF$, we can easily calculate the length of CF. This is given by:

$$CF^2 = h^2 + (R - r)^2 \tag{5.4}$$

Now, considering the other trapezoid $\square CBEF$, we can easily deduce that CF=BE. Finally, we want to figure out the length of CE. Simply, using the Pythagorean theorem, we can deduce that:

$$CE^2 = h^2 + (R - r)^2 + CB \times FE \tag{5.5}$$

Finally, we can consider $\triangle DCE$, where all sides are known. Using the cosine rule, we have:

$$DC^2 + DE^2 - 2DC \times DE cos\varphi = CE^2 \tag{5.6}$$

Furthermore, recalling the above relationships: 5.3 and 5.5, the above equation becomes:

$$h^2+r^2+R^2-2R\sqrt{h^2+r^2}cos\varphi = h^2+(R-r)^2+\sqrt{2r^2(1-cos\theta)}\sqrt{2R^2(1-cos\theta)} \tag{5.7}$$

Manipulating the above equation we end up with the final relationship between angles θ and φ:

$$cos\varphi = -\frac{r}{\sqrt{h^2+r^2}}cos\theta \tag{5.8}$$

Bibliography

[1] Jugdaohsingh R. et al. Silicon and Bone Health. *Journal of Nutrition Health and Aging*, 11:99, 2007.

[2] Powell J.J. et al. A Provisional Database for the Silicon Content of Food in United Kingdom. *British Journal of Nutrition*, 94:804, 2005.

[3] Krane K.S. Introductory Nuclear Physics. *John Wiley and Sons*, 1988.

[4] Metzger F.R. Nuclear Resonance Fluorescence in ^{72}Ge and ^{74}Ge. *Physical Review*, 101(1), 1956.

[5] Sowerby B.D. A Comparison of Gamma Ray Resonance Scattering Techniques for Borehole Analysis. *Nuclear Instruments and Methods*, 108:317, 1972.

[6] Metzger F.R. Nuclear Resonance Fluorescence in ^{60}Ni. *Physical Review*, 103(4):983, 1956.

[7] Beard G.B. & Kelly W.H. Half Life of the $1.27MeV$ Level in ^{116}Sn by Resonant Self Absorption. *Nuclear Physics*, 43:523, 1963.

[8] Sparks R.J. et al. Resonant Gamma Ray Absorption in ^{208}Pb. *Nuclear Physics*, A259:13, 1976.

[9] Rust N.J.A. et al. Nuclear Resonance Fluorescence with a $4000Ci$ ^{60}Co Radioactive Source. *Nuclear Instruments and Methods*, 67:222, 1969.

[10] Smith P.B. & Endt P.M. Resonant Absorption of Gamma Radiation from the $^{27}Al(p,\gamma)^{28}Si$ Reaction. *Physical Review*, 110(2):397, 1957.

[11] Timmermann R. et al. Search for Low-Energy Resonances in $^{27}Al(p,\alpha)^{24}Mg$. *Nuclear Physics A*, 477:105, 1988.

[12] Demortier G. et al. IBA of Au-Al Alloys. *Nuclear Instruments and Methods in Physics Research*, B85:311, 1994.

[13] Fink C.L. et al. Gamma Rays Produced by $1.75 - 4Mev$ Proton Bombardment of Thick Aluminium Targets. *Nuclear Instruments and Methods in Physics Research A*, 505:5, 2003.

[14] Savidou A. et al. Proton induced thick target γ-ray yields of light nuclei at the energy region $E_p = 1.0 - 4.1Mev$. *Nuclear Instruments and Methods in Physics Research B*, 152:12–18, 1999.

[15] Paul H. http://www.exphys.uni-linz.ac.at/stopping/.

[16] Fleming D. et al. Accumulated Body Burden and Endogenous Release of Lead in Employees of a Lead Smelter. *Environmental Health Perspectives*, 105:224, 1997.

[17] Zamburlini M. et al. In Vivo Study of an X-Ray Fluorescence System to Detect Bone Strontium Non-Invasively. *Physics in Medicine and Biology*, 2007:2107, 2007.

[18] Grinyer J. et al. In Vivo Prompt Gamma Neutron Activation Analysis of Cadmium in the Kidney and Liver. *Applied Radiation and Isotopes*, 63:475, 2005.

[19] Studinski R.C.N. et al. Estimation of a Method Detection Limit for an In-Vivo XRF Arsenic Detection System. *Physics in Medicine and Biology*, 50:521, 2005.

[20] Chettle D.R. & Fremlin J.H. Techniques of In Vivo Neutron Activation Analysis. *Physics in Medicine and Biology*, 29:1011, 1984.

[21] Atanackovic J. et al. The Comparison of Two MCNP Models Used for Prompt Gamma In-Vivo Detection of Cadmium and Mercury. *Nuclear Instruments and Methods B*, 263:169, 2007.

[22] Pejovic A. et al. Monte Carlo Design Study for In-Vivo Bone Aluminum Measurement Using a Low Energy Accelerator Beam. *Applied Radiation and Isotopes*, 53:657, 2000.

[23] Davis K. et al. In Vivo Measurements of Bone Aluminum in Population Living in Southern Ontario, Canada. *Medical Physics*, 35:11, 2008.

[24] Aslam et al. Noninvasive Measurement of Aluminium in Human Bone: Preliminary Human Study and Improved System Performance. *Journal of Inorganic Biochemistry*, 103:1585, 2009.

[25] Arnold M. Development of an Accelerator Based System for In-Vivo Neutron Activation Analysis Measurements of Manganese in Humans. *McMaster University, PhD Thesis*, 2000.

[26] Aslam et al. Oportunities to Improve In Vivo Measurements of Manganese in Human Hands. *Physics in Medicine and Biology*, 54:17, 2009.

[27] Aslam et al. Quantification of Manganese in Human Hand Bones: A Feasibility Study. *Physics in Medicine and Biology*, 53:4084, 2008.

[28] Aslam et al. In Vivo Assessment of Magnesium Status in Human Body Using Accelerator-based Neutron Activation Measurement of Hands: A Pilot Study. *Medical Physics*, 35:608, 2008.

[29] Byun S.H. et al. Dosimetric Characterization of the Irradiation Cavity for Accelerator Based In Vivo Neutron Activation Analysis. *Physics in Medicine and Biology*, 52:1963, 2007.

[30] Aslam et al. Development of a Low Energy Monoenergetic Neutron Source for Applications in Low Dose Radiobiological and Radiochemical Research. *Applied Radiation and Isotopes*, 58:144, 2003.

[31] Vartsky D. et al. Gamma Ray Nuclear Resonance Absorption: An Alternative Method for In-Vivo Body Composition Studies. *Annals of New York Academy of Sciences*, 904:236, 2000.

[32] Brookhaven National Laboratories. http://www.nndc.bnl.gov/.

[33] Exley C. Silicon in Life: A Bioinorganic Solution to Bioorganic Essentiality. *Journal of Inorganic Biochemistry*, 69:139, 1998.

[34] Sjöberg S. Silica in Aqueous Environments. *Journal of Non-Crystalline Solids*, 196:51, 1996.

[35] Bellia J.P. et al. Beer: A Dietary Source of Silicon. *The Lancet*, 343:235, 1994.

[36] Birchall J.D. et al. Aluminum, Water Chemistry and Alzheimer's Disease. *The Lancet*, page 953, 1989.

[37] Parry R. et al. Silicon and Aluminum Interactions in Haemodialysis Patients. *Nephrology Dialysis Transplatation*, 13:1759, 1998.

[38] Roberts N.B. et al. Silicon Measurement in Serum and Urine by Direct Current Plasma Emission Spectrometry. *Clinical Chemistry*, 36:1460, 1990.

[39] Jugdaohsingh R. et al. Dietary Silicon Intake and Absorption. *American Journal of Clinical Nutrition*, 75:887, 2002.

[40] McNaughton S.A. et al. Dietary Silicon Intake in Post-Menopausal Women. *British Journal of Nutrition*, 94:813, 2005.

[41] Pennington J.A.T. Silicon in Foods and Diets. *Food Additives and Contaminants*, 9:97, 1991.

[42] Dobbie J.W. & Smith M.J.B. The Silicon Content of Body Fluids. *Scottish Medical Journal*, 27:17, 1982.

[43] Schwarz K. & Milne D.B. Growth Promoting Effects of Silicon in Rats. *Nature*, 239:333, 1972.

[44] Carlisle E.M. Silicon: An Essential for the Chick. *Science*, 178:619, 1972.

[45] Jugdaohsingh R. et al. Silicon Intake is a Major Dietary Determinant of Bone Mineral Density in Men and Premenopausal Women of the Fram-

ingham Offspring Cohort. *Journal of Bone and Mineral Research*, 19:297, 2004.

[46] MacDonald H.M. et al. Dietary Silicon Intake is Associated with Bone Mineral Density in Premenopausal Women and Postmenopausal Women Taking HRT. *Journal of Bone and Mineral Research*, 20:393, 2005.

[47] Seaborn C.D. & Nielsen F.H. Dietary Silicon Affects Acid and Alkaline Phosphatase and ^{45}Ca Uptake in Bone of Rats. *The Journal of Trace Elements in Experimental Medicine*, 7:1, 1994.

[48] Seaborn C.D. & Nielsen F.H. Effects of Germanium and Silicon on Bone Mineralisation. *Biological Trace Element Research*, 42:151, 1994.

[49] Seaborn C.D. & Nielsen F.H. Silicon Deprivation Decreases Collagen Formation in Wounds and Bone and Ornithine Transaminase Enzyme Activity in Liver. *Biological Trace Element Research*, 89:251, 2002.

[50] Seaborn C.D. & Nielsen F.H. Dietary Silicon and Arginine Effect Mineral Element Composition of Rat Femur and Vertebra. *Biological Trace Element Research*, 89:239, 2002.

[51] Elsinger J. & Clairet D. Effects of Silicon, Fluoride, Etidronate and Magnesium on Bone Mineral Density: A Retrospective Study. *Magnesium Research*, 6:247, 1993.

[52] Spector T.D. et al. Effect of Bone Turnover and BMD of Low Dose Oral Silicon as an Adjunct to Calcium/Vitamin D3 in a Randomized Placebo Control Trial. *Journal of Bone Mineral Research*, 20:S172, 2005.

[53] X-Ray Data Booklet. Center for X-Ray Optics and Advanced Light Source.

[54] Database for Prompt Gamma-ray Neutron Activation Analysis. http://www-nds.iaea.org/pgaa/.

[55] Ettinger K.V. et al. Silicon Measurement in a Lung Phantom by Neutron Inelastic Scattering. *Medical Physics*, 9(4), 1982.

[56] Harissopulos S. et al. The $^{27}Al(p,\gamma)^{28}Si$ Reaction: Direct Capture Cross-Section and Resonance Strenghts at $E_p = 0.2 - 1.12MeV$. *The European Physical Journal A*, 9:479, 2000.

[57] Meyer M.A. et al. Energy Levels of ^{28}Si. *Nuclear Physics*, A250:235, 1975.

[58] Chronidou C. et al. Resonance Strength Measurements of the $^{27}Al(p,\gamma)^{28}Si$ Reaction in the Energy Range $E_p = 0.8 - 2.0MeV$. *The European Physical Journal A*, 6:303, 1999.

[59] Bethe H.A. & Placzek G. Resonance Effects in Nuclear Processes. *Physical Review*, 31:450, 1937.

[60] Metzger F.R. Resonance Fluorescence in Nuclei. *Progress in Nuclear Physics*, 7, 1959.

[61] Kittel C. Introduction to Solid State Physics. *John Wiley and Sons, VII Edition*, 1996.

[62] Lamb Jr W.E. Capture of Neutrons by Atoms in a Crystal. *Physical Review*, 55:190, 1939.

[63] Seward T. & Vascott T. High Temperature Glass Melt Property Database for Process Modeling. *American Ceramic Society*, 2005.

[64] Eckert A.C. & Shrader E.F. Nuclear Resonant Absorption of Gamma Rays by ^{40}Ca. *Physical Review*, 124(5):1541, 1961.

[65] Rose M.E. et al. Westinghouse Atomic Power Division Report SR-506. *Vol I and II*, 1954.

[66] Beynon T. D. & Grant I.S. Evaluation of the Doppler-Broadened Single-Level and Interference Functions. *Nuclear Science and Engineering*, 17(3), 1963.

[67] Duderstadt J.J. & Hamilton L.J. Nuclear Reactor Analysis. *John Wiley and Sons*, 1976.

[68] Melkonian E. et al. Slow Neutron Velocity Spectrometer Studies. V, Re, Ta, Ru, Cr, Ga. *Physical Review*, 92(3), 1953.

[69] Dardel G & Persson R. Determination of Neutron Resonance Parameters from Measurements of the Absorption Integral: Application to the Main Resonance of Uranium-238. *Nature*, 170(4339), 1952.

[70] Metzger F.R. Angular Distribution of the Resonance Fluorescence Radiation from the $411keV$ Excited State of ^{198}Hg. *Physical Review*, 97(5), 1954.

[71] Moon P.B. & Storruste A. Resonant Nuclear Scattering of ^{198}Hg Gamma Rays. *Proceeding of the Physical Society of London*, A66:585, 1953.

[72] Moon P.B. Resonant Nuclear Scattering of Gamma Rays: Theory and Preliminary Experiments. *Proceeding of the Physical Society of London*, A64:76, 1951.

[73] Knapp V. Nuclear Resonant Scattering of Gamma Rays in ^{199}Hg. *Proceeding of the Physical Society of London*, A70:142, 1957.

[74] Herrmann D. & Klaus J. Lifetime of the $1.37MeV$ State in ^{24}Mg. *Nuclear Physics*, A140:257, 1970.

[75] Tikkanen P. et al. Short Lifetimes in ^{28}Si. *Physical Review C*, 47(1):145, 1993.

[76] Metzger F.R. Properties of the $4.431MeV$ Excited State of ^{23}Na. *Physical Review*, 904:229, 1964.

[77] Hough J.H. & Mouton W.L. Nuclear Resonant Scattering of Bremsstrahlung from Low Lying Levels in ^{27}Al, ^{31}P and ^{35}Cl. *Nuclear Physics*, 76:248, 1966.

[78] Vartsky D. et al. Nuclear Resonant Scattering of Gamma Rays - A New Technique for In Vivo Measurement of Body Iron Stores. *Physics in Medicine and Biology*, 24(4), 1979.

[79] Vartsky D. et al. A Preliminary Investigation of Nuclear Resonant Scattering as a New Technique for In Vivo Measurement of Hepatic Copper. *Physics in Medicine and Biology*, 21(6), 1976.

[80] Kelly W.H. & Beard G.B. Nuclear Resonance Fluorescence Measurements on the $845keV$ Level in ^{56}Fe. *Nuclear Physics*, 27:188, 1961.

[81] Begzhanov R.B. et al. Lifetime of the $0.845Mev$ Level of the ^{56}Fe Nucleus. *Soviet Physics JETP*, 17(1), 1963.

[82] Biesiot W. & Smith P.B. Parameter of the $9.17Mev$ Level in ^{14}N. *Physical Review C*, 24(6), 1981.

[83] Hanna S.S. & Meyer-Schützmeister L. Resonant Absorption by the $9.17MeV$ Level in ^{14}N. *Physical Review*, 115(4), 1959.

[84] Wielopolski L. et al. Gamma Resonance Absorption New Approach in Human Body Composition Studies. *Annals of New York Academy of Sciences*, 904:229, 2000.

[85] Vartsky D. et al. Detectors for the Gamma-Ray Resonant Absorption GRA Method of Eplosive Detection in Cargo: A Comparative Study. *Proceedings of SPIE*, 5198:243, 2004.

[86] Mu G.U. et al. Measurements of Some Level Widths in ^{40}Ca Between 9.5 and $10.5MeV$. *Nuclear Physics*, A462:482, 1987.

[87] Van Der Leun C. & Burhoven J.N.C. A Resonant Absorption Measurement in the Reaction $^{26}Mg(p,\gamma)^{27}Al$. *Nuclear Physics*, 88:235, 1966.

[88] Smith P.B. & Endt P.M. Resonant Absorption of Gamma Radiation from the $^{30}Si(p,\gamma)^{31}P$. *Physical Review*, 110(6):1442, 1958.

[89] Bakkum E.L. et al. Resonant-Absorption Measurements of Attosecond Lifetimes. *Nuclear Physics A*, 441:209, 1985.

[90] Physical Reference Data: Stopping Power, Protons Range Tables for Electrons, and Helium Ions. http://www.physics.nist.gov/physrefdata/star/text/contents.html.

[91] Knoll G.F. Radiation Detection and Measurement. *John Wiley and Sons, II Edition*, 1989.

[92] Leung P.T. Addendum: Bethe Stopping Power Theory for Heavy Target Atoms. *Physical Review A*, 60:2562, 1999.

[93] Tschalar C. & Bichsel H. Mean Excitation Potential of Light Compounds. *Physical Review*, 175:476, 1968.

[94] Ziegler J.F. The Stopping of Energetic Light Ions in Elemental Matter. *Journal of Applied Physics*, 85:1249, 1999.

[95] Ziegler J.F. http://www.srim.org/.

[96] Lennard W.N. & Geissel H. Energy Loss and Energy Loss Straggling for Heavy Ions. *Nuclear Instruments and Methods in Physics Research B*, 27:338, 1986.

[97] Evans R.D. The Atomic Nucleus. *McGraw-Hill Book Company Inc.*, 1955.

[98] Physical Reference Data: XCOM Photon Cross Section Database. http://physics.nist.gov/physrefdata/xcom/text/xcom.html.

[99] Waddington J.C. Private Communication. 2010.

[100] Cleland M.R. et al. A New High-Current Proton Accelerator. *AIP Conference Proceedings*, 1099:42, 2009.

[101] Kiss A.Z. et al. Measurements of Relatively Thick Target Yields for PIGE Analysis on Light Elements in the Proton Energy Intervals 2.4−4.2 MeV. *Journal of Radioanalytical and Nuclear Chemistry*, 89/1:123, 1985.

[102] Kenny M.J. et al. Proton Induced γ-Ray Yields. *Nuclear Instruments and Methods*, 168:115, 1980.

[103] Hanson A.L. & Jones K.W. Determination of Si-Al Ratio in Zeolites by Proton Inelastic Scattering. *Nuclear Instruments and Methods in Physics Research B*, 9:301, 1985.

[104] Antilla A. et al. Proton Induced Thick Target Gamma-Ray Yields for the Elemenatal Analysis of the Z=3 − 9, 11 − 21 Elements. *Journal of Radioanalytical Chemistry*, 62:293, 1981.

[105] Deconninck G. Analysis by Prompt X and Gamma Ray Detection. *Journal of Radioanalytical Chemistry*, 12:157, 1972.

[106] Deconninck G. & Demortier G. Quantitative Analysis of Aluminium by Prompt Nuclear Reactions. *Journal of Radioanalytical Chemistry*, 12:189, 1972.

[107] Demortier G. & Bodart F. Quantitative Analysis of Phosphorus by (p, γ) Reactions. *Journal of Radioanalytical Chemistry*, 12:209, 1972.

[108] Ishii K. et al. The Averaged Stopping Power Method for Accurate Charged Particle Activation Analysis. *Nuclear Instruments and Methods*, 150:212, 1978.

[109] Ishii K. et al. Accurate Charged Particle Activation Analysis: Calculation of the Average Energy in the Average Stopping Power Method. *Nuclear Instruments and Methods*, 153:503, 1978.